UNIVERSITY OF SOUTHAMPTON

Ultrashort pulse surface emitting semiconductor lasers

by

Keith G. Wilcox

A thesis submitted in partial fulfillment for the degree of Doctor of Philosophy

in the

Faculty of Engineering, Science and Mathematics

School of Physics and Astronomy

May 2006

UNIVERSITY OF SOUTHAMPTON

ABSTRACT

FACULTY OF ENGINEERING, SCIENCE AND MATHEMATICS
SCHOOL OF PHYSICS AND ASTRONOMY

Doctor of Philosophy

by Keith G. Wilcox

This thesis is a report of the experimental investigation of mode locked optically pumped vertical-external-cavity surface-emitting semiconductor lasers (OP-VECSEL). Mode locked VECSELs are a promising laser technology with transform limited pulses as short as 448fs being generated directly from the laser oscillator. Mode locked VECSELs have the advantages of being; high repetition rate, compact, low cost, robust, power scalable to high output power and near turn key operation.

Here, I report the first characterisation of the timing jitter and amplitude jitter of a mode locked VECSEL producing picosecond pulses. A mode locked VECSEL has also been locked to an external electrical oscillator, demonstrating the first active stabalisation of the timing jitter. I also report the first application of a mode locked VECSEL as a laser used to generate broadband THz radiation. The laser dynamics during the mode-locking buildup time of the laser has also been investigated to gain an understanding of the pulse formation mechanisms and pulse duration limiting processes. Finally multiple pulse operation has been observed for the first time and has been characterised.

Contents

Declaration of Authorship x

Acknowledgements x

1 Introduction 1
- 1.1 The Vertical Cavity Surface Emitting Laser . . . 1
- 1.2 Comparison of semiconductor laser technology and VECSELs . . . 2
- 1.3 Comparison of thin disk diode pumped solid-state lasers and VECSELs . 5
- 1.4 Key results achieved for VECSELs and the work reported in this Thesis . 6

2 Overview of VECSEL design and Technology 10
- 2.1 Introduction . . . 10
- 2.2 Introduction to semiconductors and quantum wells . . . 11
  - 2.2.1 Semiconductor material properties . . . 11
  - 2.2.2 Carrier distribution and optical properties for semiconductor materials . . . 13
  - 2.2.3 Quantum wells and quantum confinement . . . 15
    - 2.2.3.1 Introduction to quantum confinement . . . 15
    - 2.2.3.2 Optical properties of quantum wells . . . 18
    - 2.2.3.3 Non-radiative decay mechanisms in semiconductor quantum wells . . . 20
- 2.3 Design of VECSEL gain structures . . . 21
- 2.4 Power scaling of VECSELs and the importance of heat removal . . . 29

3 Sample characterisation and CW lasing 34
- 3.1 Gain sample characterisation . . . 34
- 3.2 CW lasing characterisation . . . 42
- 3.3 Conclusions . . . 45

4 Introduction to mode locked VECSELs: Theory of mode-locking and SESAMs 46
- 4.1 Introduction to mode-locking . . . 46
- 4.2 Theory of mode-locking . . . 47
- 4.3 Fast and slow absorber passive mode-locking . . . 50
- 4.4 Haus model of mode-locking . . . 53
- 4.5 Semiconductor Saturable Absorber Mirror design parameters and production methods . . . 54

5 Mode locked VECSELs: results and multiple pulse operation 59
5.1 Introduction . . . 59
5.2 Characterisation of the fast surface recombination SESAM . . . 60
5.3 Mode-locking VECSELs with a slow saturable absorber - ps pulse production . . . 63
5.4 Quasi-soliton mode-locking VECSELs producing sub 500 fs pulses . . . 65
5.5 Observations of satellite pulses due to substrate reflections . . . 66
5.6 Multiple pulse operation . . . 71
5.7 Conclusions . . . 75

6 Pulse duration limiting processes: towards producing shorter pulses 77
6.1 Introduction . . . 77
6.2 Theory of laser build-up dynamics and methods of producing a broad gain bandwidth . . . 78
6.2.1 Theory of the laser dynamics during the build-up to steady state . 78
6.2.2 Design parameters to produce broader bandwidth samples . . . 81
6.3 Previous experimental results measuring the gain bandwidth and mode-locking onset time. . . . 81
6.4 Mode-locking onset measurements . . . 82
6.4.1 Method . . . 82
6.4.2 Mode-locking onset results for different pulse durations . . . 84
6.4.3 Discussion of results and conclusions . . . 86
6.5 Spectro-temporal measurements on a 500fs mode locked VECSEL . . . 89
6.5.1 Introduction . . . 89
6.5.2 Method . . . 90
6.5.3 Results . . . 91
6.5.4 Discussion of results and conclusions . . . 92
6.6 Conclusions and future directions for producing shorter pulses directly from a VECSEL . . . 95

7 Mode-locking laser noise characteristics: Timing jitter 100
7.1 Introduction to timing jitter . . . 100
7.2 Theory of laser noise and its characterisation . . . 103
7.3 Active stabilisation of a passively mode locked VECSEL . . . 108
7.4 Noise characterisation of a passively mode locked VECSEL and an actively stabilised passively mode locked VECSEL . . . 109
7.5 Conclusions and future work . . . 117

8 Generation of THz radiation using a VECSEL 119
8.1 Introduction to THz generation and its applications . . . 119
8.2 THz generation using VECSELs . . . 123
8.3 Experimental results for a LT-GaAsSb antenna, driven by a sub-500fs mode locked VECSEL operating with a repetition rate of 1.2 GHz and a wavelength of 1038nm . . . 126
8.4 Future work: all room temperature generation and detection . . . 129

9 Conclusions 134
9.1 Application based results for VECSELs . . . 134

9.2 Fundamental VECSEL properties 135

A Publication list **137**

Bibliography **138**

List of Figures

2.1 A schematic of a mode locked VECSEL laser cavity with close up views of the gain region and the saturable absorber. 11
2.2 A diagram showing the conduction band and valence band structure of bulk GaAs. 12
2.3 A diagram showing various III-V semiconductor materials, their band gaps and lattice constants. 13
2.4 A diagram showing the density of states for materials with different quantum confinements. 17
2.5 A diagram of a typical VECSEL gain structure showing the essential design components. 22
2.6 A diagram of a Distributed Bragg Reflector showing the alternating layers of high and low refractive index and the decreasing e-field amplitude through it. 24
2.7 Calculated reflectivity curves for a Distributed Bragg Reflector with different numbers of GaAs/AlAs pairs. 24
2.8 A diagram showing the theoretical percentage of pump absorption per quantum well. 25
2.9 Diagrams showing the magnitude of $|E|^2$ with position in the sample, and also with wavelength for the quantum wells for a resonant microcavity. . . 27
2.10 Diagrams showing the magnitude of $|E|^2$ with position in the sample, and also with wavelength for the quantum wells for an anti resonant cavity. . . 28
2.11 A schematic diagram showing the different methods to heat flow management. 31

3.1 A graph showing the theoretical reflectivity from the sample design program, with no absorption from the quantum wells, and the measured reflectivity of the sample after growth. 36
3.2 A diagram of the experimental setup for measuring edge and top PL. . . . 37
3.3 A graph showing the edge photoluminescence of the sample at a range of pump powers and at three different sample temperatures. 38
3.4 Graphs of the shift in peak PL emission with increasing pump power for two temperatures. 39
3.5 A graph showing the top photoluminescence of QT1544 at a range of pump powers and at two different sample temperatures. 39
3.6 A graph showing the Quantum efficiency of the entire gain structure. . . . 41
3.7 A graph showing integrated PL power measurements and the calculated quantum efficiency of the quantum wells for sample QT1544. 42
3.8 Laser output power curves for a range of gain temperatures for sample QT1712. 43

3.9 Graph showing the shift in laser wavelength with increasing pump power, with the sample heat-sink held at 10 degrees. 44
3.10 A graph showing the shift in laser wavelength with changing temperature of the gain sample heat-sink, for a constant pump power for QT1712. . . . 44

4.1 A schematic diagram showing fast saturable absorber mode-locking and slow saturable absorber mode-locking. 52
4.2 A schematic diagram showing the design of the surface quantum well SESAM, QT1627. 57
4.3 Published experimental results obtained showing the ac-Stark shift for a Quantum well at 27 K. 58

5.1 A graph showing the variation in reflectivity verses the incident pulse fluence for QT1627. 60
5.2 A graph showing the pump-probe measurements of the absorber recovery time of SESAM QT1627 at a wavelength of 1030nm. 61
5.3 A graph showing the pump-probe measurements of the absorber recovery time of SESAM QT1627. 62
5.4 A complete characterisation dataset for a mode locked VECSEL producing 2.13 ps pulses at a repetition rate of 939.6 MHz, with an average output power of 40 mW. 64
5.5 Complete laser characterisation of a mode locked VECSEL producing 448 fs pulses at a repetition rate of 905 MHz, with an average output power of 40 mW. The pulses are Fourier limited. 67
5.6 Autocorrelation and optical spectrum of a VECSEL producing sub 500 fs pulses and satellite pulses, with unpolished gain and SESAM. 69
5.7 Autocorrelation and optical spectrum froma a VECSEL producing sub 500 fs pulses and no satellite pulses, with polished gain and SESAM. . . . 70
5.8 Autocorrelation and fast sampling oscilloscope trace of laser pulse train showing 523 fs pulses being produced with only one pulse per round trip time. 72
5.9 Autocorrelation and fast sampling oscilloscope trace of 485 fs pulses being produced, in a multi-pulse regime, with two pulses per laser round-trip time. 73
5.10 A graph showing the number of pulses per round trip versus to incident pump power. 74
5.11 A graph showing the energy devided by the number of pulses circulating intracavity verses the pump power. 75

6.1 A schematic of the experimental setup used for mode-locking onset measurements. 83
6.2 Optical spectrums and Autocorrelations for the three mode-locking regimes showing pulse durations of 2500 fs, 627 fs and 481 fs. 85
6.3 Mode-locking onset time measurements for the three different pulse regiemes investigated. 86
6.4 The design properties of the ac Stark effect SESAM, QT1626. 89
6.5 A schematic diagram of the experimental setup used for spectro-temporal measurements. 91
6.6 Evolution of the optical spectrum at several different buildup times 92

6.7 A graph showing the inverse bandwidth squared (HWHM) versus the generation time after laser start-up. 93

7.1 Single sideband noise of a harmonically mode locked semiconductor optical amplifier laser. 102
7.2 Diagram of a low noise mode locked semiconductor optical amplifier laser. 102
7.3 A representitive diagram of a noise free pulse train and one with noise. . . 104
7.4 Diagram of the theoretical rf spectrum of the laser, showing the contributions of amplitude noise and timing jitter. 106
7.5 A schematic of the component parts of the active stabalisation feedback locking mechanism. 109
7.6 A schematic diagram of the laser cavity used for noise characterisation and for active stabalisation. 110
7.7 Autocorrelation and optical spectrum of the pulses produced by the stabilised laser. 111
7.8 A graph showing the reduction of noise of the RF spectrum of the fundamental laser repetition frequency from pump launch stabalisation and enviromental isolation. 112
7.9 A graph showing the single sideband noise of all the harmonics used for the characterisation of the actively stabilised VECSEL. 112
7.10 A graph showing the single sideband noise of all the harmonics used for the characterisation of the unstabalised VECSEL. 113
7.11 A graph showing the single side band noise measured for the 0th, 1st and 20th harmonics for the actively stabalised VECSEL. 114
7.12 A graph of the measured noise single sidebands of the 3rd harmonic for both the activly stabalised and the unstabalised VECSEL. 115
7.13 A graph showing the total integrated noise versus the harmonic number, along with a quadratic fit to the data for the un-stabilised laser. 116
7.14 A graph showing the total integrated noise versus the harmonic number, along with a quadratic fit to the data for the actively stabilised laser. . . . 116
7.15 Final extracted timing jitter single sidebands for the passively mode-locked and actively stabilised passively mode-locked VECSEL. 117

8.1 A schematic diagram of a typical THz time domain spectrometer. 120
8.2 A typical THz antenna showing a metallic H structure deposited on an LT-GaAs substrate. 121
8.3 A single cycle THz pulse and its spectrum extracted through Fourier transform for a Ti:Sapphire driven THz system 123
8.4 An image of the log-periodic antenna design used in the LT-GaAsSb antenna used in this work. 125
8.5 Photographs of the 50 mW, ¡500 fs pulse VECSEL with a repetition rate of 1.2G Hz, mounted on the INVAR base, in a compact, stable, portable and robust package. 127
8.6 A schematic diagram showing the setup used to generate THz radiation and its detection with a bolometer. 127
8.7 Graphs of the autocorrelation and optical spectrum of the VECSEL pulse train used for THz generation. 128
8.8 A THz image of a circular hole in a metal target, and a photograph of the target for comparison. 130

8.9 A THz image of a foil F mounted on plastic, and a photograph of the target for comparison. 131
8.10 A photo of a pigs larynx set in wax and a THz image from the VECSEL system and from a Ti:sa system. 132

List of Tables

2.1 A table showing several important materials for VECSELs and their thermal conductivity. 30

6.1 A table showing the pulse durations, optical spectrum width (FWHM) and the number of times the Fourier limit the pulse is, for the three different pulse regimes explored in this work. This also shows the expermentally measured buildup time and the number of round trips inside the laser cavity this relates to. 84

6.2 A table showing the parameters estimated or measured for SESAMs from the previous work described described by Hoogland [1], and those used in this work, as estimated for the SESAM when the laser is producing 2.5 ps pulses. Further details of the properties of SESAM QT1627 can be found in 5, where the full characterisation of the SESAM is described. 87

Acknowledgements

I would like to acknowledge the many people that have helped and supported this work in many ways. I am indebted to my Supervisor, Professor Anne Tropper, who has always been there to encourage perseverance and to talk through the progress being made, as well as working out strategies to solve technical issues with experiments as well as discussing and understanding the results we obtained.

I would also like to thank all the group members I have worked with over the years, Sjored Hoogland and Kestutis Veskiusis who were nearing the end of their Phd's when I started and whose patience and encouragement were invaluable to gaining the basis of skills and understanding in the subject to allow me to pursue my own projects in the following years. Thanks to Hannah Foreman who has been working on linked projects over the same period and finally thanks to Zakharia Mihoubi and Steven Ellsmere, who recently joined the group.

Thanks to all the support staff, the workshop people who produced beautiful pieces of equipment such as the stable laser base and casing, the teaching lab technicians for allowing me to borrow equipment for longer than I should, and to the lab support technicians for all their help.

Thanks to all the researchers under the Quantum Functional Matter umbrella for sharing their research and ideas for my work.

Thanks to my family and friends for their support and interest.

Finally my biggest thanks to my wife, Stacey, who has been there through the elation, frustration, stress and has put up with me 'physics babbling' to her.

To Stacey

Chapter 1

Introduction

1.1 The Vertical Cavity Surface Emitting Laser

Semiconductor lasers have achieved high output power through edge-emitting array design and circular TEM_{00} output beams from Vertical Cavity Surface Emitting Laser (VCSEL) technology, at low output powers of typically only a few mW [2], [3]. The Vertical External Cavity Surface Emitting Laser (VECSEL) can produce both high output power and good beam quality from a semiconductor gain structure [4] [5]. VECSELs achieve this through optically pumping a semiconductor gain structure and utilising an external cavity to produce good beam quality, although there has been work done, mainly by Novolux, to produce electrically pumped versions (NECSELs) [6] [7].The gain structure is made up of several quantum wells in an active region with a semiconductor multilayer mirror behind it. VECSELs have many of the advantages of semiconductor lasers in terms of their wavelength engineering and growth technology.

VECSELs are power scalable [8] and can be passively mode locked [9], exploiting the external cavity in a fashion similar to thin disk solid state lasers [10] [11]. They take some of the best features in terms of flexibility and advanced applications from solid-state laser cavity design and combine this with the advantages of semiconductor lasers, whilst avoiding the problems of dealing with electrical pumping and the typical extremely elongated output beams of edge emitting semiconductor lasers.

VECSELs are a relatively new laser technology, with the potential for this type of laser first shown by Kuznetsov et al [4] [5]. In this work they reported a VECSEL producing 0.5W in a TEM_{00} beam with a conversion efficiency of greater than 30%. There were many reports of optical pumping in previous work, which was often viewed as a report of a poor electrically pumped structure. The potential advantages of optical pumping semiconductor lasers had previously been recognised in works such as [12].

The work reported by Kuznetsov sparked intense interest in the field of VECSELs, and these lasers have since been shown to have unique advantages over other semiconductor lasers as well as diode pumped solid state lasers. The following sections will describe the distinguishing characteristics of the VECSEL and describe some potential niche applications.

1.2 Comparison of semiconductor laser technology and VECSELs

Diode lasers can be designed to generate high power or single transverse mode beams. They are also renowned for their reliability, efficiency and compact size. Edge emitting diode lasers do, however, have several drawbacks. The single largest drawback to diode lasers is that they suffer from elongated output beam profiles. Commercial narrow stripe edge emitting lasers can achieve CW output powers of 0.3-0.4W in a single transverse mode. High power is achievable in wide stripe lasers, typically in the range of 1-3W commercially available, with multi-transverse-mode output. Even higher CW output power of up to 100s of Watts is available from edge-emitting diode lasers by forming an array of wide stripe lasers. These, however, suffer from low brightness output beams which are characterised by large M^2 values.

The drawback of the strongly asymmetric output beams can be overcome by using elaborate beam reshaping optics for most applications, although a Gaussian beam profile is difficult to achieve and it is more common to obtain a circular top hat type of beam profile from a reshaped output of an edge emitting diode laser. Beam reshaping cannot however reduce the M^2 value of the beam from a multi-transverse-mode laser.

Diode lasers have been used for many applications and have been mode locked with the use of both external cavities and monolithic integrated devices, producing pulses of typically a few ps [13]. The pulses can then often be externally compressed and final pulse duration after compression of 200fs has been achieved [14]. Pulse durations of 393fs [15] and 190fs [16] have been achieved directly from mode locked semiconductor lasers. Monolithic mode locked semiconductor lasers are ideal for very high repetition rate operation due to their integrated size, and repetition rates of up to 100GHz have been readily achieved [17]. Much higher repetition rates, up to 2.1THz, have also been achieved through harmonic mode-locking, or hybrid mode-locking [18]. This harmonic mode-locking is necessary so that the gain region can remain long enough to provide sufficient gain per pass.

VCSELs constitute the other major semiconductor technology with which VECSELs compete. VCSELs are vertically emitting lasers, based on a quantum well active region surrounded with a high reflecting semiconductor multilayer mirror below the active region and a semiconductor multilayer output coupler above the active region. They are electrically pumped and typically have very low laser thresholds, although they are limited to extremely low output powers in the order of 7.5mW in a single transverse mode [2] [3]. The major advantage of the VCSEL, compared to standard wide stripe diode lasers, is that they have the desired circular output beams as well as simple single frequency operation [2]. VCSELs have a very small device diameter of typically only 10μm for single spatial mode operation. Larger device diameters can be used but these operate in a multiple transverse mode output and there are problems with power scaling due to the need to have uniform current flows, and voltages across the device. These large diameter devices can achieve output powers of up to 1.95W [7], in a multimode regime.

VECSELs have many advantages over these other types of semiconductor laser. Many of the advantages come from the fact that the VECSEL uses optical pumping. These include the simplification of the growth and processing of the laser wafer and increased reliability due to there being no need for p-n junctions or electrical contacts. The fact that no p-n junctions are required also means that VECSELs can be grown with

undoped semiconductor materials, which reduces the optical losses associated with free carrier absorption in the multilayer mirror. This is one of the major power limitations for edge-emitting semiconductor lasers and VCSELs. Finally, without current injection in the VECSELs there is no electrical power loss on parasitic resistances that normally have to be eliminated in standard semiconductor devices. Optical pumping removes the need to compromise on the optical properties to ensure that the electrical properties are sufficiently good to produce a high performance device.

VECSELs have the circular Gaussian TEM_{00} output beams of VCSELs with the power ranges that can be achieved in edge emitting diode lasers. The final advantage of VECSELs is the high intra-cavity power. This is often over 50 times greater than the output power which means that efficient intra-cavity frequency doubling can be achieved [8], whereas in edge emitting diode lasers the intra-cavity power is typically of the order of the output power, and the cavities are monolithic, removing the possibility for intra-cavity doubling. An external cavity also makes it easy to introduce other components such as semiconductor saturable absorber mirrors (SESAMS), which are used to mode-lock VECSELs [9]. The application of a high Q cavity with low output coupling also reduces the sensitivity to feedback, which is an issue for edge-emitting semiconductor lasers.

VECSELs do, however, have some disadvantages compared to edge-emitting and VCSEL semiconductor lasers. Optical pumping causes an unwanted heating process through the quantum defect between the pump photon energy and the bandgap of the pump absorption layers in the device. VECSELs are also significantly more complex and expensive compared to other semiconductor lasers due to the need for a pump laser and pump focusing optics, along with an external laser cavity for the VECSEL itself. These extra optics also require mechanically stable construction and VECSELs are therefore bulky compared to other semiconductor lasers. However, for applications where high output power in a TEM_{00} beam are required the disadvantages of extra expense and difficulty of the external cavity and optical pump are outweighed by the advantages that the VECSEL platform offer.

1.3 Comparison of thin disk diode pumped solid-state lasers and VECSELs

VECSELs more closely resemble thin disk diode pumped solid-state lasers than conventional semiconductor lasers. The VECSEL has several distinct advantages over thin disk diode pumped solid state lasers, which split into two groups. The first group is due to the fact that the VECSEL is based on semiconductor technology, which is a mature technology with several different semiconductor material systems already available for use in VECSELs. This means that the VECSEL can have its operating wavelength of the laser chosen by design, and the pump laser wavelength can easily be accommodated in the design process. This is a major advantage compared to working to the constraints of a certain solid-state material. The fact that the gain region in a VECSEL can be designed allows for band gap engineering of the multiple quantum well structures to be used to make desirable properties, such as low laser threshold, high output power and high conversion efficiency. Finally, VECSEL laser principles have been demonstrated over a wavelength range from 391 nm [19] up to 2.36 μm [20].

The second group of advantages that VECSELs have, compared to solid-state lasers, is in the nature of the pump sources. Firstly, the VECSEL gain medium has a broad($> 40nm$)range of acceptable pump wavelengths, so no wavelength stabilisation of the pump source is required, and the pump diode does not need to have a particularly tight wavelength specification. Secondly, the pump absorption length in semiconductors is very short, typically 1-2 μm, which leads to very efficient pump absorption. This is distinctly different from thin disk solid-state lasers that require many passes of the pump, and good mode overlap over large distances, to achieve efficient pump absorption.

Currently for particular applications other laser systems can typically outperform the comparable VECSEL, as VECSEL technology and development is in a much earlier stage compared to the more mature laser systems of edge emitting diode lasers, VCSELs and diode pumped solid-state lasers. CW solid state lasers can reach the kW power level through power scaling of a thin disk design [10] [11]. Many different types of solid state laser have also been mode locked, producing the shortest pulses possible from

any laser source in the case of the Ti:Sapphire laser [21] as well as short pulses from many different gain media, for example [22]. These mode locked solid-state lasers have achieved high powers such as 18W average with 33 fs pulses from a Yb:YAG laser [23] and have demonstrated extremely high repetition rates up to 160 GHz [24]. With further development VECSELs have the potential to perform as well as, if not better than many of the competitive laser systems on some characteristics, particularly mode locked applications at very high repetition rates. There are also the added advantages that VECSELs have the wavelength flexibility of semiconductor lasers, are relatively cheap compared to diode pumped solid-state lasers and are compact. The latest power scaling results such as [8] also show promise for the future of CW operation of VECSELs competing with that of solid-state lasers.

A disadvantage of VECSEL lasers compared to solid-state lasers is the temperature sensitivity of the gain, which reduces rapidly with increasing temperature. This leads to the critical need for good thermal management for high power VECSELs whereas solid-state lasers are relatively temperature insensitive.

1.4 Key results achieved for VECSELs and the work reported in this Thesis

VECSEL technology has been demonstrated over a range of operating wavelengths from 391 nm [19] to 2.36 μm [20]. Here I highlight the major CW laser results achieved, grouped by semiconductor material types. Much of the work to date has focused on GaAs/AlGaAs based systems with InGaAs quantum wells. This material system has allowed VECSELs to be demonstrated over the wavelength range from 950 nm to 1040 nm, and this material group contains the majority of the high power results. This material system has been the testing ground for most VECSEL principles, due to the extensive experience many growers have with these materials, allowing for high quality, predictable sample growths to be achieved. The groundbreaking work by Kuznetsov et al [4] at 1 μm produced over 0.5 W CW and sparked the current intense research in the field. Since then, the main aim for CW lasing VECSELs has been for higher

output power, with over 8W being demonstrated at 989 nm by Lutgen et al [25] in 2003, achieved using substrate removal. More recently, 30 W has been achieved using similar processing, also at 980 nm, by Chilla et al [8]. Other important results for this wavelength have included >400 mW demonstrated directly from an unprocessed sample [26], and over 2.2W at 950nm [27] from a processed sample. Over 2.5 W has been produced at 980 nm from a laser using a diamond heatspreader, which represents the other approach to high power outputs [28]. More recently, in-well pumping has been demonstrated with a sample using a pump regeneration cavity inside the gain sample, demonstrating optical to optical efficiencies of greater than 35% with 1.9 W achieved at 980 nm. This shows that, with high accuracy sample growth, this method of pumping allows high efficiency, with low quantum defect between the pump photon energy and the emission wavelength of the VECSEL, reducing the heat load on the sample significantly [29]. The approaches to thermal management, which allows power scaling of VECSELs, has also been mathematically modelled [30]. Intra-cavity frequency doubling has also been demonstrated, mainly using 980 nm based VECSELs, with a commercial product, the coherent sapphire, now available on the market (200 mW) [31]. Up to 18 W of 488 nm blue has been produced [8] in the same manner.

VECSEL technology has also been demonstrated at shorter wavelengths, using several different material systems, with GaAs/AlGaAs based quantum wells grown on GaAs substrates being utilised for operation at 830-860 nm, with over 0.5 W demonstrated by Hasite et al, utilising a 660 nm pump laser [32]. An 850 nm VECSEL has also been demonstrated using in well pumping from an 808 nm diode laser. This first result did not have pump recycling and so the efficiency was low, with an output power of 135 nW [33]. In well pumping has also been demonstrated for a VECSEL operating at 660 nm, producing 185 mW of output power [34]. A 650 nm VECSEL has also been demonstrated by Hastie et al in both an external cavity format [35] and a microchip array format [36], These VECSELs were based on an InGaAlP material system. The shortest wavelength demonstrated from a VECSEL, 391 nm, was achieved using an InGaN/GaN based system [19].

Long wavelength VECSELs have been demonstrated as well, with a 1.3 μm laser based

on GaInNAs/GaAs materials producing over 600 mW [37]. VECSELs have been demonstrated at longer wavelengths, in the telecoms range using InGaAs/InGaAsP/InP based systems. Early work produced low power, up to 45 mW at 1550 nm [38], and more recently up to 0.8 W has been demonstrated [39]. The longest wavelength range demonstrated to date with VECSELs has been the 2.1 μm - 2.36 μm range, based on GaInAsSb/AlAgAsSb/GaSb materials. These works have typically been low power with only a few mW demonstrated, for example 5 mW at 2.36 μm [20]

VECSELs have been mode locked to produce ps pulses with a slow saturable absorber [9] and sub 500 fs pulses have been produced by utilising the ac Stark effect [40]. These fs pulses are soliton shaped and the soliton like nature of these pulses has been explained in theory [41]. Mode locked VECSELs have been demonstrated across a broad range of repetition rates from 338 MHz [9] to 30 GHz [42], producing picosecond pulses and from 950 MHz to 10 GHz producing sub 500 fs pulses [43]. Power scaling has also been demonstrated with mode locked VECSELs, with up to 2.1 W being demonstrated producing picosecond pulses [44].

The work reported in this thesis started from a basis of a theoretical sample design program and a characterisation method to assess the sample quality, which has been utilised for some of this work. The first demonstration of 500 fs pulses directly from the laser cavity at a repetition rate of 1 GHz had also been achieved, although the reason why the pulse was not shorter was not understood. In this thesis, I report the first demonstration of pulse split-up and multi-pulse operation of a 500 fs VECSEL in Ch.4. In Ch.7 I report the first mode locked VECSEL that is locked to an external electrical oscillator. The timing jitter and amplitude jitter of a mode locked VECSEL are also characterised here for the first time, showing a reduction in the timing jitter through active stabilisation to 160 fs rms from 400 fs rms over a frequency offset range of 1 kHz to 15 MHz, and is also reported in Ch.7. I demonstrate the first use of a sub-500-fs mode locked VECSEL used to generate THz radiation and report the first THz images taken using a THz imaging system and THz radiation generated by the VECSEL in Ch.8. Finally in Ch.6 I report the first measurements of the mode-locking buildup time for a sub 500 fs pulsed VECSEL and also spectro-temporal measurements during this

onset period, to reveal the evolution of the optical spectrum before mode locking occurs. These measurements have lead to insights to the pulse duration limiting processes and have lead to suggested future sample designs to reduce the pulse length achievable.

Chapter 2

Overview of VECSEL design and Technology

2.1 Introduction

This chapter provides a brief overview of the physical principles that are important for VECSEL gain structure design and performance. We will start with an overview of semiconductors, and then move on to quantum wells, and their optical properties. After this, I describe the design of the VECSEL gain structures, and the different options available, as well as discussing important design principles to tailor the sample characteristics to the desired application. Finally, I will briefly describe some of the issues and work that has been done on heat management, which is of critical importance to achieve high efficiency, high power devices.

A diagram of a typical VECSEL laser cavity used for mode locked operation is shown in Figure 2.1, with a close up view of the structure of the gain structure and the SESAM.

This cavity design has double pass gain, which is useful to overcome the extra losses per round trip associated with the use of a SESAM. The Z cavity design also allows us to control the laser mode size on the SESAM and on the Gain. This is critical to achieve stable mode-locking in different regimes as described in Ch.4.

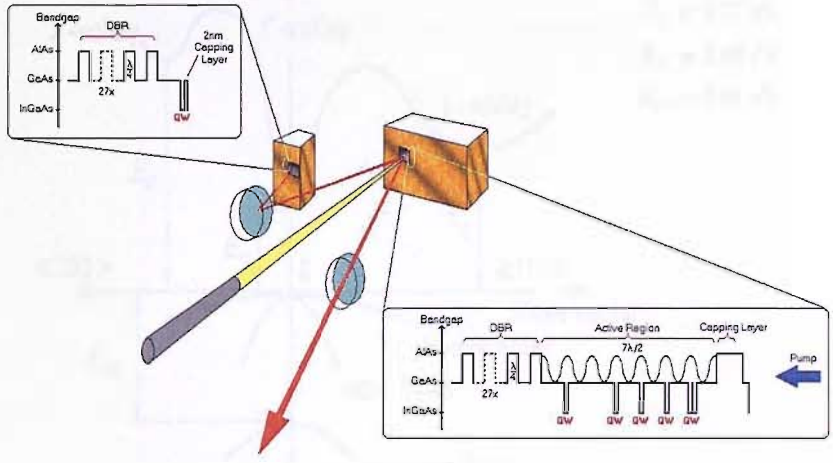

FIGURE 2.1: A schematic of a mode locked VECSEL laser cavity with close up views of the gain region and the saturable absorber. This is the typical cavity that is used in our work, with a repetition rate of typically 1GHz, an output coupler of 0.7%, with a radius of curvature of 50mm and a high reflector with a radius of curvature of 25mm to focus the laser mode onto the saturable absorber.

2.2 Introduction to semiconductors and quantum wells

2.2.1 Semiconductor material properties

Semiconductors provide a set of materials which can be designed and grown to produce many different complex devices. The basis for the usefulness of semiconductors is the existence of an electron bandgap which can be tailored by varying material composition and by controlling the quantum confinement. This is an energy gap that exists between the lowest energy band with unoccupied energy states, the conduction band, and the highest energy band with occupied states, the valence band. The bandgap structure of GaAs is shown below in Figure 2.2 (after [45]). The energy band structure is due to the interaction of an electron interacting with a regular lattice of ions, and can be solved using the Schrödinger equation.

It can be seen that for GaAs the bandgap is a direct bandgap material. This is because the lowest state of the conduction band and highest state of the valence band which produces the smallest possible bandgap, are both located at the same momentum values.

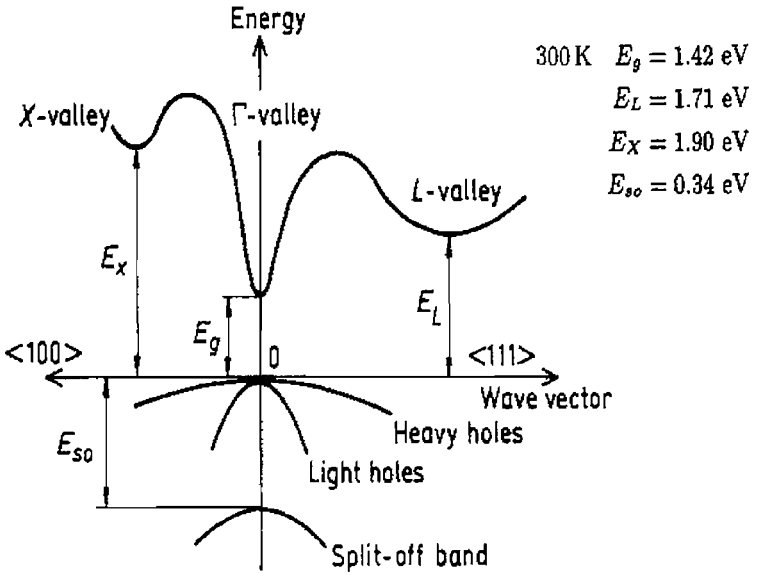

FIGURE 2.2: A diagram showing the conduction band and valence band structure of bulk GaAs. It can be seen that the smallest bandgap is centred around $k = 0$, showing that GaAs is a direct bandgap material as the highest point of the valence band lies directly beneath the lowest point of the conduction band [45].

The fact that GaAs is a direct bandgap material means that its radiative transition probability is high at the band edge, whilst if a material has an indirect bandgap the radiative transition probability is much lower.

III-V semiconductor materials such as GaAs, alloyed with various different group III and group V materials to make a range of material systems with differing bandgap, are the most commonly used for optical devices due to the high optical transition rates of these materials. There are now many different semiconductor alloys which allow a large range of bandgap energies, lattice constants and physical properties to be chosen by changing the alloy, and the relative material contents of each component. Figure 2.3 shows the different alloys of III-V materials that can be grown through standard processes. It shows the bandgap that can be achieved, along with the lattice constant, for varying concentrations of the various components in the semiconductor alloys.

This control of the bandgap through changing the relative concentration of components in the semiconductor alloy allow for bandgaps to be engineered to produce optical transitions in the range from violet [47] to 4.5μm [48]. Structures can be designed for longer

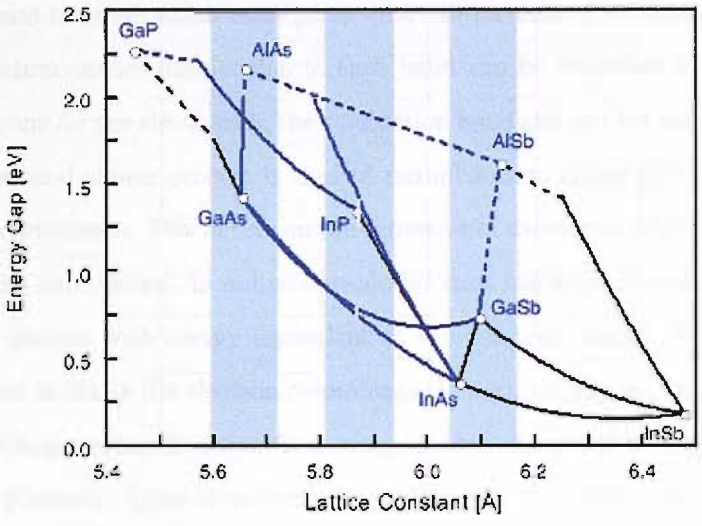

FIGURE 2.3: A diagram showing various III-V semiconductor materials, their band gaps and lattice constants. This shows that the combination of $Al_xGa_{1-x}As$ is lattice matched for all values of x [46].

wavelength but growth difficulties and increasing non-radiative losses lead to the current limit for direct inter-band lasers.

The material systems used must be lattice matched to each other and to the substrate for an efficient device to be produced, as there is strain between layers of non-lattice matched materials. This strain between non-lattice matched layers causes dislocations if the layers are thicker than a critical thickness. Dislocations due to strain in a device cause device degradation over time, leading to lifetime issues. $Al_xGa_{1-x}As$ systems are lattice matched across the whole range of x, allowing for structures consisting of layers of differing bandgap to be grown on GaAs substrates, with no strain introduced.

2.2.2 Carrier distribution and optical properties for semiconductor materials

When an electron is excited into the conduction band there are several processes which may occur, leading to recombination, either radiativly or non-radiativly. The first process to occur when an electron is excited into the conduction band is that of intra

band thermalisation. This is where the electrons are thermalised first through carrier-carrier scattering and then the excess energy is lost through carrier-phonon scattering. This intra band thermalisation takes place on a sub-picosecond timescale. The thermal quasi-equilibrium carrier distribution in each band can be described by a Fermi-Dirac distribution, one for the electrons in the conduction band and one for holes in the valence band. The second slower process is that of recombination either through radiative or non-radiative processes. This occurs on the timescale of the carrier lifetime, which is typically around a nanosecond. In radiative recombination the electron and hole recombine, producing a photon with energy equivalent to the bandgap energy. For non-radiative recombination in GaAs the electron recombines through the lattice, impurities, defects and through Auger recombination. The energy is then dissipated through lattice vibrations called phonons. Once true thermal equilibrium is reached, a single Fermi-Dirac distribution, given in Eq.(2.1), can be used to describe the probability of an electron being in an energy level, E:

$$f(E) = \frac{1}{1 + e^{(E-E_F)/k_B T}}, \tag{2.1}$$

where E_F is the Fermi level, which is a function of total carrier density and temperature, T.

When more carriers are forced into the conduction band through pumping, the spontaneous emission rate increases, the point where the material becomes transparent to an incident photon with energy equalling the bandgap can be reached. At transparency there is no net gain or absorption as both processes occur with equal probability. If the pumping level is increased further a population inversion can be produced, leading to optical gain.

The total carrier density, N_α, can be determined by the Fermi level and the density of states [49] and is shown in Eq.(2.2):

$$N_\alpha = \int_0^\infty \rho_\alpha(\epsilon_\alpha) f(\alpha)(\epsilon_\alpha)\, d\epsilon_\alpha, \tag{2.2}$$

where $\rho_\alpha(\epsilon_\alpha)$ is the energy density of states. f_α is the Fermi-Dirac distribution of the carriers.

Another feature is that the electron and hole can form a bound state called an exciton under some conditions. These excitons are formed due to Coulomb interaction between the electron and hole. They are experimentally observed at low temperatures and for low excitation levels. The exciton binding energy is small compared to the bandgap energy and gives rise to a peak in the absorption spectra of bulk semiconductor under these conditions.

In the regimes in which VECSEL gain structures operate, the exciton peak is, however, not observed. This is due to two different mechanisms. The first is that at room temperature the thermal energy, k_BT of the carriers is greater than the exciton binding energy, resulting in ionisation of the exciton. The second is that at high carrier densities the Coulomb potential of the electron and hole becomes screened, leading to ionisation of the exciton.

2.2.3 Quantum wells and quantum confinement

2.2.3.1 Introduction to quantum confinement

The carrier density needed to reach transparency and hence laser threshold for a semiconductor can be reduced by controlling the dimensions of the amplifying medium. Semiconductor growth processes allow for layer thicknesses to be controlled down to the atomic scale. This allows for the confinement of the carriers to be controlled, leading to four distinct types of semiconductor gain medium, relating to the degree of quantum confinement: three dimension bulk material, quantum wells, a two dimension material, quantum wires, a one dimension material and quantum dots, a zero dimension material. In this work we use quantum wells. A diagram of the different levels of confinement and the effect this has on the density of states of the material is shown in Figure 2.4 [50].

Increasing the confinement from bulk material to a Quantum well leads to quantum effects dominating the density of states and the band structure. This allows the emission

wavelength of photons from a quantum confined material to be accurately controlled through design of the dimensions of the confinement.

The shape of the conduction and valence bands can be approximated by parabolic curves given by Eq.(2.3):

$$E_{c,v} = \pm \frac{\hbar^2 k_\perp^2}{2m_{c,v}}, \tag{2.3}$$

where $m_{c,v}$ is the electron mass in the conduction band (c) or the heavy hole mass in the valence band (v). The momentum perpendcular to the well, $k_\perp$, is given by Eq.(2.4):

$$k_\perp = i\frac{2\pi}{L_\perp}, \tag{2.4}$$

where $L_\perp$ is the thickness of the well and i is an integer.

The number of allowed transitions within a certain energy interval, the joint density of states, equals the density of states in either the conduction or valence band and is given by Eq.(2.5):

$$\rho_{c,v}^{QW}(E) = \frac{m_{c,v}}{2\pi\hbar^2}\frac{1}{L_z}\sum_{i=0}^{N_l} Step(h\nu - (E_{c_i} - E_{v_i})), \tag{2.5}$$

where N_l is the number of sub-band levels and the parabolic band approximation is used and the *Step* function makes the joint density of states a step function.

In this work the quantum wells are designed to have a transition wavelength of about 1030nm. The active region consists of GaAs spacer barriers and $In_{0.23}Ga_{0.77}As$ quantum wells. This choice of InGaAs alloy and GaAs barriers leads to compressive strain as the lattice constants are different for each. Strain is a useful feature, as it causes the peak gain and differential gain to increase compared to an unstrained quantum well [51]. The strain does, however, shift the bandgap frequency and this must be taken into account at the design and growth stage. The cumulative effect of the strain is to cause shear forces between the layers, creating an unstable structure if the thickness of the strained

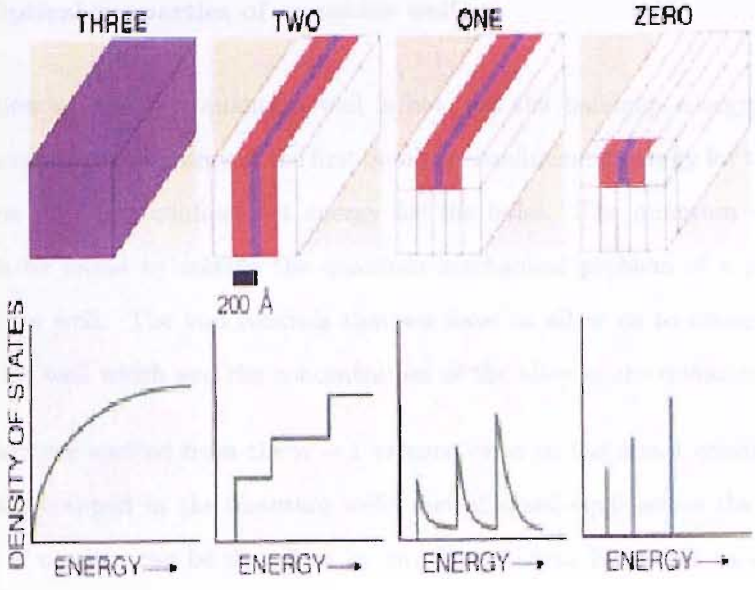

FIGURE 2.4: A diagram showing the density of states for a 3 dimensional material (bulk), a 2 dimensional material (quantum well), a 1 dimensional material (quantum wire) and a 0 dimensional material (quantum dot) [50]

layers exceeds the critical thickness. The critical thickness is a measure of how thick a layer of a certain lattice constant mismatch can be grown before dislocations occur at the layer interface. The end result of too much strain over an entire structure is that it will rapidly degrade over time as dislocations form, rendering the structure unusable. The compressive strain of the quantum well is of the order of 1% difference in lattice constant.

The long term problems of strain can be avoided by the introduction of strain compensation layers on each side of the quantum well. These layers consist of $GaAs_{0.94}P_{0.06}$ and have tensile strain. The widths of the strain compensating layers are chosen to completely balance the effects of the compressive strain from the quantum well that they surround. In this strain balance condition, the net strain across the entire structure is zero [51]. The strain compensating layers have a bandgap which is 54meV higher than that of the GaAs barriers. This leads to a small potential barrier, which is about twice the thermal energy, k_BT, of the electrons in the barriers. This potential barrier would reduce the carrier capture efficiency and slightly increase the laser threshold, although this effect does not significantly impair the laser performance.

2.2.3.2 Optical properties of quantum wells

The transition energy in a quantum well is not just the bandgap energy, but is the bandgap energy plus the energy of the first quantum confinement energy for the electrons plus the first quantum confinement energy for the holes. The quantum confinement energies can be found by solving the quantum mechanical problem of a particle in a finite quantum well. The two controls that we have to allow us to choose transition energy are the well width and the concentration of the alloy in the quantum well [51].

When carriers are excited from the $n = 1$ valence band to the $n = 1$ conduction band they are then trapped in the quantum wells and at quasi-equilibrium the occupation probability of carriers can be described by two Fermi-Dirac functions, as described in Eq.(2.1), one for the conduction band and one for the valence band. The Fermi levels for these functions can be calculated by solving Eq.(2.2), using the density of states of the conduction band and the valence band, given by setting $i = 1$ in Eq.(2.5). The Fermi levels are given by Eq.(2.6) and Eq.(2.7):

$$E_{F_c} = kTln(e^{\frac{N\pi\hbar^2 L_z}{m_e kT}} - 1) \tag{2.6}$$

$$E_{F_v} = kTln(e^{\frac{N\pi\hbar^2 L_z}{m_h kT}} - 1) \tag{2.7}$$

The radiative transition rate, the transition probability per second per unit volume of the active material is shown in Eq.(2.8) [51]:

$$R_r = \frac{1}{2}\frac{e_o^2\lambda}{c\epsilon_0 M_e^2 n^2} N_p \left|M_T\right|^2 \rho_J^{QW}(\hbar\omega), \tag{2.8}$$

where N_p is the number of photons per unit volume and $\rho_J^{QW}(\hbar\omega)$ is the joint density of states given by Eq.(2.5) where $m_{c,v}$ has been replaced by the reduced mass, m_r. $|M_T|^2$ is the transition matrix element of the gain medium.

The stimulated emission rate can then be written as the probability of finding an electron in the conduction band and a hole in the valence band at a given wave vector times the radiative transition rate Eq.(2.9), conversly the stimulated absorption process is given in Eq.(2.10):

$$R_{SE} = R_\tau f_c(1 - f_v) \tag{2.9}$$

and

$$R_{SA} = R_\tau f_v(1 - f_c), \tag{2.10}$$

where the Fermi-Dirac distributions have the form shown in Eq.(2.1).

The quantum well gives gain when the stimulated emission rate is larger than the stimulated absorption rate. The material gain per unit length can then be written as Eq.(2.11) and is defined as the net growth of the photon density as it propagates along some direction, z, in the medium:

$$g = \frac{1}{2}\frac{e_0^2\lambda}{c^2\varepsilon_0 m_e^2 n}|M_T|^2 \rho_J^{QW}(\hbar\omega)(f_c - fv), \tag{2.11}$$

where the standard symbols are used for constants and n is the refractive index. It is important to note that the material gain is not the effective gain of the device, which is given by the intensity in the gain medium as well as the material gain. The intensity distribution is a function of the VECSEL gain sample design and is called the longitudinal confinement factor and will be discussed in more detail in 2.3.

Eq.(2.11) assumes no intra-band scattering to broaden single electron transitions, and so the gain spectrum produced has a sharp cut-off edge at the long wavelength end of the spectrum. Intra-band scattering has a large effect on the band edge shape, broadening the edge. The total gain is a convolution of the gain given in Eq.(2.11) and a lorentzian linewidth function, describing the broadening due to intra-band scattering.

Eq.(2.11) also does not take into account Coulomb effects and bandgap renormalisation effects. These change the shape of the gain spectra to some extent, along with several other effects, described in [49]. Eq.(2.11) does however give a good basis for estimating the peak value of gain as 0.6% perpendicular to the plane of the well and the transparency carrier density as $0.88 \times 10^{18} cm^{-3}$, which is in line with expected values for several quantum well systems.

The laser cavities used in this work have approximately 2% loss per round trip. The maximum theoretical gain of a quantum well is 0.6% [1] and we use six quantum wells in the gain samples.

2.2.3.3 Non-radiative decay mechanisms in semiconductor quantum wells

In 2.2.2 it was stated that there are several different ways that an excited electron in the conduction band can relax back to the valence band. These split into two groups, radiative and non-radiative recombination. In a semiconductor system designed for its optical properties any carriers recombining through non-radiative processes cause a loss in efficiency. The probabilities for the different recombination processes is given by the inverse of their respective lifetimes.

For most semiconductor optical devices the relaxation rate of carriers is given by Eq.(2.12),

$$\frac{N}{\tau_{level}} = A_d N + \frac{BN^2}{L_{QW}} + C_A(\frac{N}{L_{QW}})^3, \tag{2.12}$$

where L_{QW} is the width of the quantum well. A_d is a constant which represents the density of defects in the quantum well. This value is inherently low due to the advanced growth techniques that can be used leading to very low defect concentrations under optimal growth conditions of less than 10^{16} cm^{-3} and more typically as low as 10^{15} cm^{-3}. C_A is the Auger coefficient and represents the largest non-radiative loss mechanism. An example of this effect is where the released energy from an electron that is recombining is absorbed by another electron in the conduction band, forcing this electron high into the conduction band. The excess energy of this electron is then lost through the emission

of phonons and lattice vibrations. The strength of the Auger effect is dependant on the carrier density and it is also temperature dependant. This in turn means that it is important to design samples with good thermal characteristics to minimise the effect of local heating increasing the non-radiative recombination rate. It is also important to design the laser to have a low threshold as this reduces the total carrier density and hence the non-radiative recombination losses. This is particularly important as the strength of the Auger effect scales as carrier density squared.

B is the radiative recombination coefficient and the radiative recombination rate is directly proportional to the carrier density. The radiative recombination rate can be expressed as Eq.(2.13):

$$\frac{1}{\tau_{rad}} = \frac{BN}{L_{QW}}. \tag{2.13}$$

The quantum efficiency of spontaneous emission of the quantum well can then be expressed as the lifetime of radiative recombination compared to the total lifetime of recombination as Eq(2.14):

$$\eta_i = \frac{\tau_{level}}{\tau_{rad}}. \tag{2.14}$$

The quantum efficiency near transparency is high, typically around 80%, whereas as the carrier density increases the non-radiative Auger process increases faster than the radiative processes, and the overall quantum efficiency of the quantum well decreases. This shows that good sample design for low threshold and low temperature dependence are important to ensure that the samples remain efficient, with optical transitions dominating the recombination processes.

2.3 Design of VECSEL gain structures

A diagram of the 'active mirror' is shown below in Figure 2.5, it shows the bandgap of the materials versus distance through the sample. The sample contains an active region

with 6 InGaAs strained quantum wells with InGaP strain compensation layers and GaAs spacer layers. For simplicity the strain compensating layers are not shown in Figure 2.5 but these are 28.2 nm thick layers of $GaAs_0.94P_0.06$ which are located directly on either side of each quantum well. GaAs is used as the spacer layers to absorb the 830nm pump light and produce carriers that then fill the quantum wells. The quantum wells are located at antinodes of the E-field, to maximise the coupling between the photons in the laser cavity and the quantum wells. The active region is surrounded by a distributed bragg reflector (DBR) on one side. A DBR is made up of $\lambda/4$ thickness alternate layers of AlGaAs/GaAs or AlAs/GaAs. There is a window layer on the other side of the active region and this allows the microcavity enhancememt factor to be controlled, by setting the strength of the E-field inside the sample. Finally on the top surface a small capping layer is used to remove the problem of oxidation in the window layer. All of the gain samples used for this work are MOVCD grown by John Roberts. These lasers are designed to operate at a wavelength 1035nm.

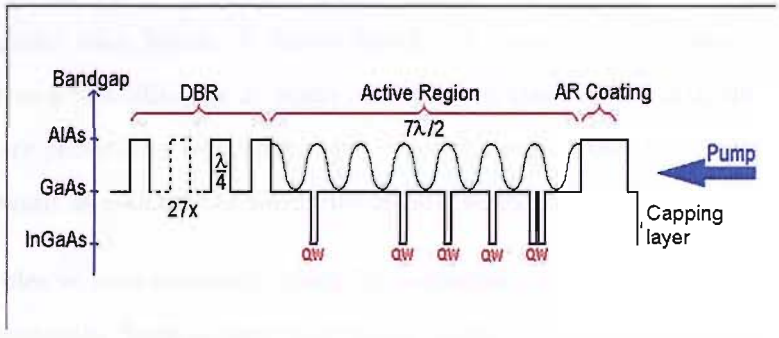

FIGURE 2.5: A diagram of a typical VECSEL gain structure showing the essential design components; the DBR high reflector, the active region, with the quantum wells located at the antinodes of the e-field standing wave, the window layer which controls the strength of the coupling of the e-field outside the gain sample to that in the active region and the capping layer, which is necessary to stop oxidation of the surface.

The earlier samples use GaAs/AlAs in the DBR, which causes pump absorption in the GaAs layers of the DBR. More recent designs have avoided this problem by using $Al_{0.2}Ga_{0.8}As$/AlAs layers to make the DBR. This does have the disadvantage of reducing the index contrast in the DBR, but this is not a significant problem for the reduction in temperature sensitivity gained.

The quantum wells are designed to emit at 1020nm at room temperature and low pump power. This means that when pumped with 1W of pump power, the peak of the gain

shifts to longer wavelength as the active region is heated by a proportion of the absorbed pump power, due to the mismatch between the pump photon energy and the bandgap energy of GaAs. This excess absorbed energy produces heat through lattice vibrations. This shift is usually 0.3nm/K and under high pump power conditions the peak of the emission from the quantum wells is shifted to 1035nm. This shows that the region being pumped on the gain sample is locally heated by about 70^0C. Six quantum wells were chosen for this design to provide a good balance between low lasing threshold, high output power, thermal issues and gain bandwidth considerations.

The DBR is designed to have its stop band centred on the design laser wavelength of 1035nm as shown in Figure 2.7. The DBR is made up of 27.5 pairs of GaAs/AlAs $\lambda/4$ layers and is designed to have a reflectivity at the design wavelength of greater than 99.98%. Figure 2.6 shows a schematic of a simplified DBR, showing the electric field of the incident light diminishing as it passes through each $\lambda/4$ layer, showing that the light is reflected. Figure 2.7 shows the stop band of the DBR for three different numbers of pairs of quarter wave layers. It shows that for 15 pairs the reflectivity is too low for application in a VECSEL. For 27 layers and 35 layers there is very little difference, with the necessary reflectivity reached in both cases. To ensure that the design remains as straightforward as possible the minimum number of layers is used.

In our samples we have assumed a pump light absorption pattern across the active region with an exponential decay as described by the Lambert-Beer law. This means that more carriers are produced near the surface of the active region than closer to the DBR. We have distributed our quantum wells in an imbalanced way to reflect this, with 2 quantum wells located at the first intensity antinode, and an empty space near the rear of the active region. This is shown to theoretically produce an even carrier distribution in each of the six quantum wells as shown in Figure 2.8 from Hoogland [1].

Methods have been suggested to further improve the carrier distribution between the quantum wells by placing barriers in the pump absorption regions to force carriers produced in particular areas to go to particular quantum wells [52]. Some sample designs used by other groups use a symmetric pattern for their layout of quantum wells [53],

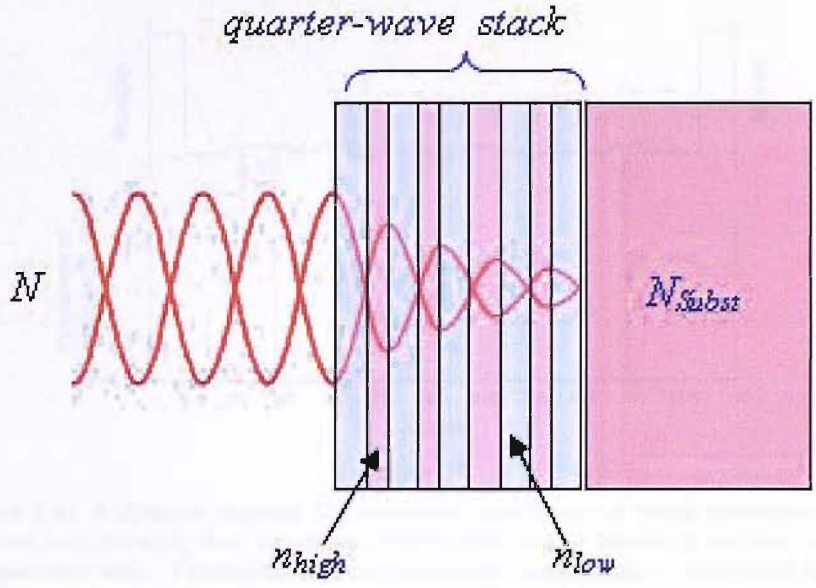

FIGURE 2.6: A diagram of a Distributed Bragg Reflector showing the alternating layers of high and low refractive index and the decreasing e-field amplitude through it. It is important to note the antinode on the top surface of the DBR, which then sets the standing wave pattern in the active region that is grown on top of this for gain structures.

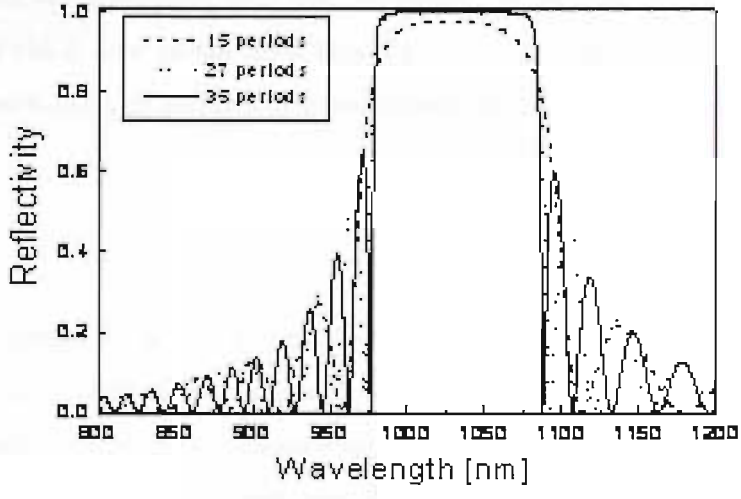

FIGURE 2.7: Calculated reflectivity curves for a Distributed Bragg Reflector with different numbers of GaAs/AlAs pairs. It can be seen that for the combination of GaAs/AlAs 27 pairs is of $\lambda/4$ layers are necessary to produce the required reflectivity of 99.9% over a reasonable range. A DBR containing fewer layers significantly reduces the total reflectivity, whilst a DBR with more layers unnecessarily increases the growth complexity.

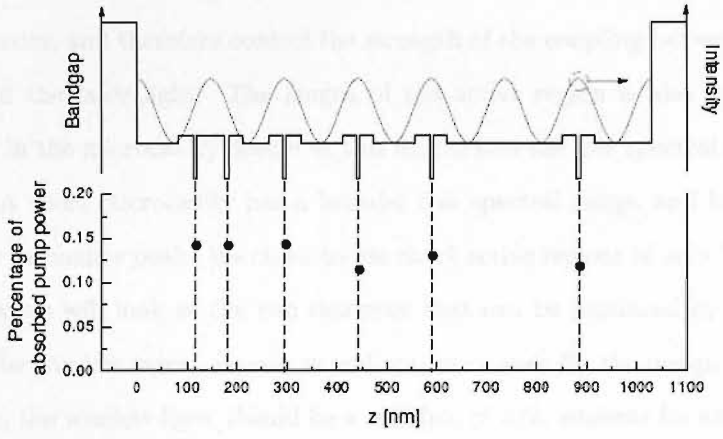

FIGURE 2.8: A diagram showing the theoretical percentage of pump absorption per quantum well, showing that the carrier distribution should be nearly uniform across all 6 quantum wells. This calculation assumes an exponential pump absorption in the active region, with the carriers being trapped before they have time to redistribute through diffusion across the whole active region [1].

believing that the carriers quickly redistribute across the whole active region through diffusion processes.

The total device gain of a VECSEL gain structure is given by a combination of the material gain of the quantum wells and the intensity of the E-field on those wells. The intensity of the E-field on the wells depends on the microcavity that surrounds the quantum wells, and this microcavity enhancement can be calculated using Eq.(2.15):

$$\Gamma_z = \frac{\sum_q |E(z_q)|^2}{|E_0|^2}, \tag{2.15}$$

where the summation is over all the quantum wells in the structure, $|E(z_q)|^2$ is the squared modulus of the E-field amplitude at the position of the q^{th} well, calculated by standard multilayer matrix calculations and $|E_0|^2$ is the squared modulus of the E-field in air. The total device gain is then given by Eq.(2.16),

$$Gain = g \times \Gamma_z, \tag{2.16}$$

Where g is the material gain from Eq.(2.11).

The thickness of the window layer can be used to control the strength of the resonance of the microcavity, and therefore control the strength of the coupling between the quantum wells and the laser light. The length of the active region is also an important consideration in the microcavity design as this length sets the free spectral range of the microcavity. A short microcavity has a broader free spectral range, and hence a spectrally broader resonance peak. We chose to use short active regions of only $7\lambda/2$ for this reason. Below we will look at the two extremes that can be produced by altering the thickness of the window layer: resonance and anti-resonance for the design wavelength. For resonance, the window layer should be a multiple of $\lambda/2$, whereas for anti-resonance it should be a multiple of $\lambda/4$ thickness at the design wavelength.

For maximum output power the sample should be designed so that the microcavity reaches a resonance at the design wavelength. If this is done the enhancement factor of the coupling between the photons and the carriers is of the order of 3. This increase in coupling, and hence overall gain from the active region does, however, have implications on the gain bandwidth, which is filtered by the resonance bandwidth of the microcavity as shown in Figure 2.9 [1]. Most high power results such as [8] rely on this enhancement by the microcavity resonance, long microcavities and many (10 - 20) quantum wells, along with other processing steps as discussed in 2.4.

The use of an anti resonant microcavity to increase the bandwidth of the gain structure does, however, have the disadvantage that the intensity on the quantum wells is reduced to approximatly 0.4. This reduction in intensity on the quantum wells means that there is a much weaker coupling between the carriers in the quantum wells and the photons resonating in the laser cavity. This reduces the effective gain of these gain samples substantially and means care must be taken to reduce all other losses as much as possible. Thus for high power VECSELs utilising resonant microcavities output coupling of 2-4% is not uncommon [8], whereas for VECSELs based on anti resonant structures output coupling of only 0.7% is typical [40].

In the case of using a VECSEL to produce the shortest pulses available, the microcavity must be designed to not limit the intrinsic gain bandwidth from the quantum wells. To achieve this, the microcavity is designed to be near-anti-resonant at the laser wavelength,

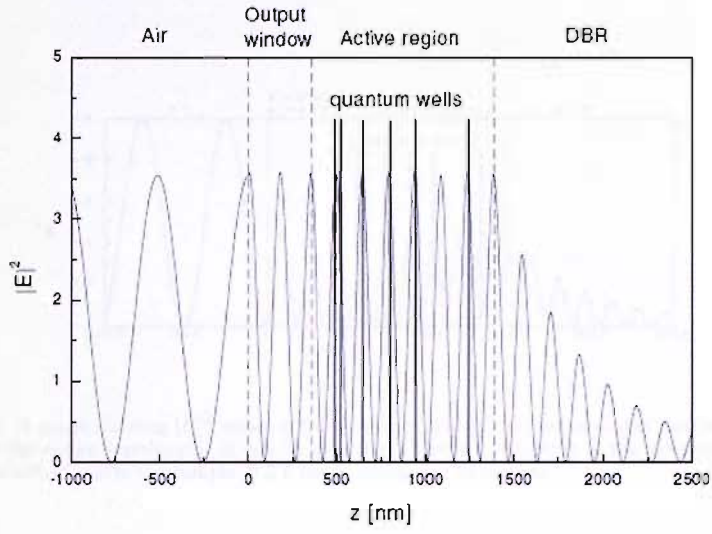

(a) A graph showing $|E|^2$ verses optical distance through a resonant gain sample at the design wavelength. It can be seen that there is no reduction in the magnitude of the e-field inside the sample, compared to outside.

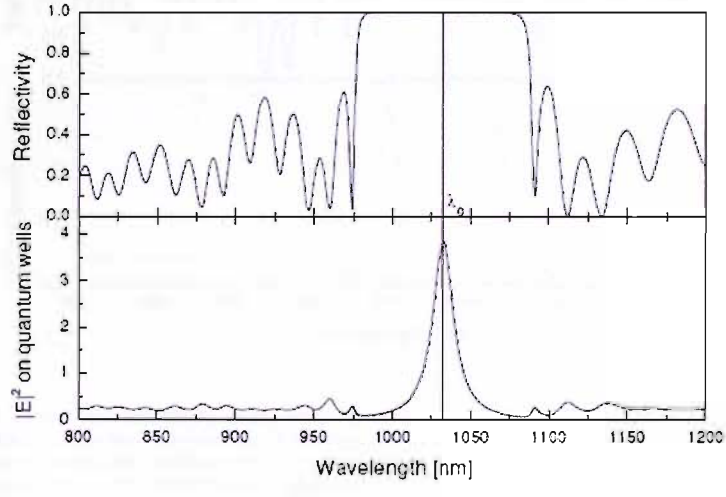

(b) Theoretical reflectivity curve and a graph showing the variation of $|E|^2$ on the quantum wells with wavelength. This shows a narrow resonance around the design wavelength, peaking up to a maximum value of nearly 4.

FIGURE 2.9: Diagrams showing the magnitude of $|E|^2$ with position in the sample, and also with wavelength for the quantum wells. These show a resonant enhancement of the $|E|^2$ at the design wavelength, and also show the narrow filter function imposed on the gain spectrum due to this. These graphs are calculated using a modeling program, developed previously in our group, based on standard multilayer techniques .

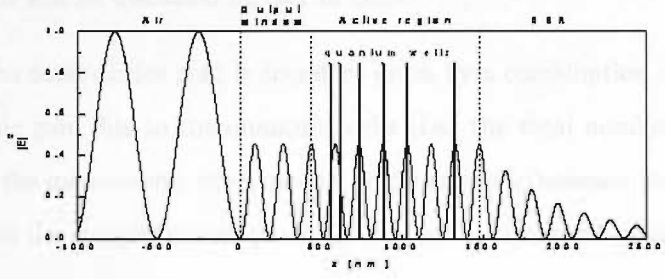

(a) A graph showing $|E|^2$ verses optical distance through an anti resonant gain sample at the design wavelength. It can be seen that there is a reduction in the magnitude of the e-field inside the sample of 2.5 times, compared to outside.

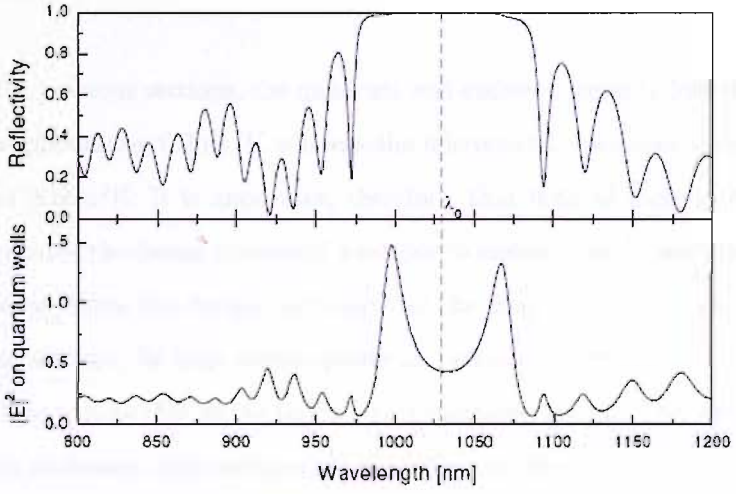

(b) Theoretical reflectivity curve and a graph showing the variation of $|E|^2$ on the quantum wells with wavelength. This shows a broad trough between two peaks at the design wavelength, leading to the microcavity not filtering the gain strongly as in the resonant case. The e-field on the quantum wells reaches a value of approximately 0.5 at the design wavelength, showing that the gain bandwidth is increased at the expense of the total device gain.

FIGURE 2.10: Diagrams showing the magnitude of $|E|^2$ with position in the sample, and also with wavelength for the quantum wells. These show an anti resonant design structure, showing the spectrally flat filter function across the design wavelength region, and also the trade off in effective device gain.

leading to a spectrally broad gain region which has a broad flat filter function imposed onto it as shown in Figure 2.10. This can allow the entire gain bandwidth to be exploited as there is nearly uniform gain across a large wavelength range. The importance of the gain bandwidth will be discussed further in Ch.4

In summary the total device gain is therefore given by a combination of factors including the intrinsic gain due to the quantum wells (i.e. the total number of wells), their positioning in the microcavity, the strength of the coupling between the photons in the laser cavity and the carriers in the quantum wells at the designed emission wavelength.

2.4 Power scaling of VECSELs and the importance of heat removal

As discussed in previous sections, the quantum well emission tunes to longer wavelength at a rate of approximatly 0.3nm/K whereas the microcavity resonance tunes at a much slower rate of 0.1nm/K. It is important, therefore, that both of these shifts are taken into account during the design process of a sample to ensure that the gain peak from the quantum wells matches the design wavelength of the microcavity for high pump power and room temperature, for high output power and efficient operation to be achieved. It is also important to note that as the temperature increases, the quantum efficiency of the quantum wells decreases. Any increase in local temperature above that accounted for by design, leads to the quantum well gain reducing and tuning away from the microcavity design wavelength, which is experimentally seen as thermal rollover of the laser. For the unprocessed samples discussed here thermal rollover is the major power limiting factor. Much work has been done by other groups to minimise the increase in local tempreature due to pump absorbtion away from the active region and the quantum defect between the pump wavelength and the emission wavelength. It is this efficient removal of heat from the active region that has allowed VECSELs with output powers as high as 30W to be demonstrated [8].

Due to the total thickness of the active region being in the order of 20μm, the heat flow through the active region is in theory one-dimensional as shown in Figure 2.11.

Material	Thermal Conductivity $\kappa(\mathrm{WK^{-1}m^{-1}})$
GaAs	45
AlAs	91
$Al_{0.5}Ga_{0.5}As$	11
Cu	400
CVD diamond	1000-1800
Composite diamond	600
Copper-Tungsten W-10	180
Al_20_3	44
SiC	490
In	82
Ti	22
Pt	71
Au	315

TABLE 2.1: A table showing several important materials for VECSELs and their thermal conductivity.

This should allow for simple power scaling of the VECSEL technology platform [5]. To increase the output power it should be a simple case of increasing the pump spot size, as the total incident pump power is increased without raising the temperature of the active region.

In reality however this is not the case due to the active region being grown on a thick GaAs substrate in the order of 500 microns. GaAs has a relativly high thermal resistivity, which means that whilst the thick substrate allows for lateral heat flow away from the pump area as well as directly through the substrate, the heat which is deposited cannot be removed fast enough, leading to thermal rollover. The problem of thermal rollover increases for an unprocessed sample as the pump spot size and incident pump power is increased whilst attempting power scaling due to the fact that more of the centre of the spot, where a majority of the excess heat is deposited, only sees an one dimensional heat flow. As an example of this, the limiting factor on the output power of the VECSELs we use for this work is the local heating effect as the pump power is increased, leading to thermal rollover. The thermal conductivity of several materials important to VECSEL processing are shown below in Table 2.1, where it can be seen that GaAs and $Al_{0.5}Ga_{0.5}As$ have particularly poor thermal conductivities, leading to large local temperature increases for relativly small amounts of heat deposited.

The main sources of heat in our samples are heating effects due to the quantum defect

between the pump and the sample and excess pump power that is not absorbed in the active region, but is then absorbed in the DBR and substrate. The pump wavelength of 830nm generates carriers well above bandgap and these relax down to the lowest available states in the quantum wells. In the process the excess energy is lost mainly to phonons which cause local heating in the active region. About 30% of the pump power is not absorbed in the active region but is absorbed in the DBR and substrate, producing another heating effect.

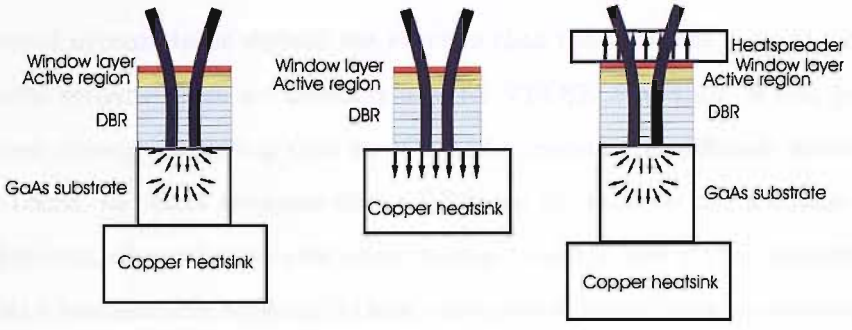

FIGURE 2.11: A schematic diagram showing an unprocessed sample, with the 3D heat flow in the high thermal impeadence substrate region, leading to strong thermal dependence of the sample, (left). A schematic of a sample which has had the substrate removed and is bonded directly to a copper heat sink, showing the improvement in heat flow away from the active region (centre). A schematic of a sample which has had a heatspreader bonded directly onto the front surface, showing that the heat is efficiently removed into the heat spreader in a 1D fashion (right).

Much research has been undertaken by other groups to attempt to solve the problem of heat removal to allow power scaling. There are two main approaches to dealing with this problem that have been demonstrated so far; substrate removal [4],[25],[8], or the use of a high thermal conductivity material as a heat spreader on top of the gain structure [53],[32].

Substrate removal works by removing the thick substrate with high thermal resistivity leaving a gain sample with a total thickness of only 20 microns, which can then be directly bonded using high thermal conductivity solders to a high thermal conductivity heat sink. This ensures that the heat is efficiently removed from the active region, reducing the local temperature of the active region for any incident pump power. To date 30W of CW output power has been achieved by using this method to manage the heat flow out of the active region [8]. This method for heat flow management and power scaling looks to be an extremely promising method for achieving high output powers.

A second method for heat flow management is the use of a heat spreader applied to the front surface of the gain structure. In this case heat spreader material is bonded to the front surface of the gain region using capillary bonding [53], to form an optical interface with low scattering loss. The high thermal conductivity of the heat spreader removes the heat from the active region efficiently and allows it to then be removed to a heat sink. This method has been demonstrated with diamond to produce 2.5W of output power, which was pump power limited [32].

This method appears to be slightly less effective than the substrate removal technique for material systems which are normally used for VECSELS at 1μm. It has, however, been shown through modelling that for VECSELs operating at different wavelengths, such as 1.5μm, the extra thickness of the DBR due to the lower Δn available in this material system, along with the even lower thermal conductivities of these materials, will mean that a heat spreader approach to heat management should have an advantage over substrate removal. The heatspreader approach to thermal management gives VECSELs the potential of achieving high output power at longer wavelengths, using more exotic material systems [30].

The final approach which has been demonstrated to overcome this problem is to use in-well pumping. This has been demonstrated particularly for VECSELs operating at 850nm, where pump lasers have a similar wavelength to the VECSEL output [33]. This in-well pumping means that there is very little mismatch between the absorbed photon energy and the emitted photon energy, meaning very little of the absorbed pump power is lost to heating through lattice vibrations caused as energetic carriers created relax to the lowest available energy states in the sample. This technique does, however, pose some problems and remove some of the advantages of these lasers over solid-state lasers. The major problem is that the absorption per pass is low due to there only being pump absorption in the quantum wells. This leads to the need to have a multi-pass pump scheme which is complicated and expensive.

Power scaling by using in well pumping is possibly the least appealing approach due to the removal of many of the advantages that VECSELs have over diode pumped solid state lasers. In-well pumping may however be a method to allow for short wavelength

VECSELs to be produced, where the pump diode lasers available have a similar wavelength as the lasers. Recently in well pumping has been shown to produce an optical to optical efficiency as great as 35%, and 1.9W output power, with the use of a pump resonating microcavity [29].

Chapter 3

Sample characterisation and CW lasing

3.1 Gain sample characterisation

Samples are designed with specific characteristics for particular purposes and when a new sample is grown the sample must be characterised to assess the quality and accuracy of the growth. This characterisation process involves measuring the following characteristics; the reflection spectrum, the edge-photoluminescence spectrum (edge PL), the integrated photoluminescence power measurements (integrated PL), the top surface photoluminescence spectrum (top PL) and CW lasing characteristics.

Here I will describe the characterisation process used to assess the quality of samples using experimental data measured from two different samples: QT1544 and QT1712. QT1544 is the VECSEL gain sample that has been used to produce all of the results in this work, and a full sample characterisation of this sample has previously been done by Hoogland [1]. Both QT1544 and QT1712 are based on the same basic design of the active region and the DBR, whcih is described in more detail in 2. They are based on a $7\lambda/2$ long active region, containing 6 quantum wells, positioned at the antinodes of the modulus of the E-field. QT1544 is designed for an operating wavelength of 1035nm, while QT1712 is designed for 1030nm. The DBRs are made of 27.5 layers of GaAs/AlAs

and are centered at their design wavelengths. The main difference between the two samples lie in the window layer on top of the active region. In the case of QT1544 it is designed to be $1.45 \times \lambda/4$ thickness, meaning that it is nearly half way between resonant and anti-resonant, being slightly more anti-resonant than resonant. QT1712 on the other hand has a window layer with thickness $3.25 \times \lambda$, which was chosen to be thick to act as an intra-cavity heatspreader. It is designed to be antiresonant at the design wavelength, being a complete multiple of $\lambda/4$ thickness.

The measured reflection curves allow the as grown sample characteristics to be compared to those that were designed, as the designed structure reflectivity is calculated theoretically using a transmission matrix method which is described in detail in [1]. This experimentally simple comparison gives information as to the quality of the DBR and the accuracy of the growth due to the position in wavelength of the stop band and peaks surrounding it. These measurements also give information on the quantum well absorption spectrum at room temperature and low pump power. This again allows a direct and fast comparison of the grown characteristics to those of the design.

A reflection curve for sample QT1544 is shown in Figure 3.1. It can be seen that there is good agreement over the stop band between the design and the measured reflectivity, although the modulations away from this show that there is some variation and inaccuracies in the thicknesses of the layers in the DBR. The peak of the absorption can also be seen to be located at approximately 1020nm which shows that the quantum wells are emitting at the desired wavelength at low excitation and room temperature. This shows that overall the growth appears to be high quality, with only a small variation in the layer thicknesses in the DBR. There is more disagreement between the theoretical reflectivity and the measured reflectivity away from the centre design wavelength, particularly on the short wavelength side of the stop band. This is mainly due to the formula which is used in the modelling program to predict the variation of the refractive index with wavelength. This formula gives good agreement with experimentally measured values from approximatly 900nm to 1150nm, whilst outside this range the predicted values do not agree with measured values so closly.

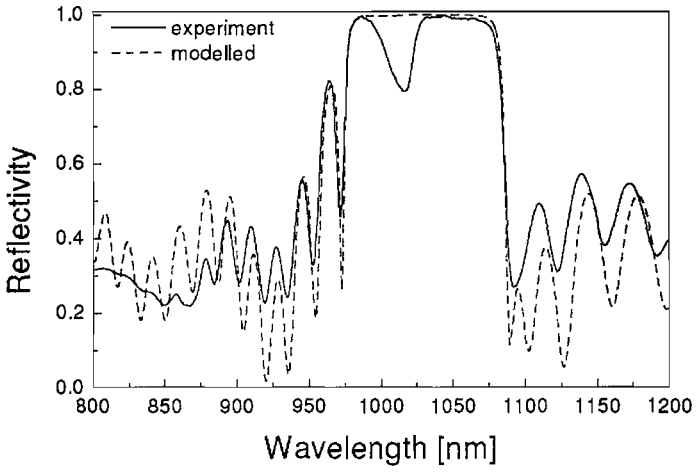

FIGURE 3.1: A graph showing the theoretical reflectivity from the sample design program, with no absorption from the quantum wells, and the measured reflectivity of the sample after growth. These show good agreement across the stop band, although there are some differences in the modulations, showing small variations in layer thicknesses.

The edge and top PL are measured using an experimental setup which is shown in Figure 3.2. The flip top mirror is used to select which measurement is to be taken. In the down position the edge PL is recorded and in the up position the top PL is measured. The gain sample is mounted on a copper heat sink using silver paint, which does not limit the device thermal performance, as the gain sample has a 500 μm thick GaAs substrate which is the limiting factor to heat removal as described in Ch.2. The copper heat sink is monted on a larger copper block which is temperature controlled using a peltier device. The temperature reffered to as the gain temperature is the temperature of the copper heat sink that the gain sample is mounted on. The 60 μm radius pump spot is focussed on the edge of the gain sample so that the edge PL measurements can be taken.

The edge PL reveals the intrinsic spectrum of emission directly from the quantum wells without any effects from the microcavity. It is obtained by pumping the sample next to a cleaved edge, and collecting the light emitted from the edge of the sample using a microscope objective. It is important to note that there is some PL which is guided along the active region and steps must be taken to ensure that a minimum of this light is collected as guided light shows modulations from the microcavity. This can be done by locating the microscope objective behind the plane of the gain sample, with an angle

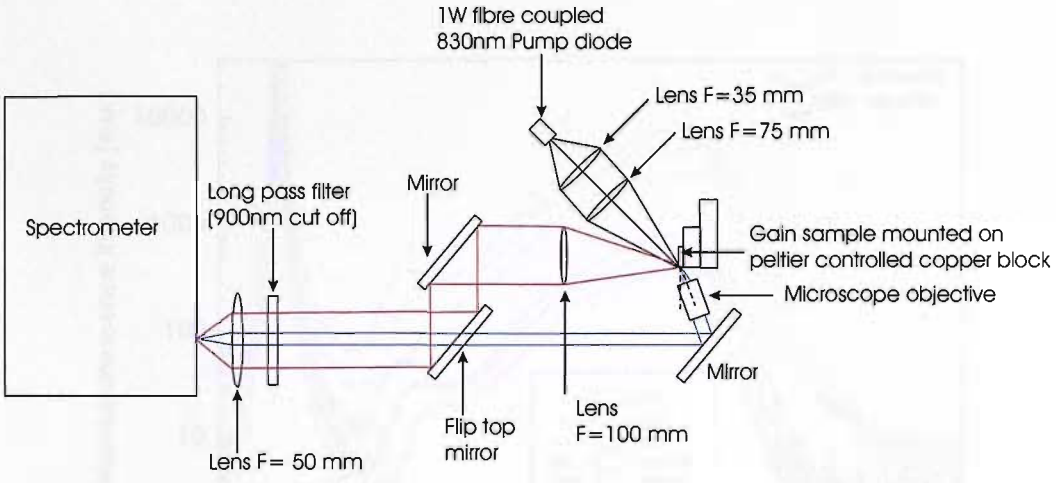

FIGURE 3.2: A diagram of the experimental setup for measuring edge and top PL. The flip mirror is flipped up to measure top PL and down to measure edge PL.

of approximatly 20^0 as shown in Figure 3.2. The microscope objective is also chosen to have a suitable numerical aperture and focal length to ensure that the PL that is guided by the microcavity is not collected. The microscope objective that we use has a magnification of 10 and a numerical aperture of 0.25. Finally experimentally it is important to check that there are no modulations on the edge PL spectrum that is recorded as these are evidence of collection of some PL which has been guided along the microcavity.

The edge PL measurements allow us to assess the quality of the quantum wells and their emission wavelengths at different pump powers. At this stage, based on the measurements of the reflectivity measurements and the edge PL spectrum, it is usually possible to estimate the laser performance of any particular growth.

From Figure 3.3 it can be seen that the peak of the PL spectrum shifts to longer wavelengths as the temperature is increased. It can also be seen that the peak of the PL decreases in amplitude as the temperature is increased. This shows that the gain falls as temperature increases. The pump laser light can be seen at 830nm in these measurements. The peak PL emission wavelength changes with temperature because the thickness of the quantum well changes. The total emitted PL also increases as the temperature is reduced because the excess heat is removed faster and the carriers are trapped faster in the wells. By measuring the edge PL at a range of temperatures and

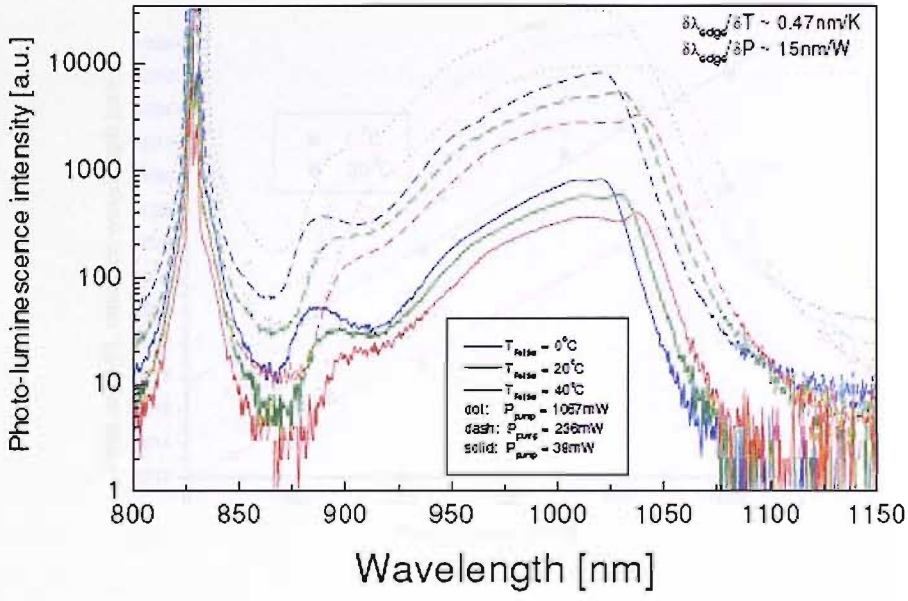

FIGURE 3.3: A graph showing the edge photoluminescence of the sample at a range of pump powers and at three different sample temperatures. It can be seen that the peak of the PL moves to longer wavelength due to increasing temperature, and also due to increasing pump power [1].

pump powers, the quality of the quantum wells can be inferred. For good quantum wells a shift in the peak PL wavelength with temperature of 0.3nm/K is observed. Performing these measurements at a range of temperatures allows us to compare the measured PL peak shift with temperature to that for a good quantum well.

As we also measure the edge PL at a range of pump powers this allows us to estimate the heating effect of the pump on the sample. By comparing this to the average shift expected, the thermal impedance of the sample can be assessed, as the local temperature at different pump powers can be seen. In this case it can be seen that a local temperature change of approximately 60^0C above heat sink temperature is induced for 1W incident pump power. The peak PL also moves to longer wavelengths with higher pump power due to the many body effect, leading to coulomb shielding of the exciton at higher carrier densities that are produced with higher incident pump powers.

Figure 3.5 shows the measured PL from the top surface of the sample. This measurement allows the combined effects of the PL emission from the quantum wells, and the

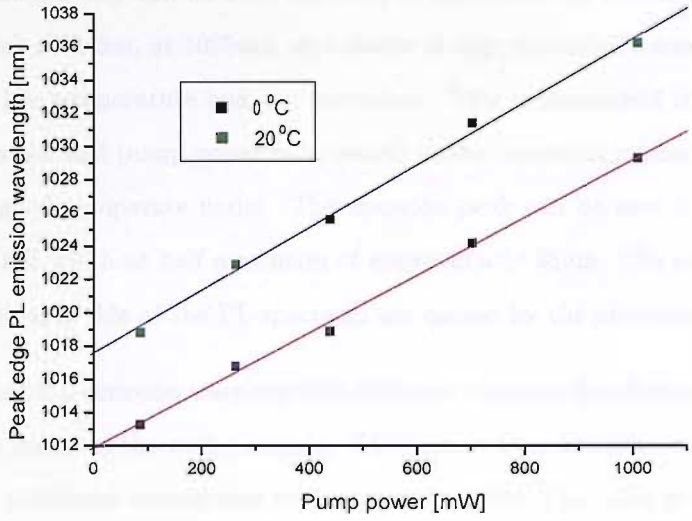

FIGURE 3.4: Graphs of the shift in peak PL emission with increasing pump power for two temperatures. This shows a shift in the peak Quantum Well gain of 0.3nm/K.

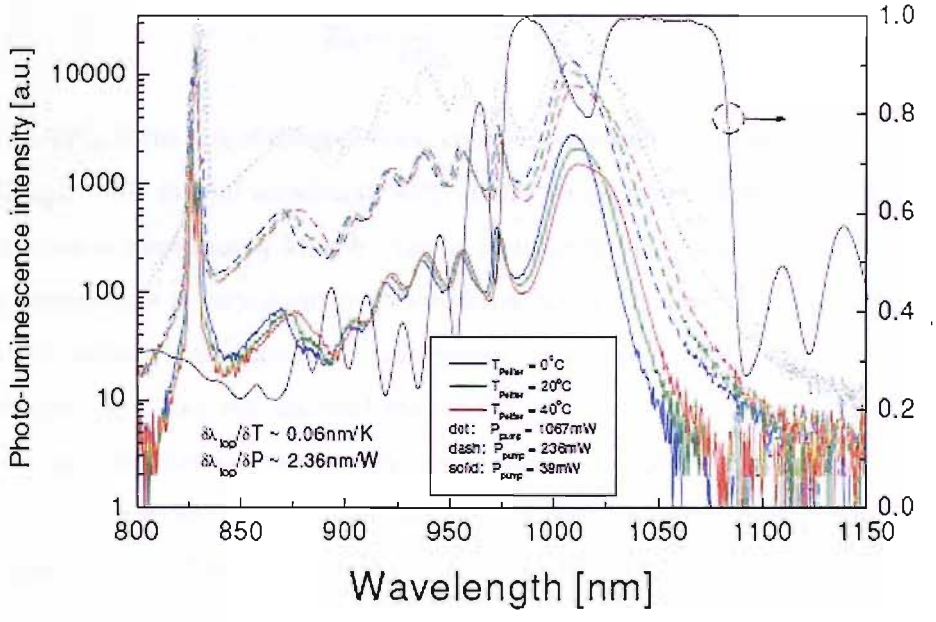

FIGURE 3.5: A graph showing the top photoluminescence of QT1544 at a range of pump powers and at two different sample temperatures. The top PL shows the microcavity enhancement ontop of the quantum well PL [1].

enhancement of the microcavity to be observed. The enhancement of the peak of the PL from the microcavity can be seen, centered at approximatly 1025nm. This has increased the peak emission, at 1025nm, by a factor of approximatly 10 compared to that at 1000nm at low temperature and low excitation. This enhancement reduces slightly as the temperature and pump power is increased to the operating regime that the gain sample is designed to operate under. The emission peak can be seen to be relatively broad, with a full width at half maximum of approximatly 35nm. The modulations on the short wavelength side of the PL spectrum are caused by the microcavity.

The shift in peak PL emission wavelength in this case is due to the changes in the thickness of all the layers in the entire sample. This means that the microcavity enhancement tunes at a different rate to that of the quantum wells. The value is approximately 0.1nm/K for samples designed at the early stages of VECSEL reasearch in this group, and in this case it is 0.06nm/K showing that the sample is slightly more immune to local temperature changes compared to earlier samples. The thermal resistance of the entire structure can also be obtained from these measurements using Eq.(3.1):

$$Z_{th} = \frac{\delta\lambda}{\delta P_{abs}} \frac{\delta T_{sample}}{\delta\lambda}, \tag{3.1}$$

where $\delta\lambda/\delta P_{abs}$ is the rate of change of peak emission wavelength vs. absorbed power and $\delta\lambda/\delta T_{sample}$ is the shift of wavelength with sample temperature. These measurements show a thermal resistance of 44K/W. This is a relatively high value, showing that the device temperature is very sensitive to the excess power absorbed, causing heating of the active region. This increase in temperature causes the quantum wells to become less efficient, providing less material gain and it also causes the peak quantum well emission and microcavtiy peak to tune away from each other, further reducing the device gain. This means that these samples are only suitable for low power experiments, up to approxiamtly 150mW, with high active region temperatures.

The quantum efficiency can also be measured and is important as these devices must be efficient as they are relatively low gain. There are two types of quantum efficiency that can be extracted from the measurement of the intensity of PL emitted normal to

the surface at a fixed distance. Here I estimate the overall device quantum efficiency. The quantum well quantum efficiency can also be extracted from these measurements but does not provide extra information about the overall device performance and is not described in detail in this work.

By integrating this measured value over the entire emission region, and taking into account the microcavity enhancement, it is possible to estimate the overall quantum efficiency of the sample. This value shows how well the pump photons are converted into emitted photons for the structure as a whole. Figure 3.6 shows the measured values of overall quantum efficiency for QT1712, which reaches a maximum efficiency of 0.18. The overall maximum efficiency is 18% for room temperature operation. As the temperature is reduced the quantum efficiency decreases as the quantum well gain is tuned away from the microcavity enhancement. The quantum efficiency is also reduced with increasing pump power, as the carrier density increases and therefore the Auger recombination rate increases at a faster rate compared to the radiative recombination rate.

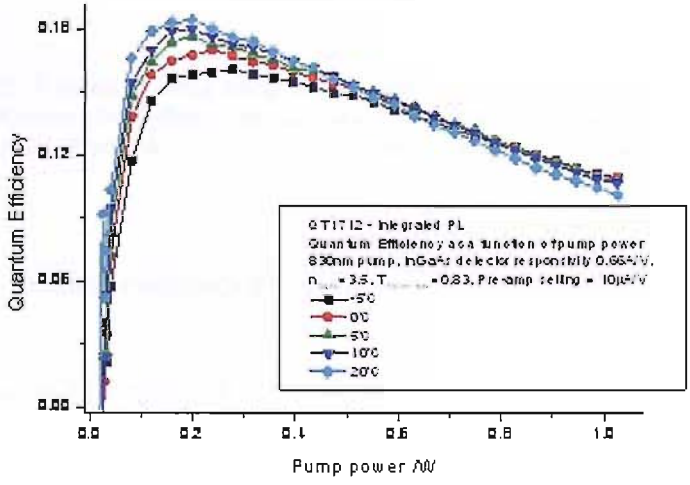

FIGURE 3.6: A graph showing the Quantum efficiency of the entire gain structure. It can be seen to reach a maximum value of approximatly 0.18, and can be seen to reduce as the temperature is decreased, as the peak wavelength of the quantum well emission and the microcavity enhancement tune at different rates with temperature.

The internal quantum efficiency, the quantum well quantum efficiency, can also be extracted from these measurements by removing the enhancement of the microcavity

through calculation. The internal quantum efficicency of the quantum wells has not been calculated in this work, but has been calculated by Hoogland [1] and is included here for completeness. These calculations reveal an estimate of the quantum efficiency of the quantum wells. The quantum efficiency of the quantum wells is seen to be high, in the order of 60% in Figure 3.7 [1]. The quantum efficiency of the quantum wells decreases as the temperature is increased as would be expected. A more complete discussion of quantum efficiency measurements in VECSELs can be found in [1].

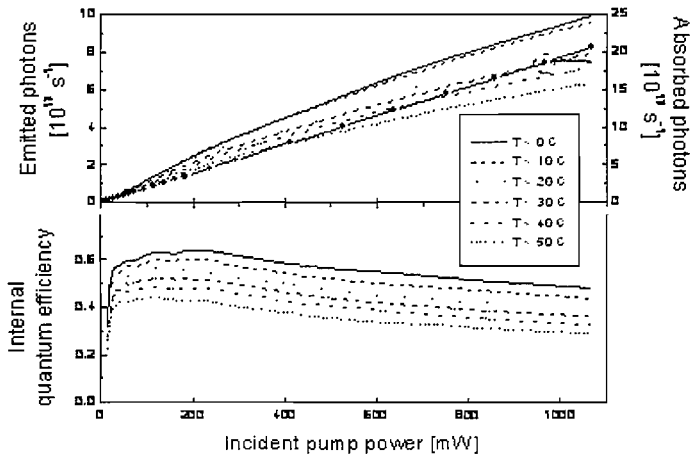

FIGURE 3.7: A graph showing integrated PL power measurements and the calculated quantum efficiency from this for sample QT1544. This shows that the quantum efficiency of the quantum wells reaches a maximum value of approximatly 60% [1].

3.2 CW lasing characterisation

The CW lasing characteristics of a sample are tested in a straight cavity and typical measurements are made, comparing the laser output power vs. pump power at a range of different temperatures as shown in Figure 3.8. This provides information on the threshold and slope efficiency of the laser. The maximum output power of the laser can also be measured in this way.

For an unprocessed sample similar to our current designs an output power of greater than 100 mW would indicate a good sample. Below i show CW laser results from sample QT1712, in a straight cavity with a 50 mm radius of curvature, 0.7% output coupler as

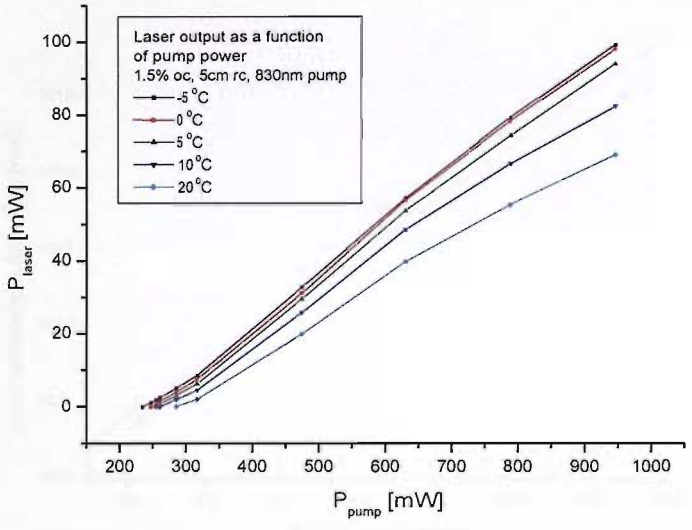

FIGURE 3.8: Laser output power curves for a range of gain temperatures for sample QT1712. This shows that the output power is pump power limited in this case, although it can be seen that the input-output curve is starting to roll over at room temperature. A CW output power of approximatly 100-150mW for 1W pump power is typical of a good sample, grown to our standard design, with no post growth processing.

one end mirror and the gain sample forming the other end of the cavity. The sample is pumped by a 1W fibre coupled 830 nm diode laser onto an area of radius 60 μm. The cavity length is then optimised to provide the highest output power, and lowest threshold.

Figure 3.9 and Figure 3.10 show how the laser wavelength tunes with pump power, and hence carrier density, as well as increasing temperature, and with heat sink temperature respectively. A typical shift of 0.1nm/K is seen, which is similar to those seen in the top PL spectra, as would be expected.

Recent measurements have shown that the thermal shift of the laser wavelength of the samples is vastly reduced for samples which have an Al0.2Ga0.8As/AlAs DBR, and hence no pump absorption in this region, as opposed to the AlAs/GaAs DBRs that are used in the samples investigated here. This should increase the total output power achievable as the lasers will be less prone to thermal rollover. However we currently do not have a good sample of this design as there is a growth mismatch between the quantum wells and the DBR for the samples we have with the improved DBR.

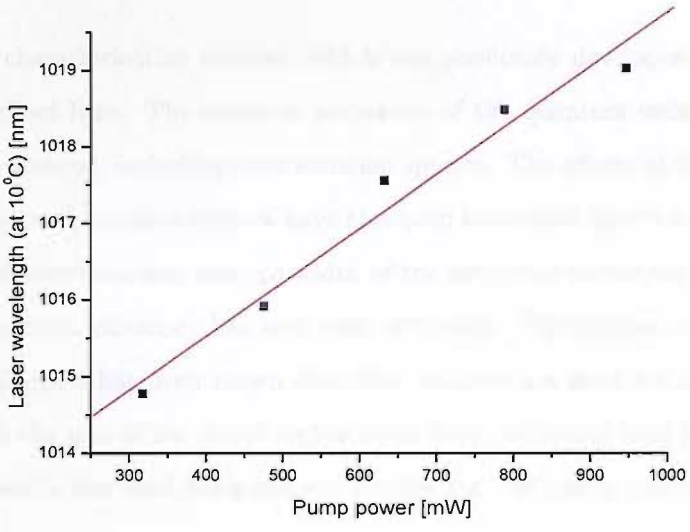

FIGURE 3.9: Graph showing the shift in laser wavelength with increasing pump power, with the sample heat-sink held at 10 degrees. The shift observed here is due to two effects; one being the local heating due to the pump light which is absorbed in the DBR and the other being the shift in wavelength due to many body effects.

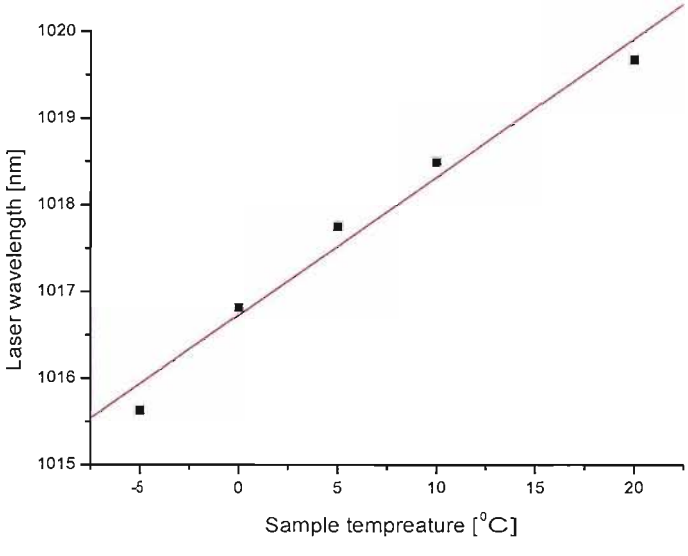

FIGURE 3.10: A graph showing the shift in laser wavelength with changing temperature of the gain sample heat-sink, for a constant pump power for QT1712. These show a shift of 0.16nm/K.

3.3 Conclusions

A full sample characterisation method, which was previously developed in our group, has been described here. The emission properties of the quantum wells has been experimentally measured, including their emission spectra. The effects of the microcavity on the quantum well emission spectra have also been measured, showing the amount of microcavity enhancement and also the width of the resonance in the top-PL spectrum. The overall quantum efficiency has also been estimated. The thermal impedance has been estimated and it has been shown that these samples are good for low power laser operation, with the gain of the active region being sensitive to any local heating effects, causing increases in the local temperature. Finally the CW lasing characteristics have been measured.

These measurements are experimentally relatively easy to obtain and are useful to assess and obtain an understanding of the basic properties of a gain sample before they are used for applications, such as mode-locking, where the explanation of experimental observations can be much more complex.

Chapter 4

Introduction to mode locked VECSELs: Theory of mode-locking and SESAMs

4.1 Introduction to mode-locking

There are several methods of mode-locking lasers that are used today depending on application. These fall in two basic groups; active mode-locking and passive mode-locking. Active mode-locking uses a modulator such as an accusto-optic modulator or an electro-optic modulator which is externally driven by an electrical pulse source.

This method of mode-locking requires the modulation of the active modulator to be carefully controlled to be at a whole multiple of the repetition frequency of the laser cavity to achieve a stable pulse train output. Active mode-locking is the type of mode-locking favoured by harmonically mode locked fibre lasers for applications such as telecommunications as this method gives control of which harmonic the laser is locked to [13]. Active mode-locking does, however, tend to produce longer pulses and requires significant control electronics to achieve stable mode-locking.

Passive mode-locking on the other hand uses an intensity dependant loss or gain. In the case of an intensity dependant loss, the loss is reduced as the intensity is increased.

In the case of intensity dependent gain, the gain is increased with increasing intensity. This means that it is energetically favourable for the laser to operate in a mode locked regime as this means that either the loss is minimised if a intensity dependent loss is used or the gain is maximised if an intensity dependant gain is used.

Passively mode locked lasers are relatively simple, with no external control electronics or drivers needed to produce stable mode-locking. Passively mode locked lasers can also produce the shortest pulses generated with mode locked lasers through the use of a optical nonlinearity. An example of a passively mode locked laser which use an intensity dependant gain is the mode locked Ti:Sapphire laser with a soft aperture. This uses the Kerr lens effect which produces better laser mode overlap with the gain profile in the gain crystal with high peak intensities than in CW operation [21]. SESAM mode locked lasers are another example of passively mode locked laser, but in this case a intensity dependant absorbtion is used. SESAMs are slow saturable absorbers, taking many times the pulse duration to recover to their high loss state [54].

Mode-locking of VECSELs has been demonstrated with both active mode-locking, producing long (100 ps) pulses [55] and passive mode-locking using a SESAM and have produced picosecond pulses [9], and even sub 500 fs pulses directly from the laser oscillator [40]. The theory of mode-locking has been explained in a great many texts, and an excellent source to describe the mechanism for soliton mode-locking with fast and slow saturable absorbers and the theory of mode-locking with a slow saturable absorber and gain saturation is given in [54] and [56]. In this chapter, I will give a short overview of mode-locking in general and mode locked VECSELs in particular.

4.2 Theory of mode-locking

Mode-locking of a laser can be described in two different ways; the frequency domain and the time domain. This discussion is based on that reported in [57].

In the time domain picture there is a saturable loss in the laser cavity and hence the net loss per round trip is less if the laser has a pulse with high peak power oscillating inside the laser cavity. When the laser starts up, the CW output has some noise associated

with it and one of these spikes oscillating in time bleaches the saturable loss slightly, and therefore achieves more gain per round trip compared to the surrounding signal.

Over many round trips this noise spike is amplified into a pulse and the intra-cavity photons are enhanced around this noise spike, reducing the number of photons spread over the rest of the cavity round trip time due to the preferential gain. The pulse is formed by the laser as this is the most efficient way for the laser to operate; in this regime the total losses of the cavity are lower than in the CW regime.

In the frequency domain description of mode-locking the laser oscillates on many longitudinal modes, and in a CW laser these have no fixed phase relationship to each other. This means that the laser output is constant when viewed on a relatively long time scale such as that given by a photodetector.

In reality, if the laser output is viewed on a short enough time scale it can be seen that the laser output consists of a random pattern of pulses and noise spikes. This output pattern is periodic and each pulse has a characteristic time, which has a duration $\Delta\tau_p$, which is approximately $1/\Delta\nu_l$, where $\Delta\nu_l$ is the total oscillating bandwidth of the laser.

On the other hand, if the phase of the longitudinal modes are locked to each other then the output changes from a random series of short noise spikes, to a definite pattern of pulses, in a pulse train. In the simplest mathematical description of mode-locking it is assumed that all of the oscillating longitudinal modes have equal amplitude, and are equally spaced in frequency as in Eq.(4.1). It is assumed that the laser oscillates on $2n+1$ modes.

$$\varphi_l - \varphi_{l-1} = \varphi \tag{4.1}$$

where φ_l is the phase of one of the output modes and φ_{l-1} is its adjacent mode. φ is a constant in this case.

The total electric field of the electromagnetic wave at any point can then be written as show in Eq.(4.2).

$$E(t) = \sum_{l} E_0 expj[(\omega_0 + l\Delta\omega)t + l\varphi] \tag{4.2}$$

In this equation ω_0 is the central mode, which is assumed to have a phase of zero. $\Delta\omega$ is the frequency difference between two longitudinal modes.

Eq.(4.2) can be expressed differently in terms of a sinusoidal carrier wave at the central mode frequency as shown in Eq.(4.3), with a time dependant amplitude shown in Eq.(4.4).

$$E(t) = A(t)exp(j\omega_0 t) \tag{4.3}$$

$$A(t) = \sum_{l} E_0 exp[jl(\Delta\omega t + \varphi)] \tag{4.4}$$

Eq.(4.4) can be re-written with a new time reference t' so that $\Delta\omega t + \varphi = \Delta\omega t'$ as shown in Eq.(4.5).

$$A(t') = \sum_{l} E_0 expjl(\Delta\omega t') \tag{4.5}$$

The sum in Eq.(4.5) is a geometric progression and can be summed to give Eq.(4.6).

$$A(t') = E_0 \frac{sin[(2n+1)\Delta\omega t'/2]}{sin(\Delta\omega t'/2)} \tag{4.6}$$

From Eq.(4.6) it can be seen that pulse maxima occur when the denominator vanishes. This occurs at $t' = 0$. Following pulses occur at time intervals such that $\Delta\omega t' = \pi$. This means that two successive pulses are spaced as shown in Eq.(4.7).

$$\tau_p = \frac{2\pi}{\Delta\omega} = \frac{1}{\Delta\nu} \tag{4.7}$$

The duration of the pulses can also be predicted from the theory of mode-locking given above and is given by Eq.(4.8).

$$\Delta\tau_p \cong \frac{2\pi}{(2n+1)\Delta\omega} = \frac{1}{\Delta\nu_L} \tag{4.8}$$

The above description of mode-locking assumes equal amplitudes of the different oscillating modes and also assumes no chirp, leading to transform limited pulses. In reality however it is common for the pulses that are produced to display a more complex behaviour that that described above, although this can be taken into account.

It can therefore be seen that the phase shifts introduced by each component in the laser cavity must be carefully analysed and taken into account to understand the mode-locking process.

The magnitude and origin for differing phase shifts in the mode locked VECSELs has been calculated and is reported in [1] and can be shown to account for the overall process of the mode-locking of a VECSEL by a SESAM.

4.3 Fast and slow absorber passive mode-locking

The work done in this thesis and indeed at Southampton University on mode-locking VECSELs has been based on passive mode-locking using SESAMs. These are slow saturable absorbers, with a recovery time much longer than the duration of the formed pulse. Slow saturable absorber mode-locking in a VECSEL relies on gain saturation as well as SESAM saturation to open a short window of net gain in the laser cavity round trip time. In this regime it is critical that the SESAM saturates faster than the gain, as it is the small window in time between the saturable loss saturating and the gain saturation that leads to a small window of net gain for the pulse, and hence the stable pulse being formed. A diagram showing mode-locking with a slow saturable absorber and gain saturation and a fast saturable absorber with no gain saturation for comparison can be seen in Figure 4.1 [56].

Mode locked VECSELs can be observed to produce soliton pulse output shapes and this has been explained with a quasi soliton pulse shaping mechanisms relying on weaker effects to shape the pulse than are seen in typical soliton mode locked lasers[41]. VECSEL lasers also rely on gain saturation as well as SESAM saturation to produce the pulse.

Mode locked lasers producing the shortest available pulses are typically mode locked using a fast saturable absorber effect. In the case of a hard apertured Ti:Sapphire laser this is created by a hard aperture introducing loss in the CW regime, This loss is saturated when the laser works in a mode locked regime as the kerr lens, which is intensity dependant, reduces the laser mode size at the hard aperture. In a fast saturable absorber the saturation and recovery of the loss follows the pulse shape exactly. This produces strong pulse shaping in terms of pulse duration, although it is important to ensure that the modulation depth of the saturable loss is great enough. A diagram of a fast saturable absorber and slow saturable absorber is shown in Figure 4.1 [56].

It has been attempted to mode lock a VECSEL using a Kerr lens in ZnSe, although to date this has proved unsuccessful, mainly due to the available gain not being great enough to compensate for the introduction of the ZnSe crystal intra-cavity with the samples we have available. It has been suggested that a polymer based microstructured fast saturable absorber could be used to mode lock a VECSEL, and a design has been suggested, although this has not been experimentally attempted [58].

The insertion of a Semiconductor Saturable Absorber Mirror (SESAM) into the laser cavity introduces a saturable loss to the laser. The SESAMs that are used in VECSELS have to have very low non-saturable losses of less than 1.4%, and the saturable losses are typically approximately 1% or less.

All of the mode locked VECSELs demonstrated so far use a slow saturable absorber, with the exception of the femtosecond soliton mode locked VECSEL which uses a combination of the fast ac Stark effect and the slow saturable absorber effect, which is normally exploited for mode-locking.

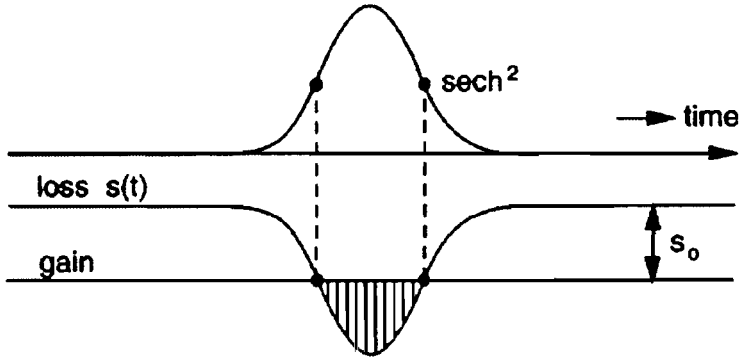

(a) Schematic diagram of a fast saturable absorber mode locked laser

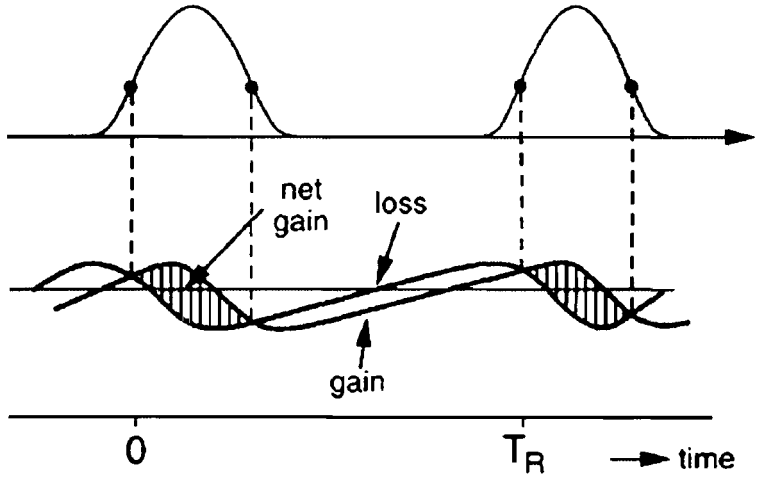

(b) Schematic of a slow saturable absorber mode locked laser

FIGURE 4.1: A schematic diagram showing fast saturable absorber mode-locking and slow saturable absorber mode-locking. A mode locked VECSEL mode locked with a SESAM uses slow saturable absorber mode-locking, and gain saturation is important to open a short window of net gain in time. In the case where the VECSEL produces sub 500 fs pulses, the ac-stark effect is utilised, which is a fast saturable absorber effect. (after [56])

4.4 Haus model of mode-locking

Another approch to the discription of mode-locking is the Haus theory of mode-locking [56]. Haus has developed models for many types of mode-locking, including slow saturable absorber mode-locking, which is most similar to the mode-locking mechanism in VECSELs. It is useful to look at this description because, whilst it is not a complete description of the mode-locking process in a VECSEL, and therefore cannot be used for quantative predictions, it does give a qualitative insight into the relative importance of several factors. In particular we will use it here to demonstrate the importance of the gain bandwidth curvature in the formation of short pulses. This has a direct implication on gain sample design, as the gain bandwidth curvature can be controlled by controlling the microcavity enhancement in the gain smaple.

In the model of mode-locking with a slow saturable absorber the effect of gain saturation and recovery become important. When the dynamics of the gain and saturable absorber are taken into account the master equation for mode-locking, given in Eq.(4.9) becomes:

$$\frac{1}{T_R}\frac{\partial}{\partial T}a = [g_i exp(-\int_0^t dt\,|a|^2/W_g) - \ell - s_i exp(\int_0^t dt\,|a|^2/W_s)]a + (\frac{1}{\Omega_f})^2\frac{\partial^2}{\partial t^2}a. \quad (4.9)$$

Here T_R is the roundtrip time, g_i is the initial gain before the pulse arrives, s_i is the initial loss of the absorber before the pulse arrives, W_g is the saturation energy of the gain and W_s is the saturation energy of the saturable absorber, ℓ is the background loss and a is the amplitude of the envelope of the pulse. Finally Ω_f is a filter function which is used to express the filtering action of the gain bandwidth. In the case of mode-locking with a slow saturable absorber it is useful to express this filter function as a separate fixed filter function, rather than by the finite bandwidth of the gain, which varies with time as the gain is saturated and recovers.

From Eq.(4.9) a solution of the form $a(t) = A_0 sech(t/\tau)$ can be found, with one of the constraints being that:

$$\frac{1}{\tau^4} = \frac{\Omega_f^2 A_0^4}{4}\left(\frac{s_i}{W_s^2} - \frac{g_i}{W_g^2}\right). \tag{4.10}$$

Eq.(4.10) is the equation for the inverse pulsewidth and from this several intersting points can be seen. The first is that the pulsewidth has a dependance on Ω_f, the filter function which represents the gain bandwidth. Therefore it can be seen that ensuring that the curvature of the gain is as flat as possible produces the shortest pulse duration. For VECSELs, this means that for efficient mode locked operation, with the shortest possible pulses being produced, the gain sample should be designed to have a near anti-resonant microcavity as discussed in Ch.2, as the effect of the curvature of the filter function of the gain counteracts the curvature of the emission from the quantum wells to some extent, creating a broader gain bandwidth, and hence potentially shorter pulses.

Another important practical conclusion that can be obtained from Eq.(4.10) is that to obtain a real solution $S_i/W_s > g_i/W_g$, meaning that the saturable absorber must saturate faster than the gain in order for a net window of gain to be opened. This condition is experimentally achieved in the work reported here by ensuring that the laser mode area is smaller on the SESAM than on the gain structure. An area ratio of 25 is typically used to ensure that the absorber saturates significantly faster than the gain.

4.5 Semiconductor Saturable Absorber Mirror design parameters and production methods

There are several types of SESAMs that can be used for mode-locking VECSELs. The typical method used for making a SESAM is to grow a structure similar to the gain structure, but instead of having multiple quantum wells in the active region, typically only one is used.

There are four parameters that are important for the design of a SESAM to produce stable short pulse mode-locking. The first and simplest is non-saturable losses. These are intrinsic losses which should be minimised for optimal device performance. The

second is the modulation depth of the SESAM, ΔR%, i.e. how much the reflectivity changes between unsaturated and saturated. Thirdly the recovery time of the SESAM is important, with a faster recovery time typically producing shorter output pulses from the laser. Lastly the saturation fluence, $F_{sat,sa}$, is important as this determines how easily the saturable loss is saturated. The lower $F_{sat,sa}$, the faster the mode-locking onset, for a given mode area and incident energy on the SESAM. A ratio called the saturation perameter can be defined, which is given by the ratio of the fluence of the incident pulse on the SESAM and the saturation fluence of the SESAM and is shown in Eq.(4.11):

$$S_a = \frac{F_{pulse}}{F_{sat,sa}} \tag{4.11}$$

The saturation fluence of the SESAMs described here is of the same order of magnitude as that of the gain structures as they are both based on quantum wells. However, the micro cavity can also be designed to change the intensity on the quantum well, and hence how easily it saturates. If the saturation fluence is too high, the loss is hard to saturate and hence the pulse shaping takes a long time or does not happen at all.

SESAMs are normally designed to operate so that the pulse saturates them many times over, ensuring that they saturate faster than the gain saturates, opening a short window of net gain per round trip for the pulse to form in. It is therefore necessary to have a smaller mode waist on the SESAM than on the gain to ensure that the pulse saturates the SESAM quicker than the gain. The only exception to this is to use a saturable absorber with a different saturation fluence. This has been achieved by using a quantum dot SESAM and has allowed lasers with repetition rates of up to 30 GHz to be produced [42] using a 1:1 ratio of spot size on the SESAM and the gain region. In the case of a VECSEL producing 500fs pulses at a repetition rate of 1.2 GHz and an average output power of 40 mW, the saturation parameter on the SESAM would normally be in the range of $S_a = 27$.

The modulation depth, ΔR%, of the SESAM is controlled in exactly the same fashion as the gain of the gain samples. ΔR% is set by a combination of the total saturable

absorption due to the number of quantum wells and the microcavity enhancement factor which controls the strength of the coupling of the photons to the quantum well. A large ΔR introduces too much loss into the cavity, whilst a weak ΔR produces too weak a pulse shaping effect.

As mentioned above it is also important for the SESAM to have a fast recovery time. For example with VECSELs the typical recovery time of SESAMs used to mode lock is between 5 ps and 150 ps. For a good quantum well the upper level lifetime is of the order of a nanosecond. For good mode-locking to be achieved, a recovery time as short as possible is desired. Therefore it is not possible to use ordinary quantum wells, grown under ideal conditions, as these have a carrier lifetime similar to the gain carrier lifetime. The recovery time of a quantum well in a SESAM can be made fast through several techniques which are outlined below.

The first and probably most common technique is to grow the quantum well at low temperature, typically in a MBE reactor. The low temperature growth of the quantum well ensures that it has many defects, which whilst introducing a fixed loss, also introduces sites for fast recombination of the excited carriers in the quantum well. The recovery time of a SESAM can be made very short, but there is a basic rule that as the recovery time gets shorter the non saturable losses also get bigger, meaning that there is a design limit for the shortest recovery time usable for VECSEL lasers due to the low overall gain. The saturable absorbers that we use that have been grown in this way have a recovery time of 5 ps and 150 ps with fixed losses of typically 1.4% and saturable losses also of 1%.

There has been work done in our group on the use of superlattices to reduce the recovery time of a saturable absorber whilst keeping the non-saturable losses small, and from that the superlattice saturable absorber mirror (SUSAM) has been demonstrated. Typical recovery times of 50 ps have been achieved with this process. These SUSAMs have a saturable loss of approximately 0.7% and a low non-saturable loss of 0.2% or less due to the growth under ideal conditions [59]. A SUSAM mode locked VECSEL has been demonstrated to produce picosecond pulses, although it has extremely hard to

produce clean Gaussian or $sech^2$ pulse profiles and the output pulses typically have a large pedestal component.

The final method of making a SESAM have a fast recovery time that has been developed in our research group by Hoogland and Garnache is to grow the quantum well extremely near the top surface of the sample at normal growth temperatures [60]. We typically grow it at a depth of 2 nm from the surface. This causes surface recombination effects to speed up the recovery process of the saturable absorber because the top layer of the semiconductor has free bonds that localise charge, aiding recombination at the surface. We have measured one of the SESAMs that we use grown by this process to have a recovery time of 21 ps using a streak camera [60]. A schematic diagram of a surface quantum well SESAM is shown in Figure 4.2.

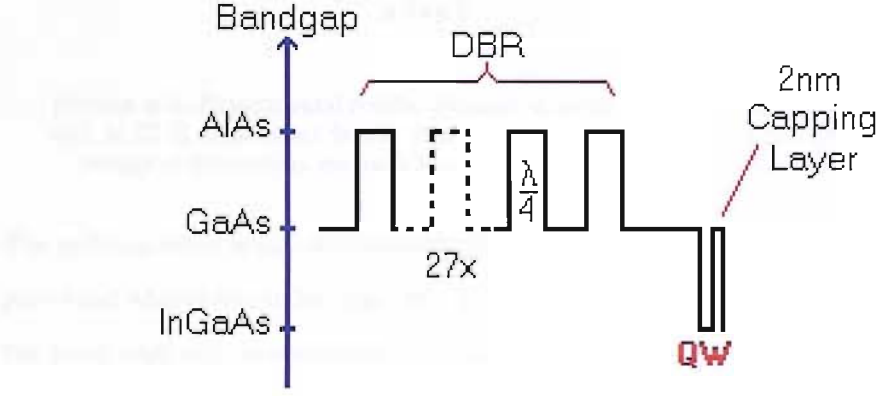

FIGURE 4.2: A schematic diagram showing the design of the surface quantum well SESAM, QT1627, with the quantum well positioned 2 nm from the top surface.

This SESAM has also been designed so that the band edge of the quantum well is at 1040nm so that the ac-Stark effect can be utilised with careful optimisation. This leads to the SESAM having an extremely fast component to its recovery time, which is thought to be instantaneous.

The ac-Stark effect is an instantaneous band edge shift which is seen when the quantum well is optically pumped below the band edge. It is due to a shift in the exciton level due to the instantaneous electric field incident on it. This band-edge shift is fast and the recovery is thought to be instantaneous.

The band edge shift is shown in Figure 4.3 for a quantum well at 27 K so that the effect can clearly be resolved [61].

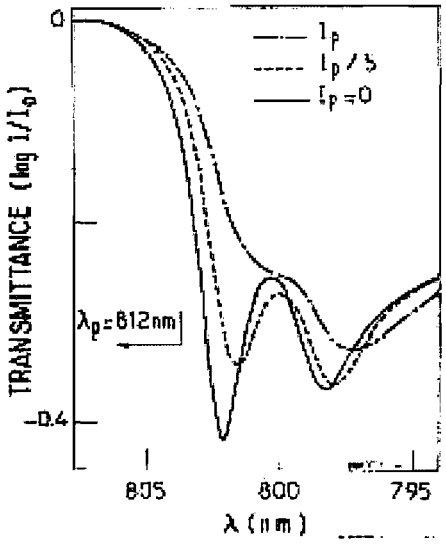

FIGURE 4.3: Experimental results obtained showing the ac-Stark shift for a Quantum well at 27 K. This effect is still present at room temperature, although the thermal energy of the carriers makes it harder to measure. Ip = 10^10 W/cm^2 (after [61])

The ac-Stark effect is usually investigated at low temperature in quantum wells, where a pure band edge shift can be observed. As the temperature and pump power is increased the band edge shift is accompanied by a reduction in the exciton level due to the real carriers created. At room temperature, the band edge shift should be of the same order of magnitude, although the effect cannot be resolved due to the thermal distribution of the carriers at the higher temperature.

Chapter 5

Mode locked VECSELs: results and multiple pulse operation

5.1 Introduction

In this chapter I will report the results of the characterisation of the surface quantum well SESAM, sample QT1627, which has been used throughout the results reported in this work. This characterisation was performed by Rachel Grange at ETH Zurich.

I will then report the two distinct regimes in which a VECSEL consisting of gain sample QT1544 and SESAM QT1627 can operate; picosecond pulse production and sub 500 fs pulse production. I will show data for the full set of parameters measured, which make up a full characterisation of the pulses produced by a mode locked VECSEL. These include the optical spectrum detected using a spectrometer, the pulse autocorrelation detected using a Femtochrome FR-103XL autocorrelator, the RF spectrum of the first RF peak and the first 8 RF peaks detected using a Newfocus 25 GHz InGaAs photodiode and an Advantest R3273 26 GHz RF spectrum analyser and data from a 25 GHz fast sampling oscilloscope looking directly at the pulse train from the laser.

After this I will report new results from my work on satellite pulses, which are due to substrate reflections, and also report the first observation of multiple pulse operation of a sub 500 fs mode locked VECSEL along with an explanation for this.

5.2 Characterisation of the fast surface recombination SESAM

The SESAM parameters such as the saturable loss, ΔR, the non-saturable loss, ΔR_{ns}, the absorber recovery time, τ_{sa}, and the saturation fluence, $F_{sat,a}$, are critically important for the understanding of mode-locking dynamics and to predict the pulse duration and other characteristics of a mode locked VECSEL. To obtain experimetal values for all of these parameters two different experiments need to be performed. These experiments were carried out at ETH Zurich as they have an excellent SESAM characterisation facility, with stable mode locked lasers at 1030nm.

The first experiment is the nonlinear reflectivity measurement, where the reflectivity of the SESAM is measured across a range of incident pulse fluences. Details of the principle of this measurement can be found in [62]. In this case the reflectivity was measured over a range of pulse fluences from 9 to 2900 $\mu J/cm^2$ and the results are shown in Figure 5.1.

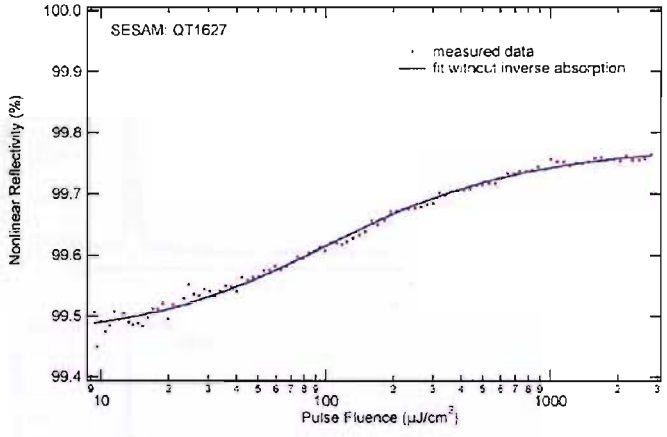

FIGURE 5.1: A graph showing the variation in reflectivity verses the incident pulse fluence. From these measurements the modulation depth, ΔR, the non-saturable losses, ΔR_{ns}, and the saturation fluence, F_{sat}, can be extracted.

From the fit made to the experimental results the saturation fluence, $F_{sat,a}$, non-saturable losses, ΔR_{ns}, and saturable loss, ΔR, can be extracted. From this experiment they are measured to be:

- $F_{sat,a} = 56 \pm 3 \mu J/cm^2$
- $\Delta R = 0.32 \pm 0.04\%$

- $\Delta R_{ns} = 0.22 \pm 0.04\%$

The second experiment is a pump-probe experment, which allows the absorber recovery time, τ_{sa}, to be measured. A typical pump-probe setup is used and the reflectivity is measured versus varying delay between the pump pulse and probe pulse. This allows the recovery time of the SESAM to be measured. In this experiment the source laser was a Yb:YAG solid-state laser mode locked with a SESAM, producing pulses with a repetition rate of 77 MHz, a pulse duration of 2.1ps and an average output power of 215 mW, centred at a wavelength of 1030 nm. The SESAM recovery time was characterised at a range of incident pump pulse fluences, from 8 to 422 $\mu J/cm^2$. Figure 5.2 shows the recovery time from -40 to +400 ps delay. This data shows that the SESAM can be characterised by a single recovery time, and does not have a slow component to the recovery.

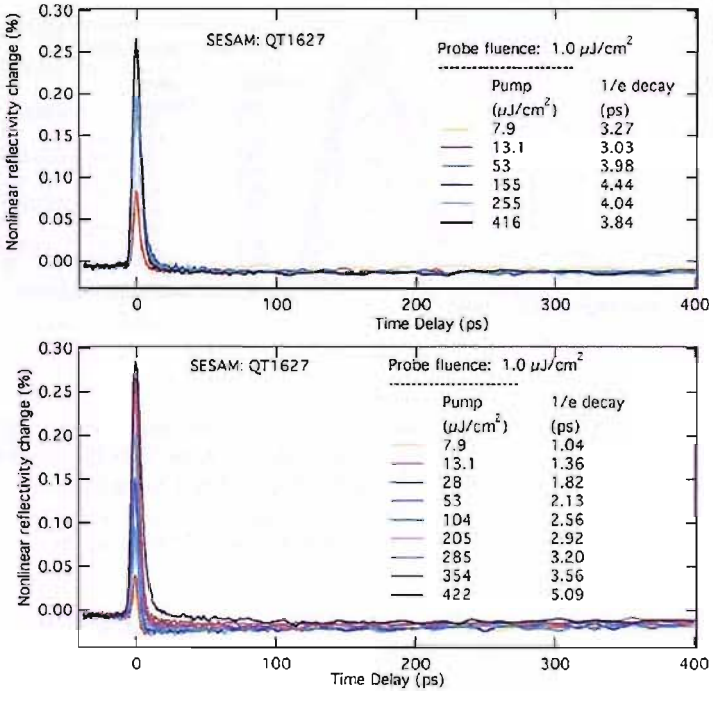

FIGURE 5.2: A graph showing the pump-probe measurements of the absorber recovery time of SESAM QT1627 at a wavelength of 1030 nm, at two different spots, for a range of incident pulse fluences up to 420 $\mu J/cm^2$.

Figure 5.3 shows the recovery time over a much smaller range of delays form -20 to +20 ps. In this case it can be seen that the decay time is relatively constant, independently

of the pump pulse fluence. It is thought that the SESAM recovery time should remain nearly constant up to pulse fluences of greater than 1500 $\mu J/cm^2$, as the nonlinear reflectivity measurements do not show any sign of inverse absorption like two photon absorption, even at high pulse fluences of 2900 $\mu J/cm^2$. It is also important to note that the pump-probe data looks nearly symmetric, showing that the recovery time is probably not being fully resolved, due to the pulse duration of the test laser available.

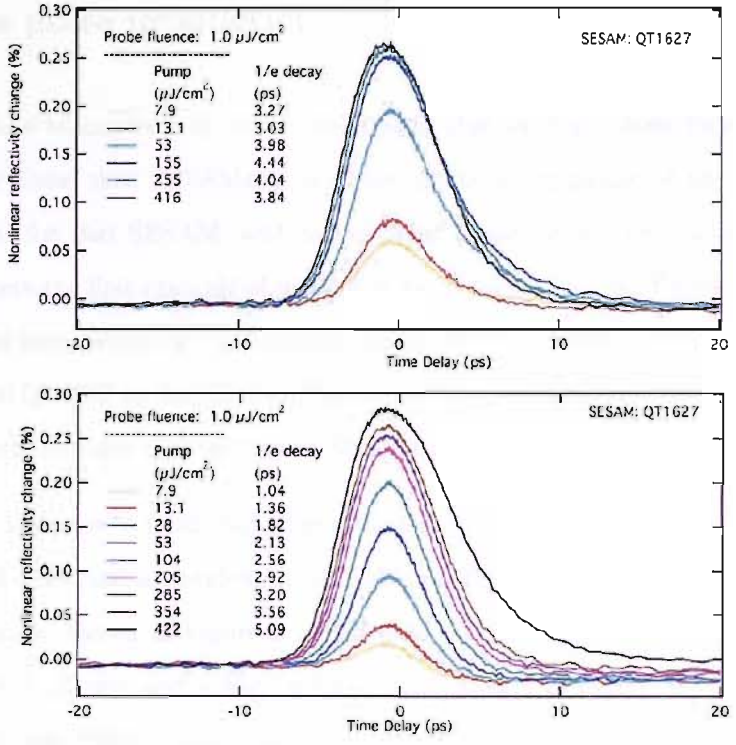

FIGURE 5.3: A graph showing the pump-probe measurements of the absorber recovery time of SESAM QT1627 at a wavelength of 1030 nm, at two different locations on the sample, for a range of incident pulse fluences up to 420 μJcm^2. In this graph the nonlinear reflectivity is plotted agains time, with a small time delay range, showing that the SESAM recoveres fully in a few 10s of picoseconds.

These measurements make it a simpler process to understand the dynamics of the mode locked VECSEL, although there are some limitations to these measurements. The main limitation is that the source laser was centered at 1030 nm. It would be extremely interesting to know the SESAM properties at the longer wavelength of 1040 nm to 1043 nm, which is the spectral region in which the sub-500 fs pulses are produced. At 1030 nm the test laser has a wavelength which is higher energy than the quantum well bandgap

and hence the laser wavelength is resonant with the SESAM quantum well absorption. At the longer wavelength we believe that the ac-Stark effect plays a part to the SESAM recovery time, and it would be useful to be able to compare the difference in the SESAM properties in these two different excitation regimes.

5.3 Mode-locking VECSELs with a slow saturable absorber - ps pulse production

VECSELs have been passively mode locked using slow saturable absorbers. The pulses produced by these slow SESAMs in the laser cavity are typically of the order of the recovery time for that SESAM, with pulses being formed from about 4 ps in duration up. These were the first example of mode-locking of a VECSEL [9]. Figure 5.4 shows all the measured parameters for a picosecond pulsed VECSEL based on QT1544 as the gain structure and QT1627 as the SESAM. Stable, clean picosecond pulses had not previously been observed with this combination of SESAM and gain strucure.

In this case the laser is producing approximately 40mW output power at a repetition rate of 939.6 MHz and a wavelength of 1046 nm. The laser consisted of a standard Z cavity design, as shown in Figure 2.1, and used a 0.7% output coupler with a radius of curvature of 50 mm and a high reflector with a 25 mm radius of curvature. The cavity length was slightly longer than that used in previous work, which usually used a repetition rate of approximatly 1.2 GHz. This causes the peak power of the intracavity pulse to be greater, leading to stronger saturation effects. The mode size on the gain was 60 μm radius, and the waist on the SESAM was 9 μm radius. This gives an area ratio of 44 between the gain and the SESAM. This is a significantly larger area ratio than than necessary to produce 500 fs pulses, which is of the order of 25. This increased area ratio, through a smaller mode area on the SESAM, means that the SESAM is saturated faster, and nonlinear effects such as self phase modulation (SPM) induced in the SESAM become greater.

The data in Figure 5.4 shows some very typical characteristics for picosecond pulses produced by a mode locked VECSEL. The first of these is the fact that it is several times

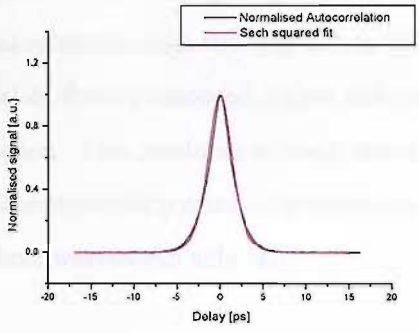

(a) Autocorrelation and sech squared fit of 2.13 ps pulse.

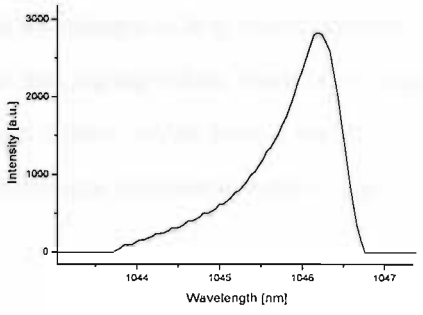

(b) Optical spectrum of 2.13 ps pulse.

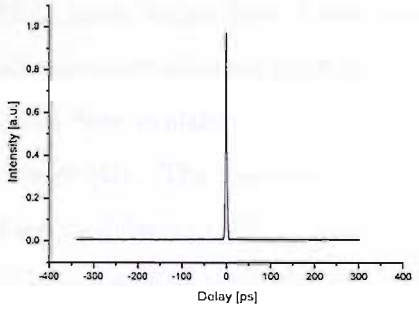

(c) Full range autocorrelation showing a clean single pulse with no sattelite pulses.

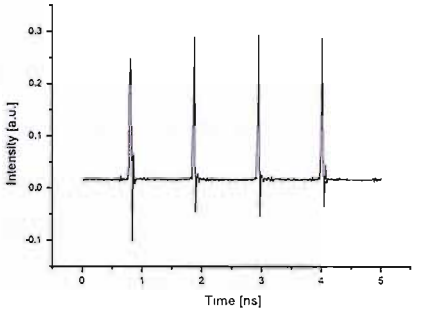

(d) Fast sampling socilloscope data of the pulse train, showing a single pulse per round trip.

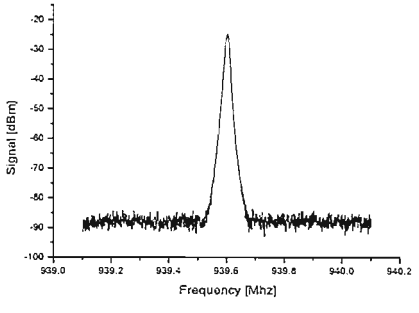

(e) First RF peak of the laser, showing a fundamental repetition frequency of 939.6 MHz.

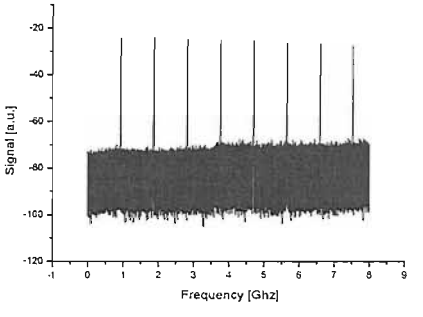

(f) Graph of the first 8 RF peaks of the mode locked laser. These show nearly equal amplitudes of all of the harmonics of the fundamental repetition frequency.

FIGURE 5.4: A complete characterisation dataset for a mode locked VECSEL producing 2.13 ps pulses at a repetition rate of 939.6 MHz, with an average output power of 40 mW.

Fourier limited, showing that there is a significant chirp to the pulses. The asymmetric optical spectrum with the long tail on the short wavelength side of the maximum is also typical of these picosecond pulses and occur in the regime where there is net negative dispersion. This produces strongly down chirped pulses, which have a nonlinear chirp. This nonlinear chirp causes the spectrum to be strongly assymetric with a longer tail on the short wavelength side [41].

5.4 Quasi-soliton mode-locking VECSELs producing sub 500 fs pulses

VECSELs mode locked with a combination of the fast ac-Stark effect and the slow saturable absorber effect are typified by sub 500 fs pulses with a $sech^2$ profile. The $sech^2$ profile has been explained in theory with the laser described as a quasi-soliton mode locked laser [41]. The mode-locking is established mainly due to the balance of the self phase modulation (SPM), induced in the SESAM, and the group delay dispersion (GDD) from the SESAM and the gain. It is a balance in these two effects that causes the steady formation of a quasi-soliton with less than 500 fs duration. The slow saturable absorber effect that is also partially exploited in the SESAM acts to stabilise the soliton against the continuum. Figure 5.5 shows a complete measurement set for a typical sub 500fs pulse VECSEL with an output power of 40 mW.

The SESAM and VECSEL gain sample are therfore designed with attention being paid to the GDD of the samples. The SESAM is designed so that at the operating wavelength of 1040 nm the GDD is small and negative. It is in the range of -50 fs^2 to -200 fs^2. On the other hand the VECSEL gain is designed to give a GDD of +500 fs^2 at the operating wavelength. The gain is in a double pass configuration in the laser cavity and therefore the net GDD per round trip is positive and small. It has been shown that in this regime quasi-soliton pulse formation can occur as the positive GDD is compensated for by the SPM induced in the SESAM, leading to a $sech^2$ pulse profile. On the other hand if the total GDD per round trip is negative, then strongly chirped pulses are produced, similar to those shown above [41].

In the example shown in Figure 5.5 the laser cavity was based on the standard Z design with an output coupler of 0.7% with radius of curvature 50 mm, and a high reflector with radius of curvature of 38 mm. The mode size on the gain has a radius of 60 μm and the mode radius on the SESAM is 12 μm, giving an area ratio of 25. The repetition rate was 905 MHz and the pulse duration was 448fs, at a wavelength centred at 1038.5 nm. These pulses of duration 448 fs represent the shortest pulses obtained from a mode locked VECSEL, with previous work reporting pulses as short as 471 fs. In this example the pulses are 1.01 times Fourier limited.

In the sub 500 fs pulse regime, the laser produces clean soliton-like pulses which are near bandwidth limited, and hence have little or no chirp. The pulse duration is sensitive to many parameters including gain temperature, which controls intra-cavity power, dispersion and gain characteristics, pump power and the mode-areas on the gain and SESAM.

5.5 Observations of satellite pulses due to substrate reflections

Small satellite pulses can sometimes be observed around the central pulse in the autocorrelation, under certain operating conditions. Satellite pulses are typified by their small relative amplitude and fixed spacing compared to the main pulse. An example of an autocorrelation of the pulse train of a typical 500fs pulsed VECSEL is shown in Figure 5.6. The satellites can clearly be seen and have a spacing of 15 ps. Satellite pulses are experimetally observed in the autocorrelation in the normal course of pulse characteriation.

This effect was first observed by S.Hoogland [1] and has been explained due to the reflections off the back surface of the substrate of the gain region coupling back into the cavity. This leads to pulses of much smaller amplitude, due to the much higher losses and also explains the fixed spacing between the main pulse and these satellites. The typical delay of 15 ps relates to a distance in GaAs of 1mm, twice the substrate thickness.

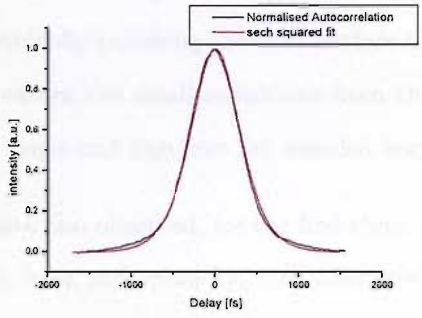

(a) Autocorrelation and sech squared fit of 448 fs pulse.

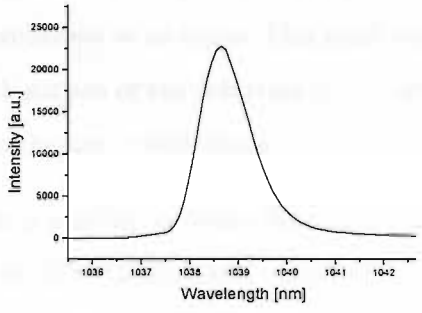

(b) Optical spectrum of 448 fs pulse.

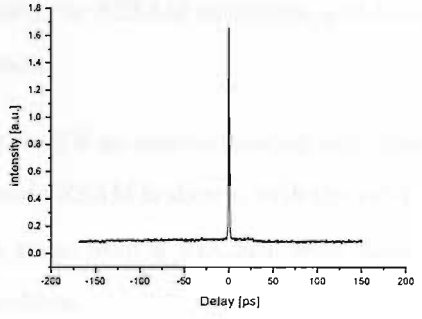

(c) Full range autocorrelation showing a clean single pulse with no sattelite pulses.

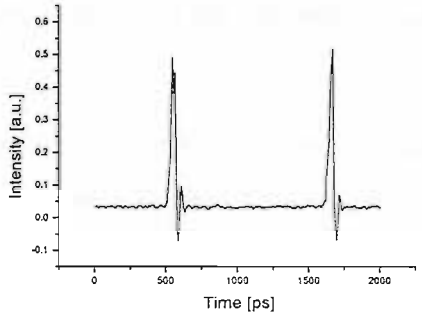

(d) Fast sampling socilloscope data of the pulse train, showing a single pulse per round trip.

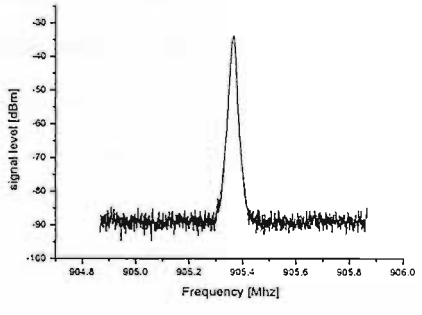

(e) First RF peak of the laser, showing a fundamental repetition frequency of 905 MHz.

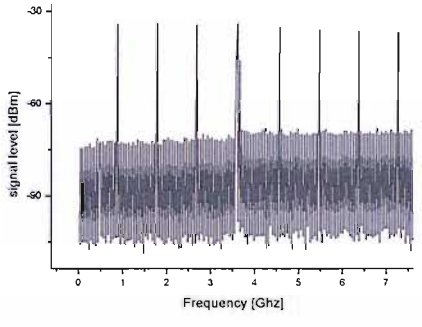

(f) Graph of the first 8 RF peaks of the mode locked laser. These show nearly equal amplitudes of all of the harmonics of the fundamental repetition frequency.

FIGURE 5.5: Complete laser characterisation of a mode locked VECSEL producing 448 fs pulses at a repetition rate of 905 MHz, with an average output power of 40 mW. The pulses are Fourier limited.

Further to the experimental evidence, these substrate reflections can be removed by mechanically polishing the back surface of the substrate at an angle. This small angle of $< 2^0$ causes the small reflections from the back surface of the substrate to be reflected at an angle and they are not coupled back into the laser cavity mode.

We have also observed, for the first time, that it is possible to obtain these fixed satellite pulses from reflections off the substrate of the SESAM. However, these are not due to direct coupling back into the laser cavity as the laser mode does not support these reflected pulses. It is suggested that these satellites are caused by the light reflected off the substrate bleaching the SESAM slightly, allowing a stable satellite pulse to be formed in the laser cavity. Again these satellites can be straightforwardly removed through angle polishing the SESAM substrate, and changing the direction of the light reflected off the substrate.

In Figure 5.6 an autocorrelation and optical spectrum from a VECSEL with unpolished gain and SESAM is shown, with the satellite pulses, and in Figure 5.7 the autocorrelation of the pulse from a VECSEL with angle polished gain and SESAM is shown, showing no satellites.

These satellite pulses caused by substrate reflections are undesirable for many applications, although the energy in these pulses is small. The satellite pulses can be removed through polishing and the rest of this work uses angle polished gain samples to reduce the problem of substrate reflections. Angle polished SESAMs are also used for a majority of the work reported here, although polishing the SESAM is not always necessary or desirable, as the process can easily damage the absorber structure, which is grown only 2 nm below the top surface of the sample, through the stress induced in the polising process. More recent samples have been grown on substrates with rough back surfaces, leading to a reduction of this problem, as any light hitting the back face of the substrate is then scattered, and not reflected back into the cavity mode.

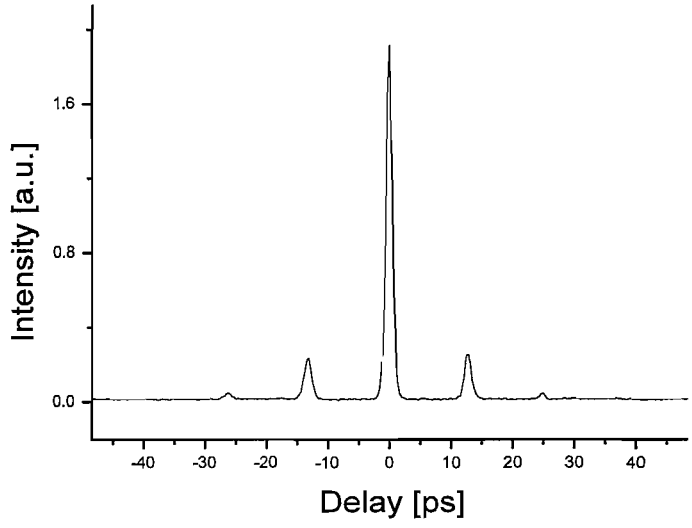

(a) An autocorrelation of the output pulse train of a mode locked VECSEL producing sub 500 fs pulses. This autocorrelation shows the satellite pulses which are seen to have a separation of 15 ps from the main pulse.

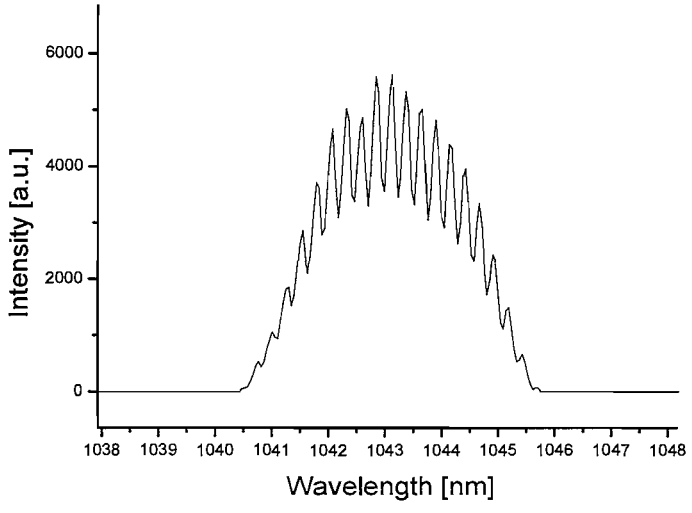

(b) Optical spectrum of the VECSEL producing satellite pulses an sub 500 fs pulses, showing modulations with a spacing of 0.15 nm.

FIGURE 5.6: Autocorrelation and optical spectrum of a VECSEL producing sub 500 fs pulses and satellite pulses, with unpolished gain and SESAM. Back reflections from the substrate of the gain couple back into the laser cavity, and back reflections from the SESAM bleach the saturable absorber to produce satellite pulses.

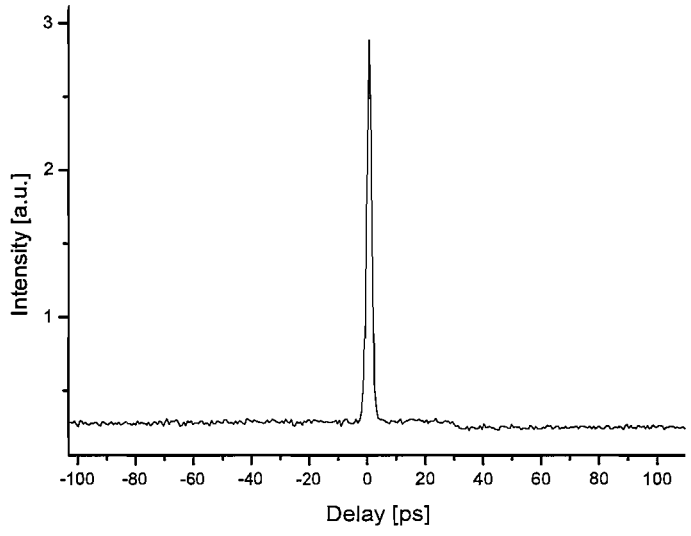

(a) An autocorrelation of the output pulse train of a mode locked VECSEL producing sub 500 fs pulses. This autocorrelation shows no satellite pulses.

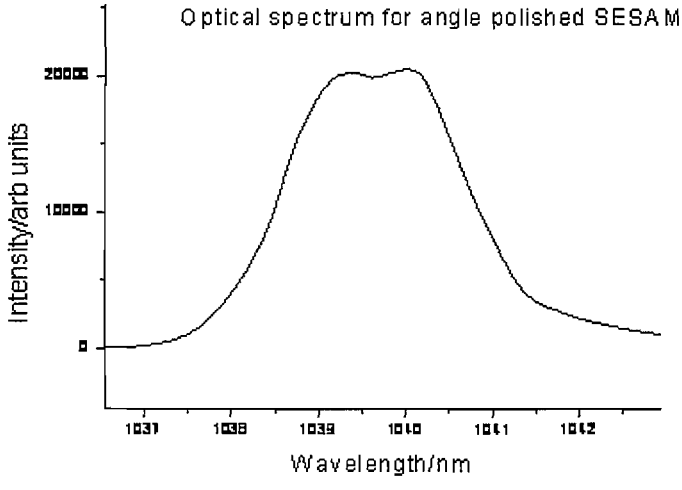

(b) Optical spectrum of the VECSEL producing sub 500 fs pulses, showing no modulations.

FIGURE 5.7: Autocorrelation a) and optical spectrum b) from a VECSEL producing sub 500 fs pulses and no satellite pulses, with polished gain and SESAM. Back reflections from the substrate of the gain do not couple back into the laser cavity, and back reflections from the SESAM do not bleach the saturable absorber to the same extent.

5.6 Multiple pulse operation

It has been observed for the first time that a mode locked VECSEL producing sub 500 fs pulses can operate in a multiple pulse regime, where there is more than one pulse oscillating intracavity. This multiple pulse operation has been experimentally investigated using a VECSEL mode locked at a fundamental repetition rate of 905 MHz. The laser had a 0.7% output coupler with a 50 mm radius of curvature, and a focusing mirror with a 38 mm radius of curvature. The pump power was changed across a range from laser threshold at 0.57 W to thermal rollover at 0.72 W incident pump power. The output power varied between 6 mW and 22 mW across this range. The laser output was characterised by recording the output power, autocorrelation, optical spectrum, RF spectrum of the fundamental harmonic, RF spectrum of the first 8 harmonics, and recording the pulse train using a 25 GHz bandwidth fast sampling oscilliscope.

It was experimentally observed that the number of pulses increased with increasing output power, from one pulse intracavity, up to 4 pulses intracavity. Figure 5.8 and Figure 5.9 show two regimes; the laser is operating with only one pulse in Figure 5.8 and two pulses per round trip as shown in Figure 5.9.

Figure 5.10 shows the output power and pulse number versus pump power and from this the transition from different numbers of pulses in the cavity can be clearly seen. It can be seen that for increasing output power, the number of pulses increases, and as the laser output power rolls over, due to thermal rollover, the number of pulses then decreases from four to three.

The same data set can be manipulated through simple calculation and displayed in the form of the intracavity energy divided by the number of pulses intracavity, revealing the intracavity pulse energy, which is shown in Figure 5.11. It is interesting to note that there is a relatively small range in the intracavity energy per pulse. A relatively straightforward approach to modelling the dynamics of the laser gain and absorption in the SESAM can be used to calculate the range of allowed intracavity energies; at one extreme the pulse energy must be great enough so that the gain equals unity, and at the other extreme the energy must be just below that needed for the laser to become

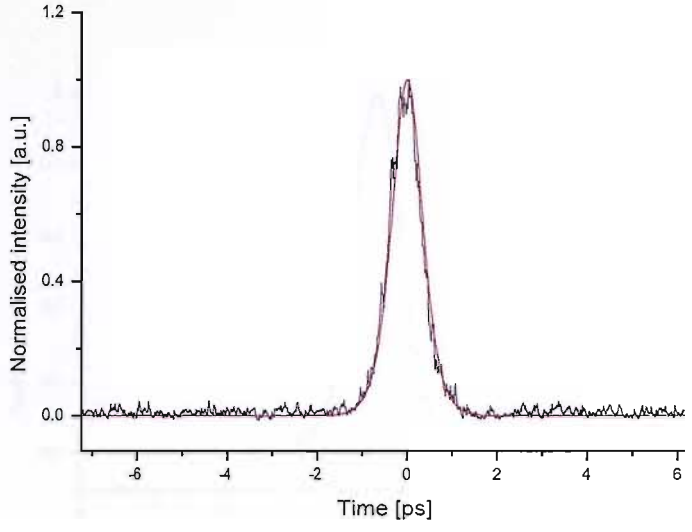

(a) Autocorrelation of VECSEL laser pulse train when operating in single pulse per round trip.

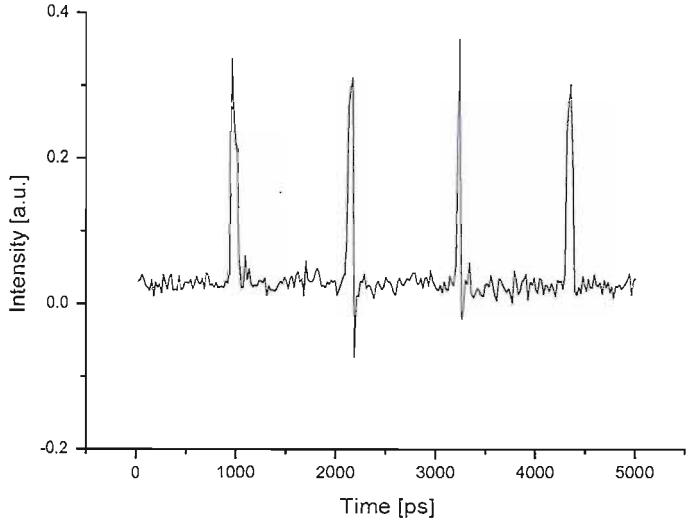

(b) Fast sampling oscilloscope trace of pulse train coming from laser showing only one pulse per round trip.

FIGURE 5.8: Autocorrelation and fast sampling oscilloscope trace of laser pulse train showing 523 fs pulses being produced with only one pulse per round trip time.

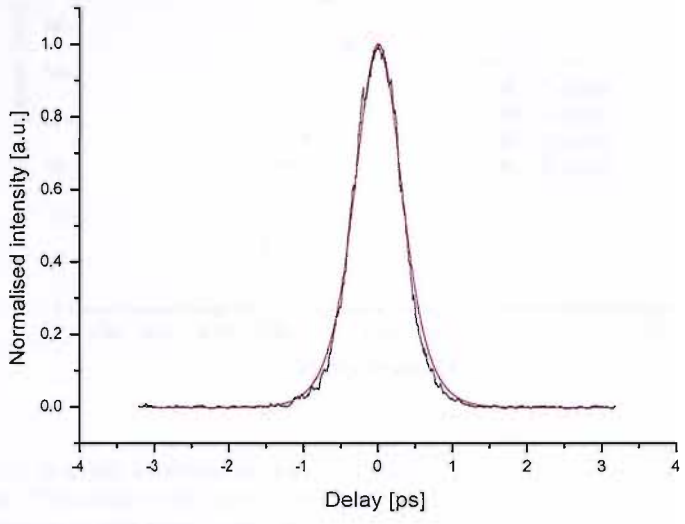

(a) Autocorrelation of laser pulse train showing a 485 fs pulse.

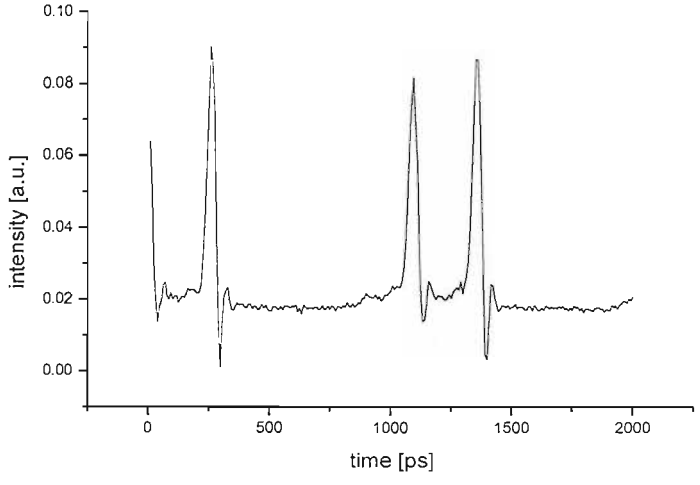

(b) Fast sampling oscilloscope trace showing two pulses per cavity round-trip time.

FIGURE 5.9: Autocorrelation and fast sampling oscilloscope trace of 485 fs pulses being produced, in a multi-pulse regime, with two pulses per laser round-trip time.

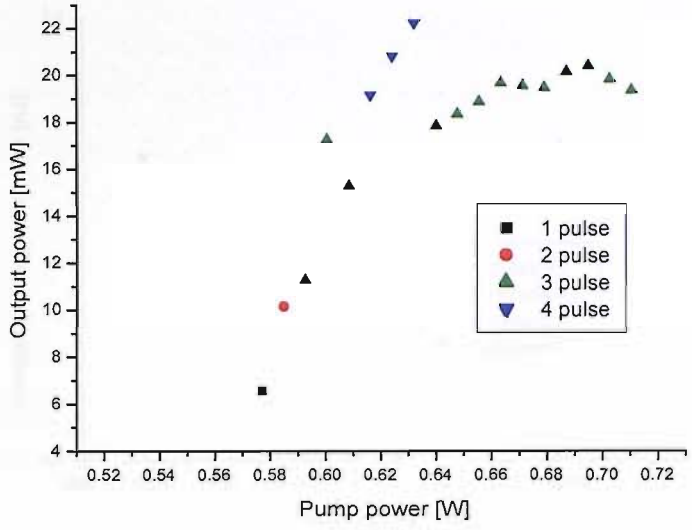

FIGURE 5.10: A graph ahowing the number of pulses per round trip versus the incident pump power. This shows the transitions from single pulse to 4 pulses circulating intra-cavity, occurring as the intra-cavity power increases. Thermal rollover is reached at high pump powers and the pulse number decreases to 3. Above the data range shown here the laser changed into a different regime, producing pulses with duration greater than 1 ps.

unstable against CW lasing. It is clear that if the intracavity energy is increased above the upper limit of this range, a second pulse will be formed, with the energy of each pulse within the range defined above. This can clearly be seen in Figure 5.11 where the individual intracavity pulse energy remains within a tight range, even when there are up to four pulses intracavity.

Multiple pulse operation is not desirable in a mode locked laser, as the pulse energy and peak power of the laser does not scale with increasing output power. Further to the undesirable property of pulse energy the application of multiple pulse VECSELs is made more complicated as the pulse spacing is not equal in the cavity, although the data from the fast sampling oscilliscope suggests that the energy in each pulse is normally equal, due to the equal amplitudes recorded on the oscilliscope. Intuitively, as the pulses have equal amplitude, one would expect the pulses to distribute equally throughout the cavity roundtrip time. However, this is not experimentally observed here and the pulses tend to appear in groups with a typical, although not rigorously constant, separation between the pulses of approximatly 150ps, followed by a large gap, making up the rest

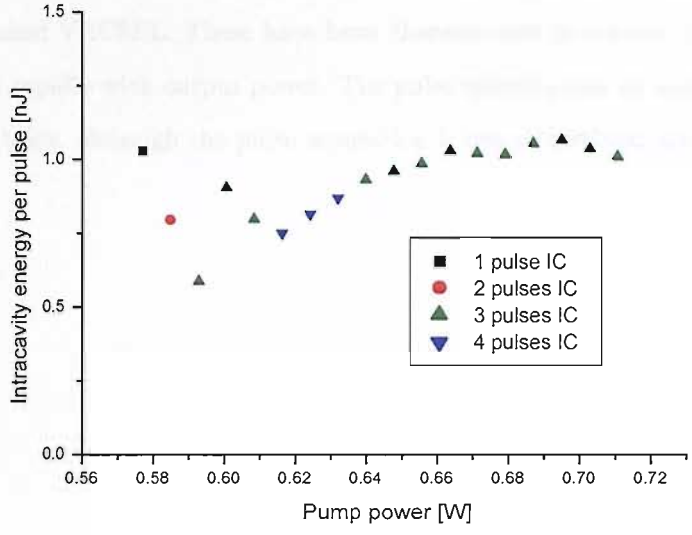

FIGURE 5.11: A graph showing the energy devided by the number of pulses circulating intracavity (the intracavity pulse energy) versus the pump power. This shows that the intracavity energy per pulse varies over only a small range, and the number of pulses varies to keep the energy per pulse within that range.

of the cavity round trip time. The processes that force this pulse spacing are not well understood.

5.7 Conclusions

We have shown the full characterisation of the SESAM QT1627, which is identical in design to the SESAM used for the first demonstration of sub 500fs pulses. This data has shown that the saturation fluence was lower than we had previously estimated and also the recovery time was significantly faster than previously estimated.

The characterisation of the two pulse regimes that can be achieved using gain sample QT1544 and SESAM QT1627 have been experimentally shown. We have also shown the presence of satellite pulses which are due to reflections off the gain substrate and can also be formed by reflections off the SESAM substrate bleaching the SESAM slightly, allowing for a satellite pulse to be formed. In both cases it has been shown that angle polishing the gain and SESAM fully removes these effects.

We have also reported for the first time the presence of multiple pulse operation in a sub 500fs mode locked VECSEL. These have been characterised in a laser where the pulse number varied rapidly with output power. The pulse splitting can be understood on an energy model basis, although the pulse separation is not understood and is still under investigation.

Chapter 6

Pulse duration limiting processes: towards producing shorter pulses

6.1 Introduction

Mode locked VECSELS have produced sub 500fs pulses directly from the laser oscillator with an optical spectrum with a width of 2.4 nm FWHM [60], but the gain bandwidth of these samples, measured previously for a CW VECSEL, using spectro-temporal measurement techniques, has been measured to be in 35 nm full width half maximum (FWHM) [1]. Mode-locking locks a bandwidth that is some fraction of the gain bandwidth and shorter pulses in the order of 100 fs could reasonably be expected to be experimentally achieveable. Other semiconductor lasers have been mode locked to produce pulses as short as 190 fs directly from the laser cavity [16], and pulses as short as 207 fs have been achieved by external compression of pulses produced by a mode locked semiconductor laser [14], showing the potential of semiconductor lasers.

The possibility of generating shorter pulses directly from the laser cavity could extend the range of potential applications. For example, with 100fs pulses the peak power would be approximately five times higher than that currently achieved with a VECSEL, at the same output power. Shorter pulses would also be useful for many applications such as pump-probe experiments where the pulse duration limits the time resolution, and THz

generation where the pulse duration is one of the parameters defining the bandwidth of the THz radiation generated.

A VECSEL producing 100 fs pulses directly from the laser cavity, coupled with high average output powers which have already been demonstrated by other groups [8] [44], would make this type of mode locked laser an attractive option as a cheap source of femtosecond pulses to a wide market.

Here I report the first detailed experimental analysis of the mode-locking mechanisms of a mode locked VECSEL, and in particular in the ac-Stark regime where 500 fs pulses are produced. The key issue is to identify those mechanisms that limit the bandwidth of the stable pulse to a small fraction of the gain bandwidth.

6.2 Theory of laser build-up dynamics and methods of producing a broad gain bandwidth

6.2.1 Theory of the laser dynamics during the build-up to steady state

The discussion and theory of the spectral and temporal dynamics of the laser during the build-up time before mode-locking onsets are described well in [63]. [63] is a discussion of the limits of laser intra-cavity spectroscopy and is based on a four level laser with homogeneously broadened gain.

Semiconductor lasers can not be well described by a four level system as they are two level systems with a large population in the lower energy state. This difference does however only really affect the probabilities for spontaneous and stimulated recombination rates [64]. The four level system can be described by rate equations for the photon number M_q in a laser mode, q and for the inversion, N. these equations can be written as Eq.(6.1) and Eq.(6.2):

$$\frac{d}{dt}M_q = -\gamma M_1 + B_q N(M_q + 1) - k_q c M_q + F_q(t), \tag{6.1}$$

$$\frac{d}{dt}N = P - AN - N\sum B_q M_q, \tag{6.2}$$

where γ is the broadband loss of the cavity, given by $\gamma = -cln[R_{OC}(1-l_i)^2]/2L$ where R_{OC} is the reflectivity of the output coupler, l_i is the internal loss and L is the cavity length. A is the spontaneous decay rate of the upper level in the laser, and P is the pump rate. B_q is the stimulated emission rate into mode q, which is taken at half width half maximum (HWHM) as Eq.(6.3). At the central mode, q_0 the stimulated emission rate is a maximum of B_0. The spectral variation in this equation is given in units of mode-spacing, $\Delta q = \Delta v 2L/c$.

$$B_q = B_0 \frac{1}{1 + [(q-q_0)/Q]^2} \tag{6.3}$$

When a laser starts to operate the laser dynamics occur on several different timescales. The first timescale is the timescale taken for the carrier population to reach steady state. This occurs on the range of a few hundred femtoseconds for a semiconductor laser and is not an important part of the following dynamics.

The second timescale is due to the build-up of photons in the laser cavity. The number of photons in the cavity increases exponentially after the carrier population reaches steady state. This increase in photon number continues until the total photon number begins to saturate and reaches its steady state value. The steady state total photon number in the cavity, $M = \sum M_q$, is given by $M = A(\eta - 1)/B_0$. The time for this saturation is given by Eq.(6.4):

$$\tau_m = ln(M)[\gamma(\eta - 1)]^{-1}, \tag{6.4}$$

Once the photon number reaches its steady state, the cavity loss is compensated by the gain at the central mode only. The modes away from the central mode see more loss than the central mode, and the photon number in these modes begin to decrease,

increasing the photon number of the central mode. This redistribution occurs since the total photon number has reached steady state.

This redistribution of the photons from the surrounding modes towards the central mode leads to spectral narrowing, which is called spectral condensation. In a CW laser this effect would continue until the steady-state linewidth of the laser is reached. This occurs when the narrowing effect due to spectral condensation is compensated for by broadening effects due to spontaneous emission. On the other hand in a mode locked laser, the mode-locking mechanism locks many modes together and halts the spectral condensation processes from further narrowing the bandwidth below that which is locked. The spectral width at half width half maximum (HWHM) of the laser varies with time during this period of spectral condensation as Eq.(6.5):

$$\Delta\upsilon = \sqrt{\frac{ln(2)}{\gamma t'}}Q, \tag{6.5}$$

where t' is the time after the total number of photons has reached a steady value. In other words $t' = t - \tau_m$.

When the laser is mode locked with the insertion of a SESAM, the intra-cavity losses are increased, both in terms of non-saturable losses and saturable losses. This increase in the total loss leads to faster spectral narrowing, with the spectral condensation being a stronger effect in the buildup dynamics.

Experimental measurement of the mode-locking onset time provides some information on the dynamic behaviour and strengths of the spectral condensation mechanism, which is tending to narrow the optical spectrum, and the mode coupling due to the saturable absorber, which is trying to broaden the optical spectrum. Further to this spectro-temporal measurements, measuring the optical spectrum evolution with time, allow the combined effects of spectral condensation and spectral broadening due to the mode-coupling in the SESAM to be directly seen.

6.2.2 Design parameters to produce broader bandwidth samples

A broad gain bandwidth in a VECSEL gain structure can be achieved by the careful design of the quantum wells and the microcavity formed around the quantum wells by the DBR and the window layers. Current work for mode locked VECSELs has only focused on the control of the micro-cavity, as the pulses generated to date are not limited by the available bandwidth of the gain structures.

The micro-cavity can be designed to be anti-resonant with the quantum wells at the designed laser wavelength making the gain spectrally broad, as there is no preference forced by the micro-cavity across the quantum well gain. The anti-resonant micro-cavity does however reduce the total gain of the laser by reducing the intensity of the light interacting with the quantum wells in the active gain region. Resonance and anti-resonance is described in more detail in 2.

In this work the gain sample used is near antiresonant at the design wavelength. The window layer is chosen to be $1.45\lambda/4$. The use of a near anti-resonant gain structure has been shown to increase the gain bandwidth from 18 nm to 35 nm [1].

6.3 Previous experimental results measuring the gain bandwidth and mode-locking onset time.

For shorter pulses to be produced a broader gain bandwidth is needed. Spectro-temporal measurements performed by Sjored Hoogland and Aurnaud Garnache on a CW VECSEL have shown that the laser gain bandwidth is in the order of 30 nm. This experiment and measurements are described in [1].

In these experiments, the total losses of the cavity are low and the evolution of the optical spectrum to steady-state were slow, in the order of 100 μs. As the fixed losses are increased, the time over which the spectrum narrows decreases. This is because as the losses are increased, the gain that is needed to compensate the loss also increases, leading to the gain filtering the spectrum more strongly per pass. This was previously demonstrated by the use of two different output couplers of differing loss [1]. The

main results previously reported show that by the design of the microcavity in the gain structure, the gain bandwidth was shown to have increased from 18 nm to 34 nm between two different samples, one resonant and the second near anti-resonant [1].

The mode-locking onset time had previously been measured by S. Hoogland [1] for a long cavity VECSEL with a repetition rate of 324 MHz producing 4.3 ps pulses. This was measured as 4 μs, corresponding to approximately 1000 roundtrips.

In this work we report the mode-locking onset measurements of a VECSEL in a 1.2 GHz repetition rate laser, with three different pulse regimes; 2.5 ps, 630 fs and 480 fs. The spectro-temporal evolution of the optical spectrum has also been measured for the mode locked VECSEL in the 480 fs pulse regime.

6.4 Mode-locking onset measurements

6.4.1 Method

The mode-locking onset time can be measured using the setup as shown in Figure 6.1. An optical chopper is placed intra-cavity to modulate the laser output. The optical chopper speed is set at 400 Hz, and the chopper blade is positioned near a waist in the cavity mode to ensure that the effect of the blade blocking and unblocking the laser cavity mode has a negligible effect on the laser build-up dynamics.

The chopper uncovers the laser mode, but the losses due to the chopper blade blocking the laser mode are too high to allow the laser to start to lase until it is uncovering the last 5% of the laser mode. The chopper has been calculated to move from causing a loss of 5% to not overlapping the laser mode at all in a time of 0.15 μs. This is sufficiently fast not to be significant in the build-up process, where the evolution to steady state takes place on a time scale of approximately 20 μs.

The laser is modulated in this fashion as opposed to direct modulation of the pump diode because modulation with an optical chopper maintains the same pumping level on the gain and hence the same local temperature of the gain remains near constant. This

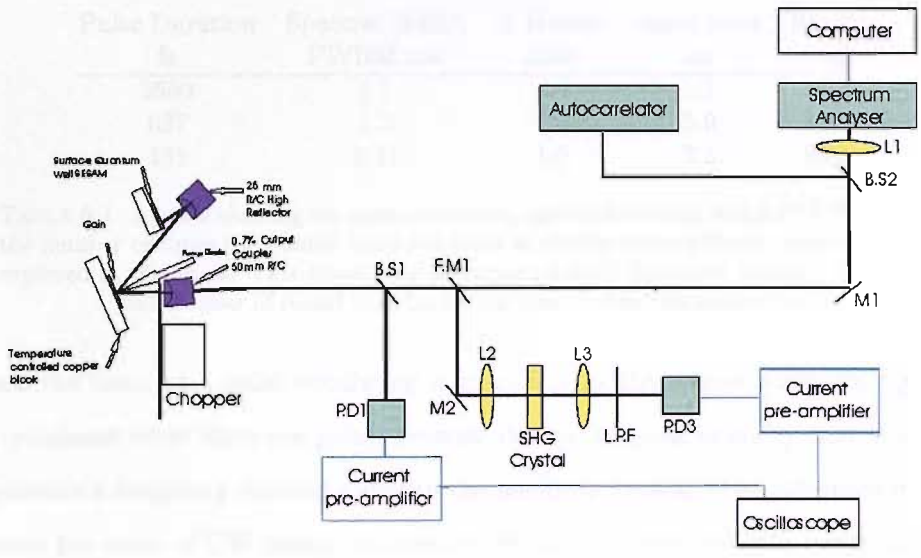

FIGURE 6.1: A schematic of the experimental setup used for mode-locking onset measurements. A portion of the laser output is detected by a photodiode, to show the buildup of the CW laser, a second portion is passed through a SHG crystal and detected to reveal the mode-locking buildup curve. The experimental setup also allows the autocorrelation and optical spectrum of the laser at steady state to be measured.

minimises unwanted thermal effects which would alter the laser dynamics, although there will still be some temperature variation of the active region due to the laser itself being modulated, which in turn means that the laser cooling effect in the gain is modulated. This modulation due to the modulation of the laser cooling effect should be a small effect compared to directly modulating the pump laser.

The mode-locking onset is experimentally obtained by measuring the change in intensity with time of both the fundamental laser light and the frequency doubled second harmonic of it. A schematic of the setup used for this is shown in Figure 6.1. The output beam is split by a 98:2 beam splitter and the 2% component is detected by an InGaAs photodiode with a 1 GHz bandwidth. The remaining 98% of the laser output is focussed into a nonlinear Lithium Niobate crystal. The output of the second harmonic signal is then detected by a Si photodiode with a 1GHz bandwidth, with a short pass filter in front to block the remaining fundamental signal.

A build-up curve is obtained on a digital oscilloscope for both components. The fundamental laser light build-up curve shows the onset of CW lasing followed by the increase of output power after this, until a steady state is reached. The frequency doubled signal

Pulse Duration fs	Spectral Width FWHM nm	X Fourier limit	onset time μs	Round trips
2500	1.1	2.4	1.1	1350
627	1.1	1.4	3.9	4700
481	2.37	1.0	7.1	8500

TABLE 6.1: A table showing the pulse durations, optical spectrum width (FWHM) and the number of times the Fourier limit the pulse is, for the three different pulse regimes explored in this work. This also shows the expermentally measured buildup time and the number of round trips inside the laser cavity this relates to.

reveals the onset of a pulse circulating intra-cavity, as the second harmonic signal is only produced when there are pulses present, due to the peak intensity that is needed to generate a frequency doubled signal in the nonlinear crystal. The difference in time between the onset of CW lasing, as measured by the fundamental light curve, and the onset of the mode-locked operation shown by the second harmonic light curve, gives the mode-locking onset time.

6.4.2 Mode-locking onset results for different pulse durations

The laser used in this experiment was a standard Z cavity VECSEL with a 1.2 GHz repetition rate and an output power of 20 mW for a pump power of 1 W. QT1544 was used as the gain and QT1627 as the SESAM. It had a 0.7% output coupler with a radius of curvature of 50 mm, a high reflector wih radius of curvature 25 mm and a mode waist on the gain of radius 65 μm and 11 μm on the sesam. This laser was chosen as the pulse formed from the laser could be altered by adjusting the gain temperature alone, whilst the other laser parameters, including output power and hence intra-cavity power, remained constant. With gain temperature tuning the laser could be switched between three different mode-locking regimes, producing pulses as described in Table 6.1 and shown in Figure 6.2.

The mode-locking onset graphs are shown in Figure 6.3. From these results it can be seen that the mode-locking onset time increases as the pulse duration decreases. The mode-locking onset times are shown in Table 6.1. The experimental data shows that as the pulse duration decreases, the mode-locking onset time increases.

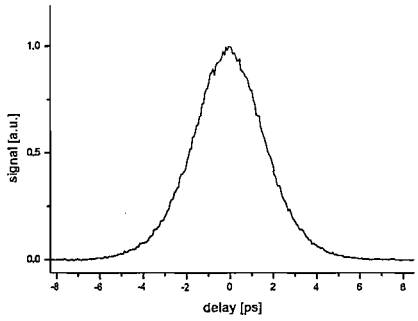

(a) Autocorrelation of 2.5 ps pulse regime

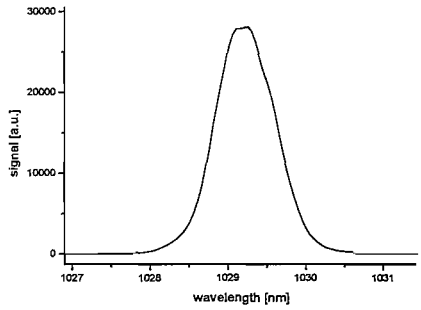

(b) Optical spectrum of 2.5 ps pulse regime

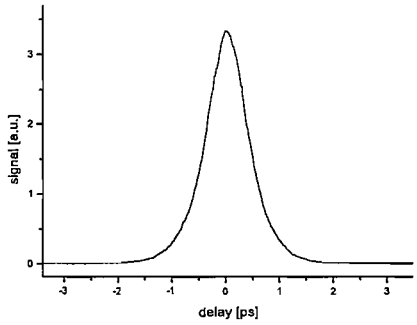

(c) Autocorrelation of 627 fs pulse regime

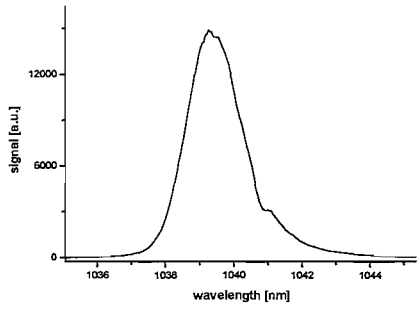

(d) Optical spectrum of 627 fs pulse regime

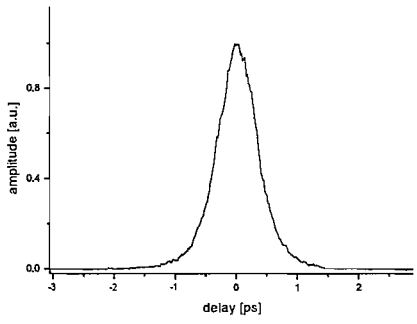

(e) Autocorrelation of 481 fs pulse regime

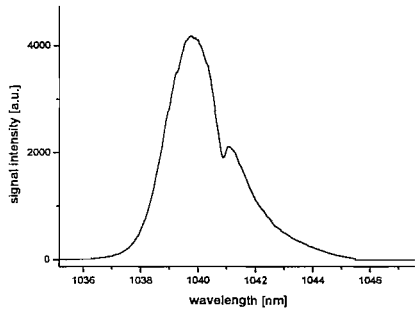

(f) Optical spectrum of 481 fs pulse regime

FIGURE 6.2: Optical spectrums and Autocorrelations for the three mode-locking regimes showing pulse durations of 2500 fs a) b), 627 fs c) d), and 481 fs e) f). The laser output power remained constant at 20 mW and the pump power was constant at 1 W.

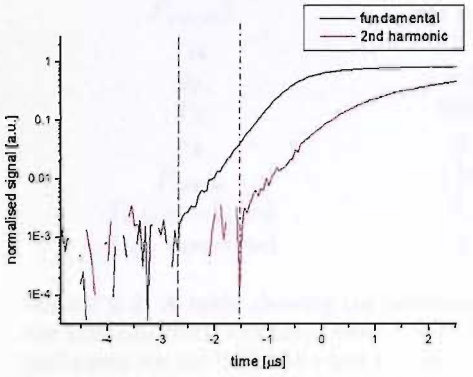

(a) Mode-locking onset time when the laser produced 2500 fs pulses.

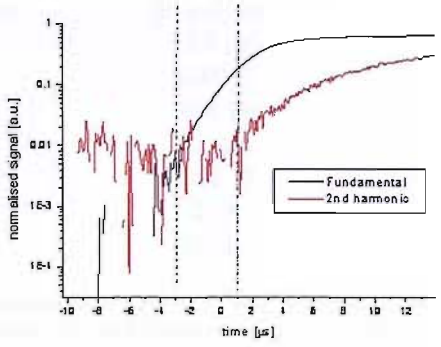

(b) Mode-locking onset time when the laser produced 627 fs pulses.

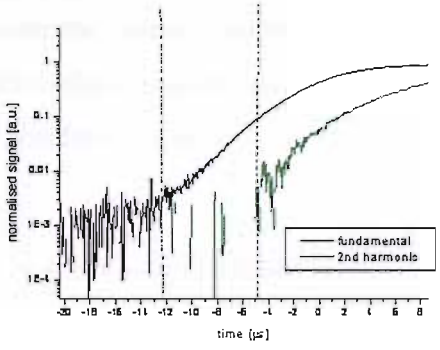

(c) Mode-locking onset time when the laser produced 480 fs pulses.

FIGURE 6.3: Mode-locking onset time measurements for the three different pulse regiemes investigated, with the laser producing 2.5 ps a), 627 fs b) and 481 fs c) pulses respectively. The time between the onset of CW lasing, shown by the IR light, and the mode locked operation, shown by the frequency doubled greeen light is the mode-locking onset time.

6.4.3 Discussion of results and conclusions

The mode-locking onset time measured for the 2.5 ps pulse regime was 1.1 μs which relates to 1350 roundtrips. This result is comparable to the onset time measured for the laser investigated previously by Hoogland [1]. This shows there is good agreement with the overall trend and dynamics, which should not relate to the cavity design, but to the properties of the gain medium and the SESAM as well as the relative fixed losses.

In this case a different SESAM was used with the same gain structure. The SESAM used

What	previous work values	new ps
$F_{sat,sa}$)	100 $\mu J/cm^2$	56 $\mu J/cm^2$
τ_{sa}	4 ps	3.8 ps
q_0	0.007	0.0032
T_R	3086 ps	833 ps
r_A	10 μm	11 μm
$P_{ave,ic}$	4.57 W	2.86 W
T_{mbt} predicted	4 μs	2 μs
T_{mbt} measured	4 μs	1.1 μs

TABLE 6.2: A table showing the parameters estimated or measured for SESAMs from the previous work described described by Hoogland [1], and those used in this work, as estimated for the SESAM when the laser is producing 2.5 ps pulses. Further details of the properties of SESAM QT1627 can be found in 5, where the full characterisation of the SESAM is described.

was a resonant SESAM grown by low temperature MBE. However for the 2.5 ps pulses produced in this experiment the central wavelength was 1030 nm, which is resonant with the absorption in the surface quantum well SESAM used. In this case, although the exact type of SESAM is different, as is the recovery times, the basic properties should be comparable.

The results obtained can be explained using Eq.(6.6) from U.Keller [65]. This equation is for slow saturable absorbers in solid state lasers, which typically have slightly different parameters due to the difference in the gain medium compared to solid state lasers which typically have more gain per pass and also much longer upper level life times (1 μs vs 1 ns). However S. Hoogland showed that this equation could be used to give good agreement with experimentally obtained data for VECSELs [1].

$$T_{mbt} = \frac{F_{sat,sa}}{2q_o}\frac{1}{\tau_{sa}}\frac{A_{sa}}{P_{ave,ic}}T_R \tag{6.6}$$

From the above experiments the parameters that change between the different pulse regimes are recovery time of the saturable absorber (τ_{sa}), modulation depth (q_0) and saturation fluence of the SESAM ($F_{sat,sa}$).

Comparing the parameters for the VECSEL when it is producing 2.5 ps pulses and 470 fs pulses as shown in Table 6.2, one can see that as the recovery time of the saturable absorber (τ_{sa}) gets shorter, the mode-locking onset time (T_{mbt}) gets longer. As the laser

moves to producing the shortest pulses from ps pulses the laser moves to longer wavelength, from 1030 nm to 1040 nm. This shift in wavelength means that the SESAM moves from working in a resonant absorption regime, with only a slow saturable absorption of the order of 4 ps, to a band edge absorption regime. In this second regime the ac-Stark effect is also exploited, which is a near instantaneous effect. In this case the SESAM recovery time is a combination of the fast effect and the slow saturable effect and hence the characteristic recovery time should be shorter than for the regime producing picosecond pulses. This decrease in the recovery time causes an increase in the mode-locking onset time.

At the same time the modulation depth (q_0) also decreases, causing an increase in T_{mbt}. When the laser produces 2.5 ps pulses, the laser wavelength is resonant with the QW absorption in the SESAM. This gives a modulation depth of approximately 0.32%. In the 470 fs pulse case the laser wavelength is increased to 1040 nm, which is on the long wavelength side of the QW band edge. In this case the modulation depth is therefore decreased as the absorption is non-resonant. This decrease should be in the order of a factor of 3 from the SESAM photoluminescence, which can be seen in Figure 6.4.

Finally the saturation fluence ($F_{sat,sa}$) also changes between the two pulse regimes. The saturation fluence, the energy per unit area needed to saturate the loss depends on the intensity of the E-field on the QW. The intensity on the QW is wavelength dependent as the standing wave in the SESAM micro-cavity changes. From SESAM design calculations it is predicted that the intensity on the QW increases slightly as the laser wavelength moves from 1030 nm to 1040 nm as shown in Figure 6.4. This change in the intensity on the QW means that $F_{sat,sa}$ decreases a small amount between the 2.5 ps and the 470 fs regime. On the other hand, when the laser produces sub 500 fs pulses, the ac-Stark effect plays a role in the pulse shaping mechanism. The strength of the ac-Stark effect scales as 1/(Energy detuning). The saturation fluence of the ac-Stark effect should therefore be larger than that of the resonant absorption, where real carriers are created, instead of the virtual carriers, causing a bandedge shift.

However it is important to note that the ac-Stark effect is a different saturation effect compared to the resonant effect seen at 1030 nm. The strength of the band edge shift

from the ac-Stark effect depends on the detuning of the laser wavelength from the exciton resonance and scales as $1/\Delta E$. Therefore estimating the saturation fluence in this regime is not possible. It would be useful to measure the saturation fluence which can simply be done, assuming that a test laser operating at the correct wavelength is available.

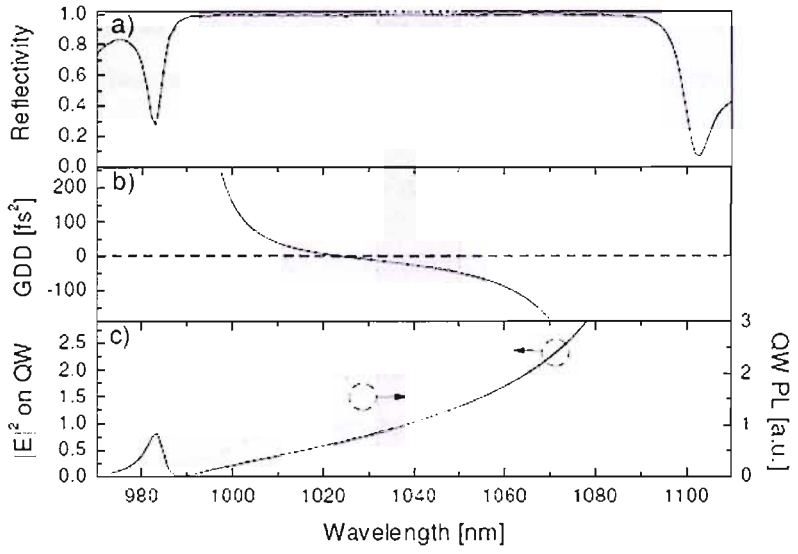

FIGURE 6.4: The design properties of the ac Stark effect SESAM, QT1626. Graph a) shows the designed reflectivity, b) shows the GDD and c) shows the squared modulus of the E-field on the quantum well. It can be seen that as the wavelength increases the squared modulus of the E-field on the quantum well also increases slightly [1].

6.5 Spectro-temporal measurements on a 500fs mode locked VECSEL

6.5.1 Introduction

The increase in the mode-locking onset time with shortening pulse length produced is interesting as this means that as the steady state pulse duration decreases the relative strengths of the spectral condensation effect and the mode coupling effect due to the saturable absorber change. In particular this gives some evidence of the fact that different effects are operating in the regime of picosecond pulse production compared to femtosecond pulse production, as the dynamics due to competing effects develop on different timescales. The gain bandwidth has previously been measured and it has been

shown that in theory this gain sample could be used in a VECSEL producing 100fs pulses.

Spectro-temporal measurements of the laser dynamics during this build-up process reveal the gain bandwidth of the laser as well as measuring other filtering effects that may be taking place such as a filtering effect due to the bandwidth of the absorption in the SESAM. The gain bandwidth measured in a mode locked laser using this method should be different to that from a CW laser because as well as the spectral condensation effect there are also competing effects due to the mode coupling from the SESAM.

These measurements described here were performed on a mode locked laser producing 481 fs pulses. In this regime the ac-Stark effect at the band edge is utilised, producing some fast pulse shaping as well as the slower pulse shaping due to the slow saturable absorber. This is of particular interest as the shortest pulses we have been able to produce are 448fs as opposed to the theoretical limit of around 100fs due to the gain bandwidth.

6.5.2 Method

Spectro-temporal measurements were performed using the setup shown in Figure 6.5. The signal from the optical chopper was used to trigger a variable delay signal generator. This was then used to trigger a short pulse generator, producing a 400 ns pulse at the AOM RF driver, which then drove the Accusto-Optic Modulator (AOM). The deflected beam was then directed to an optical spectrum analyser.

This system allowed the 400 ns window to be moved to look at any delay from laser start up through the mode-locking build up process. The mode-locking build-up data was also taken at the same time to confirm that the data obtained from this experiment was consistent with that obtained from the mode-locking build-up experiment described above.

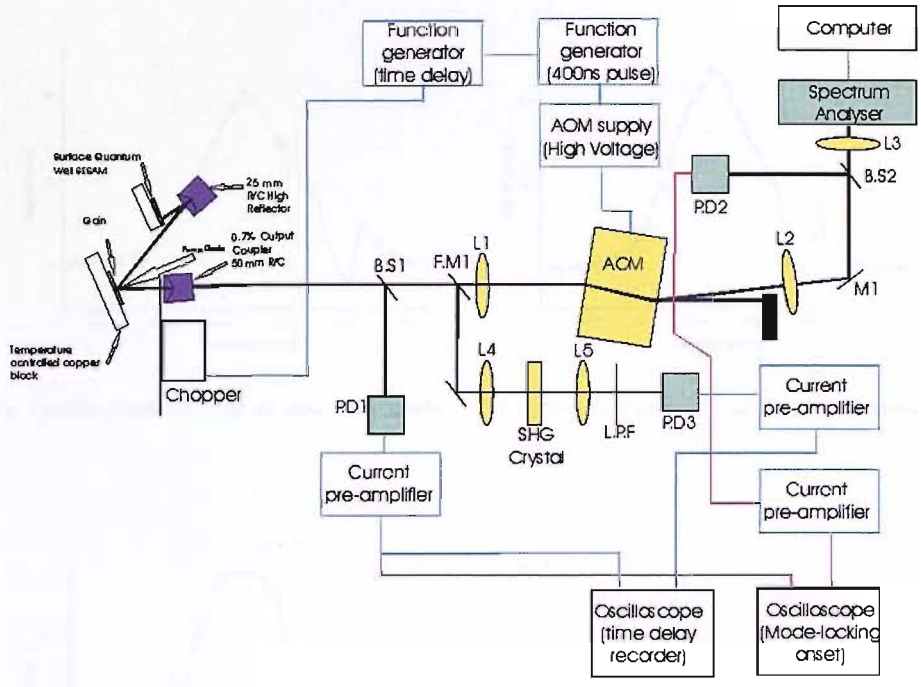

FIGURE 6.5: A schematic diagram of the experimental setup used for spectro-temporal measurements, allowing for spectro-temporal and mode-locking onset measurements to be taken for the same laser operating perameters.

6.5.3 Results

The evolution of the optical spectrum can clearly be seen in Figure 6.6. The optical spectrum has a width of 5 nm FWHM 1.245 μs after laser start-up. At 7 μs after laser start-up the optical spectrum has narrowed to 2.37 nm FWHM.

In the optical spectrums in Figure 6.6 a dip in the data can be seen at 1040 nm, particularly at the earliest build-up times. This dip is due to the background leakage through the AOM when it is off. This small signal integrated over the long period that it exists for is greater than the signal from the 400 ns pulse used for the spectro-temporal measurements. This background noise was corrected for by the spectrometer data acquisition program, although it can be seen that the small variation in this signal leads to the background being over estimated at these earliest build-up times.

Figure 6.7 shows the inverse bandwidth versus the generation time for the laser and from the linear fit to this data the gain bandwidth can be calculated using Eq.(6.5). When this calculation is performed the calculated effective gain bandwidth for the laser in a

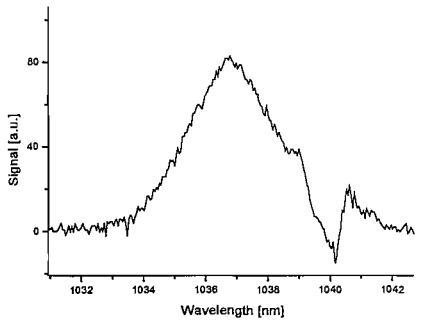

(a) Optical Spectrum 1.245 μs after lasing starts

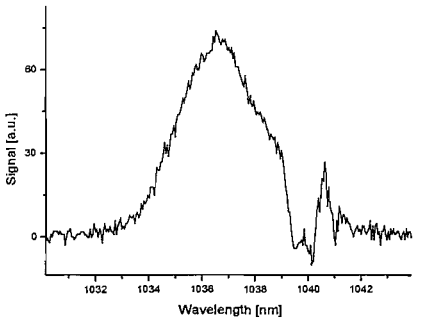

(b) Optical Spectrum 1.31 μs after lasing starts

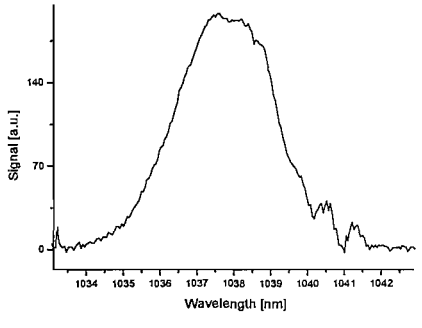

(c) Optical Spectrum 4.39 μs after lasing starts

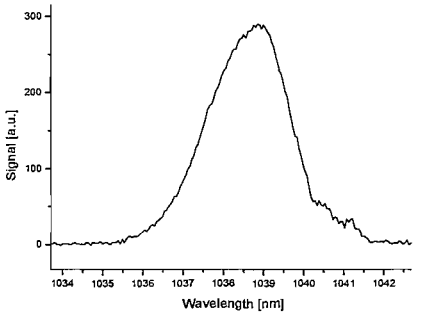

(d) Optical Spectrum 7 μs after lasing starts

FIGURE 6.6: Evolution of the optical spectrum at several different CW lasing buildup times, until the mode-locking onset of 481fs pulses, measured using the mode-locking onset measurements reported baove. It can be seen that at the mode-locking onset time the optical spectrum has evolved to be 2.37 nm broad. At this point the pulses produced have a time bandwidth product of 0.315, the theoretical limit for sech^2 pulses of this duration.

regime where it produces 481 fs pulses after mode-locking onset is approximately 32 nm FWHM.

6.5.4 Discussion of results and conclusions

The laser spectrum narrows extremely quickly due to the high fixed losses and non-linearities due to the insertion of the SESAM. This increase in fixed losses means that the filtering of the spectrum by the gain bandwidth is larger per pass, and the spectrum narrows faster, than for an equivalent lower fixed loss laser. When the spectro-temporal

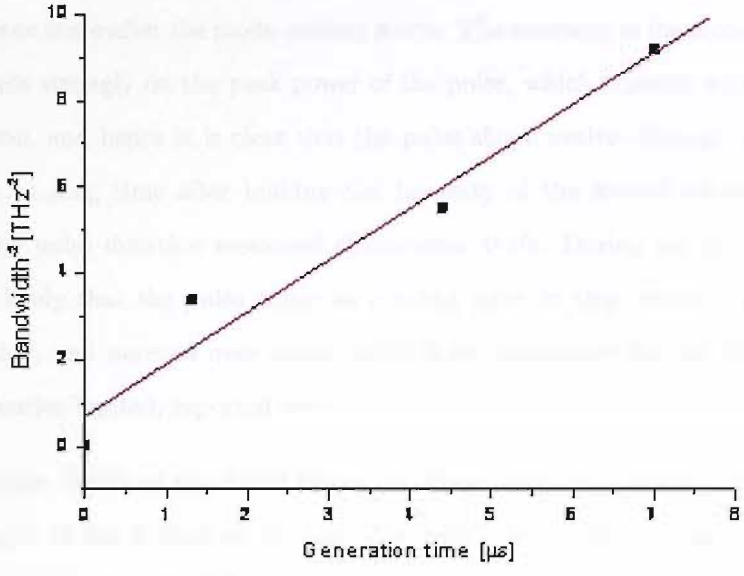

FIGURE 6.7: A graph showing the inverse bandwidth squared (HWHM), as measured from the data shown in Figure 6.6, versus the generation time after laser start-up. From this data the gain bandwidth can be calculated.

measurements were previously performed by Hoogland, the spectral condensation took place on a time scale of up to 200 μs.

These spectro-temporal measurements show that the optical spectrum narrows quickly during the period before mode-locking onset. The time for mode-locking onset as measured from the previous section was found to be 7 μs in the sub 500 fs pulse regime. From this spectro-temporal measurement it can be seen that after a delay corresponding to the mode-locking onset time the optical spectrum has narrowed to 2.37 nm (FWHM). The pulses produced from this laser in this regime were measured to have duration 481 fs with a sech^2 profile. The time bandwidth product of the optical spectrum width and the pulse duration leads to a figure of 0.315, the value for a Fourier-limited pulse.

The spectro-temporal measurements reported here, along with the mode-locking buildup measurements also reveal another interesting point about the 500 fs pulse regime; the optical spectrum evolves until the competing effects of the spectral condensation and the mode coupling due to the SESAM are in equilibrium. This spectral equilibrium is reached as soon as a pulse is formed, even though it is clear from the mode-locking

buildup measurements that the strength of the second harmonic signal increases for a further 20 μs or more after the mode-locking starts. The intensity of the second harmonic signal depends strongly on the peak power of the pulse, which depends strongly on the pulse duration, and hence it is clear that the pulse shape evolves during this time. At steady state, a long time after buildup the intensity of the second harmonic can be related to the pulse duration measured of duration 481fs. During the buildup time it is therefore likely that the pulse starts as a broad pulse in time which is many times Fourier-limited, and narrows over many round trips to produce the sub 500 fs pulses, which are Fourier-limited, reported here.

The modulation depth of the SESAM can be chosen with care through the selection of the strength of the E-field on the quantum well due to the microcavity effect. In this case, by increasing the E-field on the quantum well the modulation depth could be increased. This would also affect the saturation fluence, which would be reduced by increasing the strength of the coupling between the quantum well and the optical field. These changes should increase the strength of the mode-coupling potentially leading to shorter pulses and broader stabilised optical spectrums as a different equilbrium could be reached.

The value obtained for the gain bandwidth is in close agreement with that measured previously at 35 nm in a CW laser. The small decrease to 32 nm as measured here could be due to the filter function of the SESAM, which does not have a uniform broadband loss across the gain bandwidth, although the two values are in agreement within experimental errors. This loss should filter the gain slightly and hence slightly reduce the effective bandwidth, although the effect is small as the magnitude of the loss compared to the magnitude of the gain is small, and hence the effect should be many times weaker than the filtering effect of the gain.

6.6 Conclusions and future directions for producing shorter pulses directly from a VECSEL

As can be seen from the mode-locking onset time and spectro-temporal measurements performed, the pulse duration of the shortest experimentally demonstrated pulse from a VECSEL so far is limited by the relative strength of the mode coupling provided by the ac Stark SESAM compared to the spectral condensation effect. It has also been demonstrated that these gain structures have an available optical bandwidth of approximately 30 nm, of which a fraction of this could be expected to be mode locked, and could easily support 100 fs pulses directly from the laser oscillator. To move towards producing shorter pulses, not only does the balance of dispersion and self phase modulation as described by the quasi-soliton pulse formation mechanism [41] need to be carefully maintained, but also the design of the SESAM needs to be addressed to increase the relative strength of the mode coupling effect which is being employed relative to the strength of the spectral condensation effect.

A method to achieve shorter pulses would be to utilise a different faster pulse shaping mechanism, such as a Kerr lens. A Kerr lens would normally be formed using the sapphire gain crystal in a Ti:Sapphire laser, but the non-linear coefficients are relatively small, meaning only a weak lens is induced for the intra-cavity intensities in mode-locked VECSELs, so for the VECSEL it is preferable to use a material such as ZnSe which as a nonlinear coefficient a factor of 10 larger. This has been attempted using polycrystalline ZnSe, but the losses due to Two Photon Absorption (TPA) in this were too large to produce a working laser. A different material such as single crystal ZnSe could be used as this should reduce this effect. It has also been suggested that a photonic crystal structure in filled with a polymer would produce a strong Kerr effect and produce stable mode-locking [58]. In this case, the polymer has a much larger nonlinear coefficient and also the structuring of the photonic crystal enhances the effect.

Reducing the fixed losses of the cavity would further increase the available locking bandwidth by slowing the spectral narrowing that is seen in the laser, potentially allowing a

different equilibrium with more bandwidth and shorter pulses to be reached. The other properties of the saturable absorber would however need to be maintained

Future work should look at designing a band edge, ac-Stark design SESAM as we have used here, but with increased intensity on the QW, such that this increase counteracts the decrease on modulation depth and absorber recovery time, leading to stronger mode coupling and hence potentially broader optical bandwidths at equilibrium. This would give the potential for shorter pulses to be produced, if other pulse shaping mechanisms such as dispersion and self phase modulation are carefully controlled. This all semiconductor approach to shorter pulse duration would also ensure complexities due to a Kerr lens and cavity stability issues are not a problem, leading to the potential for a turn key, easy to operate system.

Designing a SESAM to achieve shorter pulses requires one to maintain a saturable absorber carrier recovery time on the order of 4 ps, as well as the use of the fast saturable absorber effect, the ac-Stark effect, whilst maintaining low non-saturable losses. The design used to demonstrate sub 500fs pulses utilises a QW 2 nm from the surface of the sample. This allows surface recombination to occur and hence for the saturable absorber recovery time to be short. In this case it was measured to be approximatly 4 ps Ch.4.

The other major advantage of a surface QW over more traditional techniques to achieve a fast recovery time for a slow saturable absorber is in the non-saturable losses. For a surface QW SESAM the non-saturable losses remain small, at 0.2%. For a more traditional SESAM, such as one with a low temperature MBE grown QW, the non-saturable losses would be in the order of 1-1.5% for a similar recovery time. Whilst this still appears a small loss, it has major implications for VECSELs, where typically there is only a few percent gain available.

To design a SESAM with the correct characteristics for achieving shorter pulses than the 500 fs pulses currently achieved, the intensity on the QW needs to be carefully controlled. This can be achieved by moving the QW away from the surface, to the desired position in the standing wave pattern in the micro-cavity for the required wavelength. However doing this means that a different method for obtaining a fast absorber recovery time will need to be employed. In the work of A. Aschwanden [66] it was demonstrated

that the recovery time of an ordinary InGaAs QW similar to the ones we use was in fact approximately 150 ps whereas that for a LT InGaAs QW was 100 ps, showing that the carrier lifetime was inherently short for an InGaAs quantum well, even when grown under ideal growth conditions. This shows a potential method for producing a fast absorber recovery time with very low fixed losses, whilst being able to accurately control its position in the E-field standing wave pattern. It is, however, not clear whether a carrier recovery time in the order of 100 ps would be fast enough to produce clean mode-locking like that reported in this work.

A simple way to control the ΔR of the SESAM would be to change the micro-cavity thickness. In the current design it was chosen to be $0.68\lambda/4$, which in theory should have given a ΔR of about 0.7%. This value could be increased further by reducing the thickness of the microcavity, although this would mean that the e-field at the surface would stop being near zero and therefore interface scattering, and potentially surface damage may become a problem.

Another way to increase the ΔR of the SESAM in the bandedge regime without having to move the quantum well from the surface would be to include two coupled quantum wells into the SESAM structure. This may be the next most straightforward design to use to attempt to further reduce the pulse duration, although the second quantum well would not benefit from the surface recombination effect so may have a much slower recovery time compared to the surface quantum well. It would also be important to fully understand the implications of the quantum wells being coupled to the transition energies of the quantum wells.

It is also important to consider the bandwidth of the ac-Stark effect, which has been measured at low temperature to cover approximately 3 nm [61]. The exact importance of the different contributions of the saturable absorption in this SESAM are not well understood and so it is hard to say whether the bandwidth of the ac-Stark effect will cause a limit to the pulse length which can be generated using this method.

Pump-probe experiments with a tuneable femtosecond laser would reveal much more information on this, allowing the quantitative values to be placed on the strength of the ac-Stark effect, the resonant saturable absorber effect and their interplay. This

would be obtained by performing pump-probe measurements on the SESAM, tuning the wavelength from resonant at 1030 nm, to band edge up to 1045 nm.

Once the limiting factors have been removed by increasing the strength and bandwidth of the mode coupling mechanism and the gain bandwidth is limiting the pulse duration of the pulses from a mode locked VECSEL it is possible to produce gain structures with even broader gain bandwidths by stepping the design wavelength of the quantum wells in the gain sample over a range of wavelengths. This has so far not been attempted for application in a mode locked VECSEL due to factors other than the gain bandwidth of the laser limiting the shortest achievable pulse. This has been demonstrated previously in a quantum well laser used as a tuneable mode locked semiconductor laser, with a large tuning range. A tuning range of 61 nm has been demonstrated by this process in [67] and [68]. Stepped quantum wells have also been demonstrated with a mode locked semiconductor laser where femtosecond pulses where achieved through external compression [14]. This method of increasing the available bandwidth would however further reduce the gain for each individual wavelength, as the total gain of the VECSEL would be spread over a broader range of wavelengths.

Chapter 7

Mode-locking laser noise characteristics: Timing jitter

7.1 Introduction to timing jitter

All oscillators, whether rf-electrical or mode locked lasers, have some inherent noise. This can be split up into two major parts: timing jitter and amplitude jitter.

Amplitude jitter is a measure of the variation of the amplitude of the individual pulses in the pulse train. This is of importance in some applications, for example in excitation experiments where a uniform excitation needs to be achieved from each pulse for pump-probe measurements.

Timing jitter is an uncertainty in the position in time at which each successive pulse in the pulse train arrives. Timing jitter is often seen as a more important measure of laser stability. Timing jitter is important for applications such as telecommunications, optical clocking and D-A converting.

Current state of the art systems used for telecoms are being based on harmonically mode locked fibre lasers [13]. Much success has been achieved in reducing the timing jitter of these lasers to the low fs range, although to achieve this complicated cavity designs are needed, along with a large range of control electronics [69].

Harmonically mode locked fibre lasers can achieve high repetition rates in the order of 10GHz or higher, but to achieve this they are locked on a high harmonic of the fundamental repetition frequency of the laser, which is inherently relatively low due to the lengths of fibre needed to produce stable mode locked lasers and high enough output powers. The harmonically mode locked lasers also require an active, or hybrid, mode locking mechanism to force the laser to stabilise on a particular harmonic of the fundamental repetition frequency.

When a laser is harmonically mode locked the noise spectrum becomes more complicated than a fundamentally mode locked laser. Noise spikes are seen at intervals in the noise spectrum relating to the different harmonics of the laser. This type of noise is called supermode noise. An example of a noise spectrum showing supermode noise is shown in Figure 7.1 [70].

Much work has been done to suppress supermode noise and in fact supermode suppression in harmonically mode locked fibre lasers and in semiconductor optical amplifier based lasers has been demonstrated as a very effective process. However the technology needed for supermode suppression greatly increases the complexity of the laser cavity. Figure 7.2 shows a typical semiconductor optical amplifier based laser cavity designed for low noise operation [70].

Another problem associated with harmonically mode locked fibre lasers is that of pulse drop-out. This is where pulses are missed out of the pulse train due to instabilities in laser cavity length and other factors which cause the mode-locking to switch from one harmonic of the fundamental repetition frequency to another. Pulse drop-out is very hard to combat, and complicated stabilisation and control schemes are needed.

Lasers which are mode locked at the fundamental repetition frequency see fewer of these problems in that there is no supermode noise in a fundamentally mode locked laser and when the laser is operating at a high fundamental repetition rate the laser cavity length is short, meaning that it is easier to isolate from mechanical vibrations, thermal changes and other destabilising environmental effects. A fundamentally mode locked high repetition rate laser would therefore provide a simple, compact and cheap

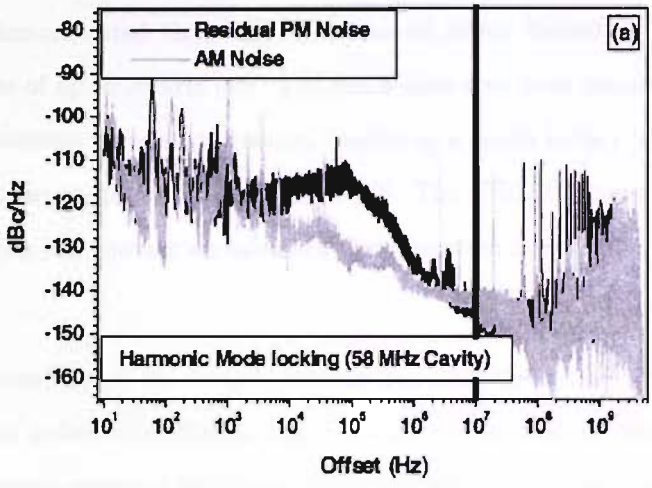

FIGURE 7.1: A noise single sideband measured at the output of a semiconductor optical amplifier based mode locked laser. This spectrum shows supermode noise in the residual PM noise, which is due to it being harmonically mode locked. The supermode noise is seen as high amplitude spikes in the noise spectrum, at high offset frequencies.(after [70])

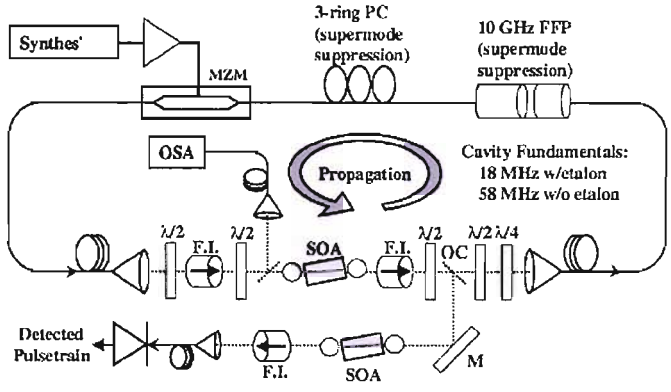

FIGURE 7.2: Diagram of the low noise mode locked semiconductor optical amplifier laser for which the above noise spectrum had been charcterised. It is clear that a harmonically mode locked laser of this type leads to a complex cavity, containig many components. SOA = semiconductor optical amplifier, F.I. = faraday isolator, FFP = fibre Fabry-Perot, PC = polarisation controller, MZM = Mach-Zehnder modulator, OC = output coupler. (after [70])

alternative to fibre lasers and the associated electronics needed for low noise harmonic mode-locking.

It has been demonstrated that VECSELs can be mode locked at high fundamental repetition rates of up to 30GHz [42]. VECSELs have also been demonstrated operating over several different wavelength ranges, including a mode locked VECSEL operating at the telecoms wavelength range of 1.5μm [40]. The VECSEL has also been identified theoretically as a laser having an inherently low quantum noise limit to the timing jitter [71].

The work reported below has focused on characterising the timing jitter and amplitude noise of a mode locked VECSEL for the first time and to lock the repetition rate of the laser to an external electrical oscillator, to actively stabilise the laser and actively reduce the laser noise.

7.2 Theory of laser noise and its characterisation

In a jitter free laser that is fundamentally mode locked, the pulse train consists of a continuous train of identical pulses, all with identical spacing between them, which is set by the cavity length, and hence intra-cavity pulse roundtrip time. This pulse train has a characteristic repetition frequency, F_{rep} which is related to the roundtrip time, T as $F_{rep} = 1/T$. When timing jitter is introduced into the laser model the pulse position becomes less precise.

If a small number of successive pulses are looked at in the pulse train, the separation in time between the successive pulses would be nearly identical, with only small changes being seen. The noise has a small influence, pushing the pulses closer together or further apart in a random fashion. The difference in the roundtrip time can be described as $T + \Delta$t, where Δt undergoes a random walk around zero. This can be seen in Figure 7.3 below which shows a laser pulse train with no timing jitter and a laser pulse train with timing jitter.

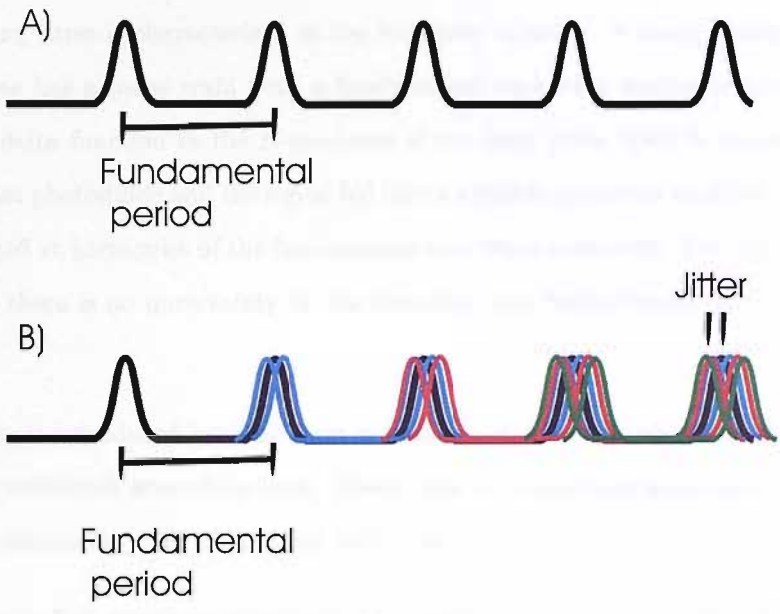

FIGURE 7.3: A representative diagram of a noise free pulse train a) and a pulse train showing timing jitter, b). This shows that the timing variation pulse to pulse is very small, but this leads to a cumalative spread, when averaged over many pulses, in the known pulse position in time because the small timing shift pulse to pulse takes a random walk and hence a statistical spread of the pulse position in time is seen.

The random walk of Δt around zero can be physically caused by many different mechanisms. The strongest mechanisms for low repetition rate lasers are mechanical movement, due to vibrations and thermal fluctuations changing the laser cavity length. As the repetition rate is increased these mechanical and thermal limitations are simpler to engineer out of the system and their relative impact is much smaller.

However there are many more subtle processes which can create noise in a mode locked laser. In the most fundamental case there is a quantum noise contribution. There is an amplitude noise to timing jitter coupling term, and this can be understood as changes in the pulse energy cause changes in the dynamics of the gain saturation and more importantly in the dynamics of the SESAM saturation. Pump power fluctuations also have an impact on the amplitude noise and timing jitter of the laser system as this causes changes in the carrier levels in the gain structure and changes in the gain dynamics.

A complete description of the different possible noise contributions and their influences on laser noise can be found in [72] and [71].

Laser timing jitter is characterised in the frequency domain. A mode locked laser that is noise free has a pulse train with a fundamental repetition frequency which can be seen as a delta function in the rf-spectrum if the laser pulse train is detected with a suitably fast photodiode and the signal fed into a suitable spectrum analyser. Spikes are also detected at harmonics of the fundamental repetition frequency. The delta functions show that there is no uncertainty in the frequency and hence timing of the successive pulses.

When noise is introduced into the laser system the rf spectrum shows a delta function with noise sidebands around its base. These noise sidebands are made up of the timing jitter and amplitude jitter of the laser pulse train.

Von der Linde first suggested a method of completely characterising the noise of a mode locked laser from a truncated frequency spectrum [73]. A mode locked laser shows spikes in the rf spectrum as these are the modes in frequency that are locked together in phase, which constructively add up at the output coupler to produce the pulsed laser output [73].

In a typical mode locked laser hundreds of modes are locked together. It is therefore possible to detect only a number of these using an rf spectrum analyser. The timing jitter and amplitude noise can however be extracted from the truncated spectrum because the timing jitter and the amplitude noise can be independently identified due to their dependence on harmonic number. Eq.Equation 7.1 shows the total noise of a mode locked laser [73]. It can be seen that the rf spectrum consists of four different components shown below:

- The ideal noise free delta functions
- $S_E(f)$ The amplitude jitter, which is independent of harmonic number
- $S_{TE}(f)$ An amplitude to timing jitter coupling term, which scales linearly with harmonic number
- $S_J(f)$ The timing jitter component, which scales with harmonic number squared

$$S_n(f) = S_E(f) + (2\pi n f_0) S_{TE}(f) + (2\pi n f_0)^2 S_J(f), \tag{7.1}$$

where $S_n(f)$ is the sideband noise spectral density function, $S_E(f)$ is the pulse energy noise spectral density function, $S_{TE}(f)$ is the timing-to-amplitude noise coupling spectral density, $S_J(f)$ is the jitter spectral density function, f is the carrier offset frequency, f_0 is the cavity repetition rate, and n is the harmonic number [74].

A schematic diagram of an rf spectrum is shown below in Figure 7.4 to illustrate this, disregarding the contribution of the timing to amplitude noise coupling term. The amplitude noise can be clearly seen to remain constant regardless of harmonic number whereas the timing jitter scales as harmonic number squared. It is also interesting to note that the majority of timing jitter noise is limited to only a relatively small range of carrier offset frequencies around the noise free delta function. This is characteristic of most lasers, particularly those where relatively slow effects dominate the timing noise, such as vibrations and thermal effects. In reality there are often noise contributions at higher offset frequencies, although these will usually be negligible compared to the low offset frequency components.

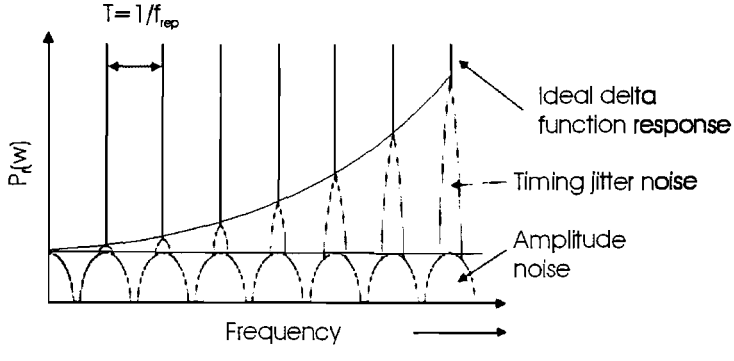

FIGURE 7.4: Diagram of the theoretical rf spectrum of the laser, showing the ideal noise free output of only delta functions at multiples of the fundamental repetition frequency, amplitude noise, which is independent of harmonic number, and timing jitter, which increases quadratically with harmonic number.

The von der Linde method of laser noise characterisation described above is the most straightforward method but it has several limitations. The first of these is that the fast photodiode and rf spectrum analyser have to have a large enough bandwidth to allow the noise around several harmonics of the fundamental repetition frequency to be

characterised. This becomes a problem at repetition frequencies in the order of 10GHz. A second limitation is also the resolution limits of the rf spectrum analyser. Mixers and internal electrical oscillators are used to analyse the signal and the noise of these can often be comparable to that of the laser that is being measured, particularly at higher frequencies.

There are therefore several other methods which have been developed to characterise the noise of a mode locked laser which can be used for analysing higher repetition rate lasers. The first of these is the phase noise method, where the laser signal is mixed with the signal from a lower noise electrical oscillator, whilst the phase between the two signals is maintained at 90 degrees [75]. This ensures that only the timing jitter component of the noise is seen and amplitude noise is rejected.

This is a popular method to use for actively mode locked lasers as the noise of the driving oscillator is removed, leaving only the timing jitter due to the laser. This method does however require a very quiet electrical oscillator, which must be synchronised to the laser pulse train through active stabilisation or through active mode-locking.

The third and most recently demonstrated method for measuring the laser noise is the Paschotta method. This requires two identical lasers, operating at nearly identical repetition frequencies, which are then mixed with the signal from an electrical oscillator at a similar, but not necessarily identical frequency to the laser repetition frequencies [76]. This then leaves a beat signal from which the absolute timing jitter of the lasers can be extracted, without having the limitations of needing a quieter electrical oscillator than the laser.

This method can be used with passively mode locked lasers as well as actively mode locked ones, which increases its applicability, although two identical lasers are needed, and the noise characteristics of each laser is assumed to be identical and to contribute equally to the total measured jitter.

7.3 Active stabilisation of a passively mode locked VECSEL

Passively mode locked lasers produce a pulse train which has a period equal to the laser cavity round trip time. Passively mode locked lasers are seen as a problem for some applications such as telecoms where a well defined electrical pulse source synchronous to the mode locked laser aids the simplicity of the control and modulation processes.

An external electrical oscillator can be synchronised to a mode locked laser through a relatively simple proportional, integral, differential (P-I-D) controller. On the other hand if the electrical oscillator available has lower timing jitter than the mode locked laser, the electrical oscillators jitter characteristics can be transferred onto the mode locked laser over a certain bandwidth by locking the laser repetition rate to that of the electrical oscillator. This can be done by controlling the cavity length and hence the round trip time of the laser using a fast mechanical stage, on which one of the laser mirrors is mounted.

In this work the laser was actively stabilised to a quieter electrical oscillator using a feedback loop and a piezoelectric stage to move the cavity output coupler, and hence change the cavity length. The bandwidth over which the noise characteristics are transferred from the electrical oscillator to the laser is set by the response bandwidth of the locking electronics and of the piezoelectric stage.

Active stabilisation has been shown to be an effective method for reducing the timing jitter of many types of mode locked lasers such as [74] and [69].

Experimentally the output coupler was mounted on a piezoelectric controlled positioning stage, which had a bandwidth of 10 kHz. This externally controlled length adjustment was used to actively stabilise the cavity length by locking the laser repetition rate to an electrical oscillator. The laser stabilisation scheme is shown schematically in Figure 7.5.

A portion of the laser output is detected by a photodiode, and the photodiode current is mixed with the signal from an HP 8656B reference oscillator to produce a beat signal between the electrical oscillator and the laser pulse train. A low pass filter ensured that

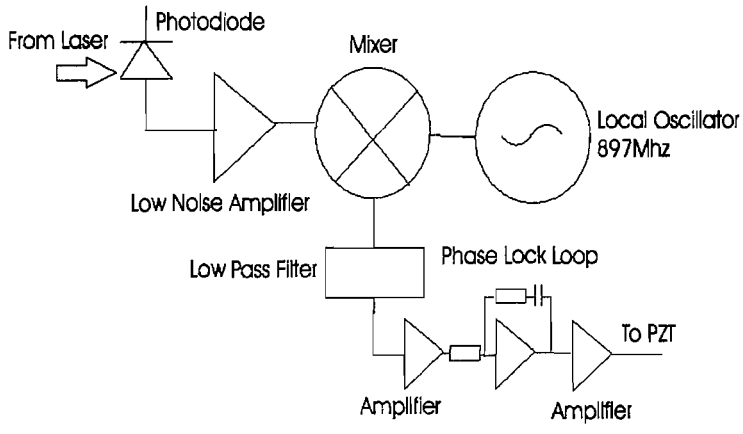

FIGURE 7.5: A schematic of the component parts of the active stabalisation feedback locking mechanism.

only frequency components up to 5 MHz were passed to the phase locked loop, which continuously adjusted the control voltage applied to the PZT driver, forcing the laser to lock to the external oscillator.

7.4 Noise characterisation of a passively mode locked VECSEL and an actively stabilised passively mode locked VECSEL

In this work we report the first characterisation of the laser noise of a free-running passively mode locked VECSEL.

For this first demonstration, it was convenient to design a cavity with a fundamental pulse repetition frequency of 897 MHz. This allowed us to use the von der Linde method for characterising fluctuations in pulse energy and pulse timing error [73], measuring noise sidebands of peaks in the rf spectrum of the laser output up to the 20th harmonic of the fundamental repetition rate, as well as to utilise an available rf electrical oscillator.

The laser was based around a Z-shaped laser cavity is shown in Figure 7.6. This cavity has a larger stability range compared to the laser cavity design that is used for most mode-locking work described in this thesis. This is useful as the output coupler is mounted on a piezoelectric stage and hence moves. The larger stability range of this

cavity ensures that the mode sizes on the gain and SESAM do not change significantly across the movement range of the PZT.

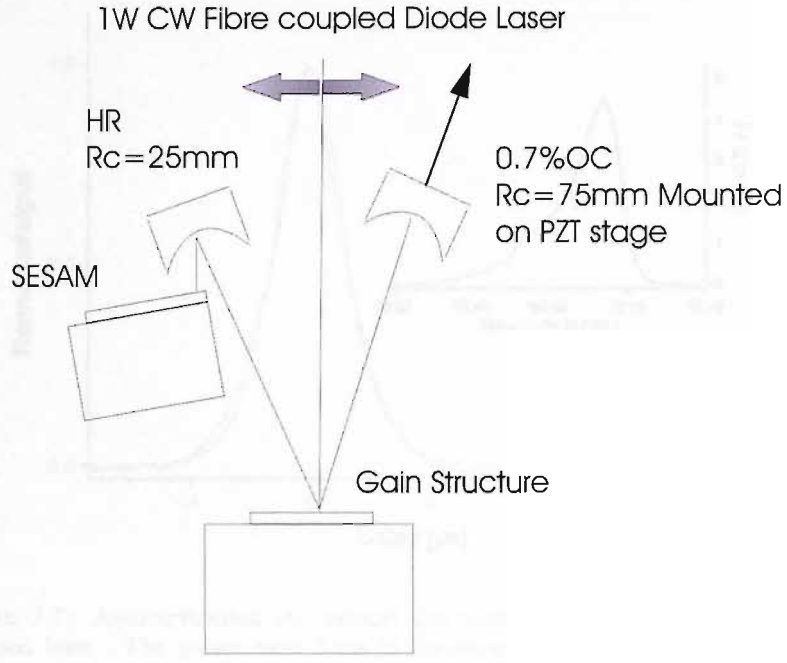

FIGURE 7.6: A schematic diagram of the laser cavity used for noise characterisation and for active stabalisation. The cavity consists of a 75mm RC focussing output coupler with 0.7% transmission and a 25 mm RC focussing mirror. The VECSEL gain sample is QT1544 and the SESAM used for locking is QT1627. The mode radius on the gain is 65μm and 13μm on the SESAM. The laser had an average output power of 40mW and produced 2.3ps pulses at a repetition rate of 897MHz.

The laser cavity design here also forces a particularly small laser mode waist onto the SESAM, which is necessary to produce stable picosecond pulses. The waist on the gain was 65μm and 13μm on the SESAM, leading to a pulse fluance approximately 25 times larger on the SESAM than on the gain. This higher than normal ratio between the mode areas means that more self phase modulation is induced in the SESAM, stopping shorter femtosecond pulses from being produced and instead producing stable chirped picosecond pulses.

The gain structure used is QT1544, which is described in 2 and the SESAM structure used is a surface quantum well SESAM as described in 4.

The laser produced an average output power of 40mW, in 2.3ps pulses with an optical spectrum centred at 1043nm. The optical spectrum had a width of 1.46nm FWHM and was slightly asymmetric with a tail on the short wavelength side. The pulses were

chirped and were approximately 3 Fourier limited. Graphs of the pulse autocorrelation and optical spectrum are shown below in Figure 7.7

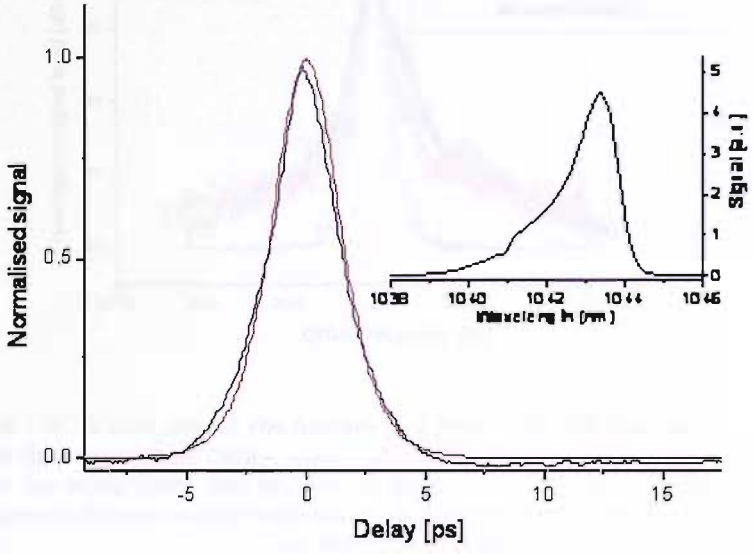

FIGURE 7.7: Autocorrelation and optical spectrum of the pulses produced by the stabilised laser. The pulses were 2.3ps in duration and near $sech^2$ in shape. The optical spectrum has a width of 1.46nm FWHM and the pulses are approximately 3 Fourier limited.

The effect of mechanical stability can clearly be seen in Figure 7.8, where the noise of the laser, at one resolution scan around the laser repetition frequency, is compared to that of the same cavity once the fibre on the fibre coupled pump laser was physically fixed in a set position and the pump launch optics stabilised. Finally a foam box was placed around the laser to reduce vibrations from air flows and to thermally isolate the laser from the environment.

The importance of simple engineering steps to reduce the noise of a laser can clearly be seen in this example, where thermal and environmental isolation along with pump stabilisation reduces the noise seen in this example to near the noise floor of the detector and spectrum analyser at this frequency resolution scan.

The noise characteristics of the laser were measured using an InGaAs photodiode (New Focus 1414) with a bandwidth of 25 GHz, and analysed by an Advantest R3273 rf spectrum analyser with a bandwidth of 26 GHz. We characterised noise sidebands on

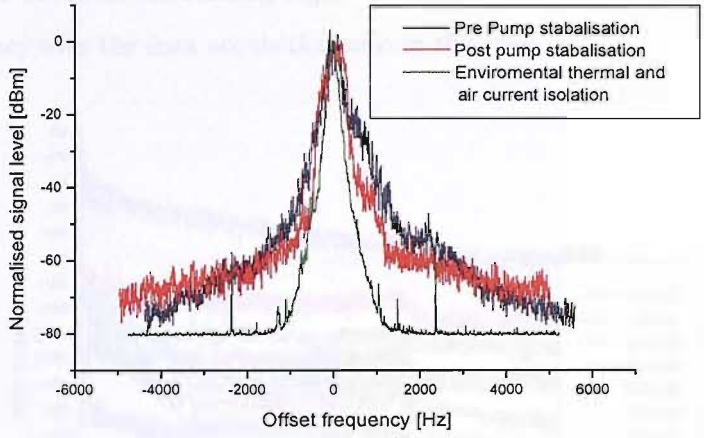

FIGURE 7.8: A scan around the fundamental laser repetition frequency, showing the noise of the original laser cavity (black line), the reduction of noise by reducing movement of the pump diode fibre and launch optics (red line), and by isolating the laser from thermal changes and air currents in the room using insulating foam to surround the laser (green line).

the 0th, 1st, 2nd, 3rd, 4th, 5th, 6th, 8th, 11th, 14th, 15th and 20th harmonics of the laser repetition frequency for the actively stabilised laser as shown in Figure 7.9.

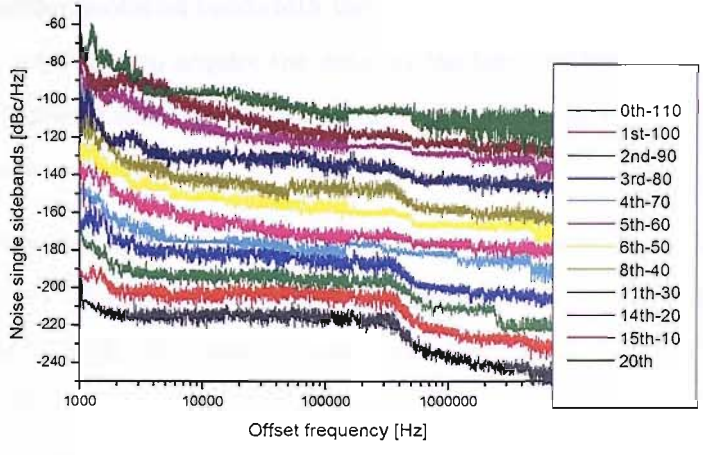

FIGURE 7.9: A graph showing the single sideband noise of all the harmonics used for the characterisation of the actively stabilised VECSEL. The data is offset by 10dB per harmonic with the fundamental harmonic being at the experimentally measured level.

The noise was also characterised for the same laser, without the active stabilisation operating. In this case the 0th, 1st, 2nd, 3rd, 4th, 5th, 6th and 8th harmonic were characterised and these measurements are shown in Figure 7.10. It was not possible

to characterise the noise surrounding higher harmonics than the 8th due to the drift in centre frequency over the data acquisition time in this case.

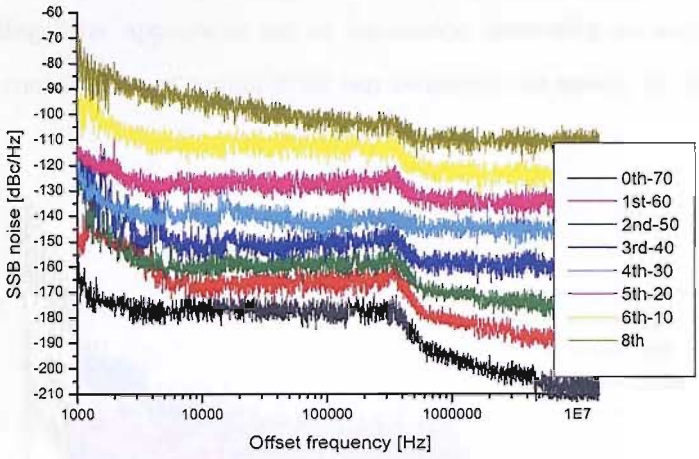

FIGURE 7.10: A graph showing the single sideband noise of all the harmonics used for the characterisation of the unstabilised VECSEL. The data is offset by 10dB per harmonic with the fundamental harmonic being at the experimentally measured level.

Each noise sideband was acquired as a composite of nine different frequency span scans, with corresponding resolution bandwidth varying from 100 Hz to 100 kHz. This is done to reduce the total time to acquire the data, as the high resolution scans are slow to acquire. The increased resolution is also not necessary as one looks at increasing carrier offset frequencies.

The noise level was normalised against carrier power and bandwidth resolution and expressed in units of dBc/Hz. The sidebands were measured in the carrier offset frequency range 1 kHz to 15 MHz. The detector noise floor is reached at about 15 MHz; below 1 kHz the noise of the electronic oscillator that we used is roughly comparable to that of the free running laser.

In an ideal case the laser noise is typically measured from an offset of 10Hz upwards. A majority of the timing jitter is located in these low offset frequencies, however for these first measurements the noise of the electrical oscillator available was too large to record a reduction in the noise, and when the laser was passively mode locked with no active stabilisation, the carrier frequency had a tendency to drift during the data acquisition period for these low offset frequencies.

Figure 7.11 shows measured noise single sidebands of the 0th, 1st and 20th harmonics for the actively stabilised laser. From these it is possible to distinguish different contributions to the laser noise. The 0th harmonic, centred around DC, shows only amplitude noise; the timing jitter appears in higher harmonics, increasing as harmonic number squared. The contribution of timing jitter can be seen to lie mainly in the 1 kHz to 30 kHz band.

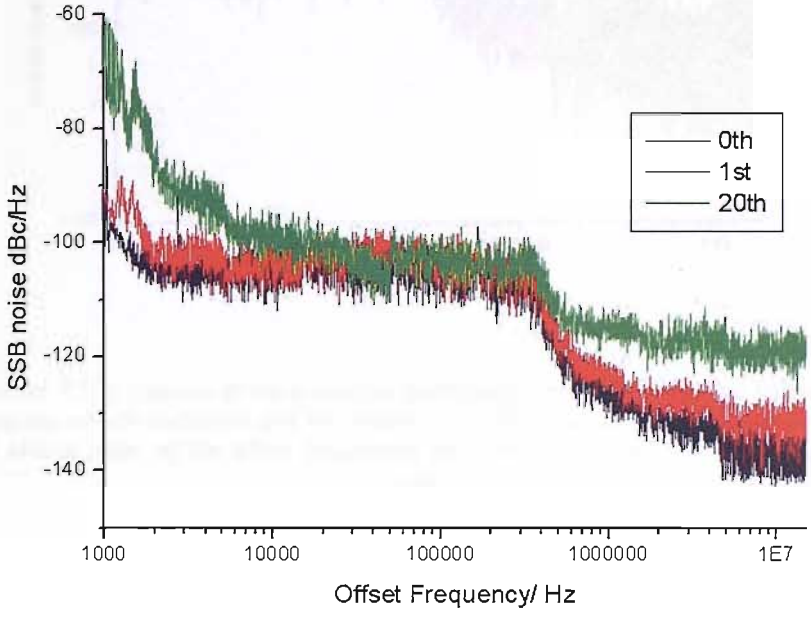

FIGURE 7.11: A graph showing the single side band noise measured for the 0th, 1st and 20th harmonics for the actively stabilised VECSEL. Timing jitter and amplitude jitter can be differentiated between as the timing jitter scale with harmonic number squared. In this case it can clearly be seen by comparing the noise measured around the different harmonics.

Figure 7.12 shows the noise sideband for the 3rd harmonic for the passive laser and the actively stabilised laser. In this case it can be seen that the noise in the low offset range has been reduced for the actively stabilised laser. The reduction in noise at lower offset frequencies is due to the reduction in timing jitter as expected.

The noise sidebands are related to the amplitude noise and timing jitter by Equation 7.1. To obtain values for the RMS jitter, the experimentally measured sidebands are integrated over the measurement bandwidth, yielding the quantity

$$\int S_n(f)df = \frac{\sigma_n^2}{2} = (\frac{\sigma_E^2}{2}) + (2\pi n f_o)(\frac{C_{TE}}{2}) + (2\pi n f_o)^2(\frac{\sigma_J^2}{2}) \tag{7.2}$$

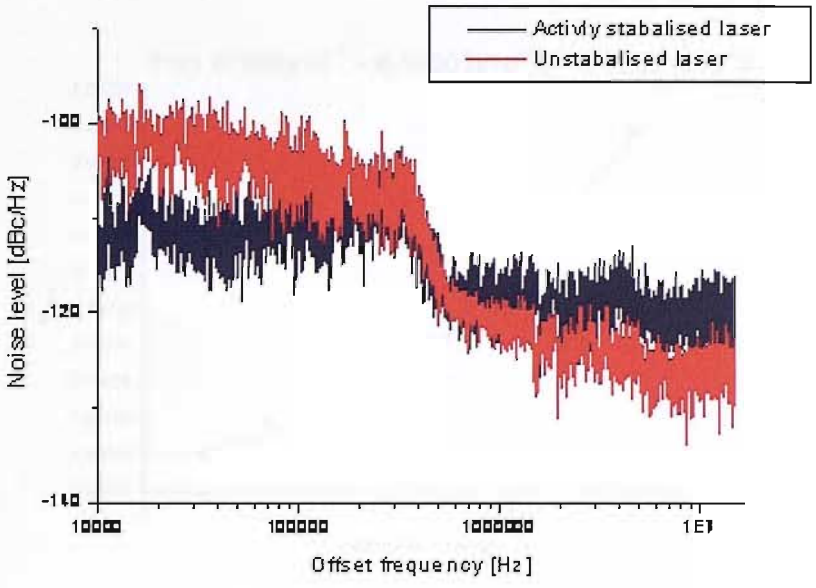

FIGURE 7.12: A graph of the measured noise single sidebands of the 3rd harmonic for both the actively stabilised and the unstabilised VECSEL. In this case it is clear that the timing jitter, at low offset frequencies has been reduced in the actively stabilised laser.

where σ_n^2 is the total noise power, σ_E is the rms normalised pulse energy fluctuation, σ_J is the rms total timing jitter and C_{TE} is the cross correlation between pulse timing jitter and normalised pulse energy fluctuations [74]. The factor of 2 occurs because we measure single sideband noise. This means that only positive offset frequencies are measured and recorded, as the negative offset sideband contains the same information.

$\sigma_n^2/2$ was fitted to a quadratic in n to extract values for σ_E, σ_J and C_{TE}. These quadratic fits are shown in Figure 7.13 for the un-stabilised laser and in Figure 7.14 for the actively stabilised laser.

We made the same measurements on the laser in a free running mode without active stabilisation. Figure 7.15 shows a comparison of the jitter noise, $S_J(f)$ for the free running laser and the actively stabilised laser. $S_J(f)$ was estimated from Equation 7.2, neglecting $S_{TE}(f)$, and averaging over all the harmonics that we measured. The figure shows that active stabilisation has reduced the jitter in the range of offset frequencies 1

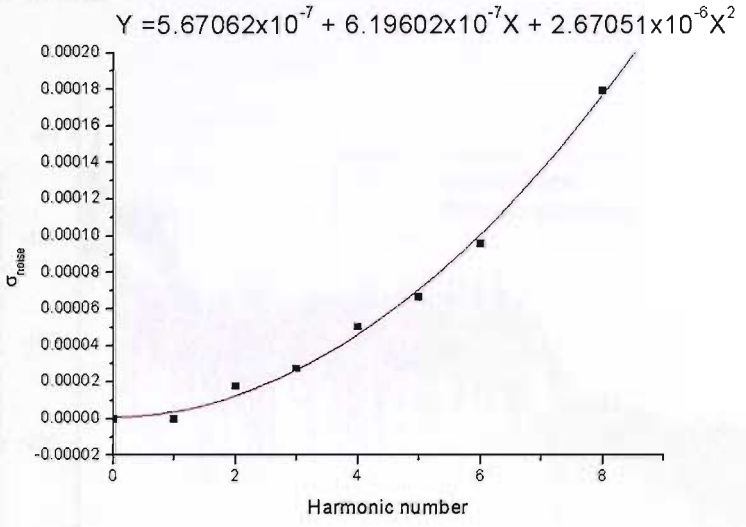

FIGURE 7.13: A graph showing the total integrated noise verses the harmonic number, along with a quadratic fit to the data for the un-stabilised laser. This fit allows the portions of timing jitter and amplitude jitter, as well as timing-to-amplitude coupling to be determined.

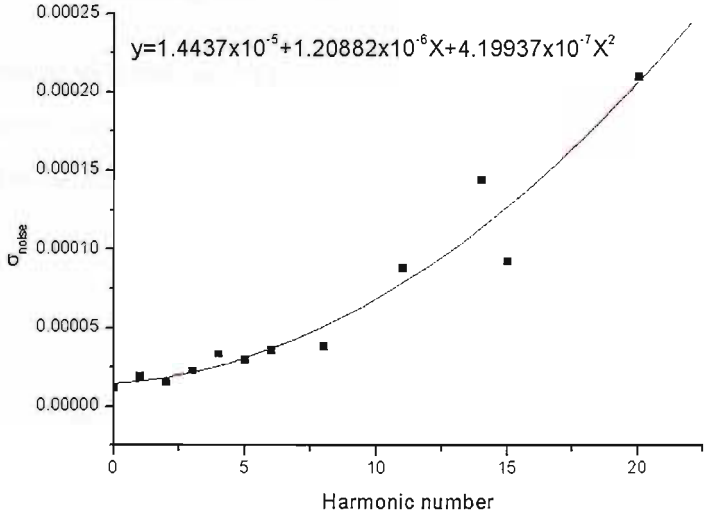

FIGURE 7.14: A graph showing the total integrated noise verses the harmonic number, along with a quadratic fit to the data for the actively stabilised laser. This fit allows the portions of timing jitter and amplitude jitter, as well as timing-to-amplitude coupling to be determined.

kHz to 5 kHz. This is consistent with the fact that the PZT and driver have a cut off frequency of 10 kHz.

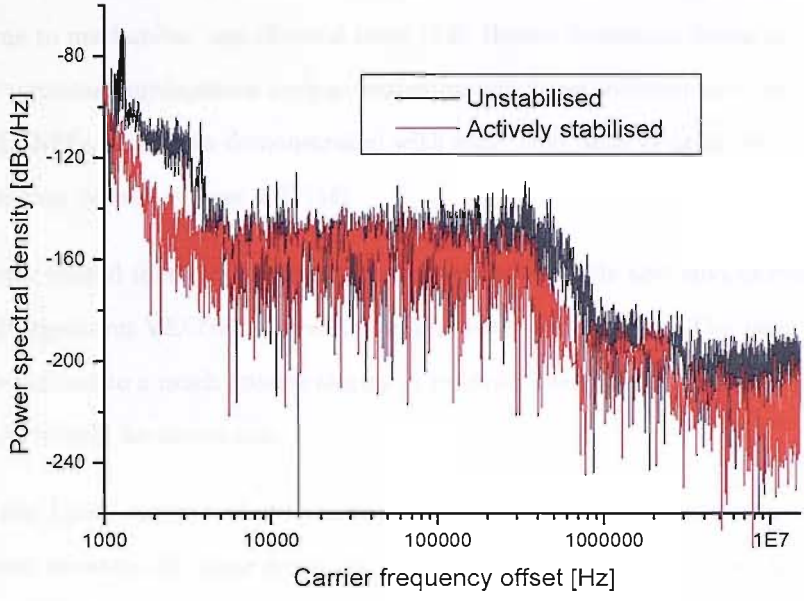

FIGURE 7.15: Final extracted timing jitter single sidebands for the passively mode-locked and actively stabilised passively mode-locked VECSEL. These sidebands were extracted by estimating the jitter using Eq.(7.2), neglecting the amplitude to timing jitter coupling term and averageing over all of the harmonics.

From analysis of the noise sideband spectra, we calculate rms timing jitter, σ_J, in the offset frequency range 1 kHz to 15 MHz of 410(30) fs for the free running laser and 160(30) fs for the actively stabilised laser. The rms amplitude noise, σ_E, over the same bandwidth, is 0.50(20)% for the actively stabilised laser and 0.30(3)% for the passive laser.

7.5 Conclusions and future work

We have characterised the timing jitter and amplitude noise of a passively mode-locked VECSEL for the first time, and shown a reduction in the timing jitter by a factor of 2.6 by locking the laser cavity to an external oscillator. These first results show that active stabilisation is possible with a VECSEL architecture, along with the demonstration that

practical steps can be taken to further reduce the noise. For example it has been shown that good environmental isolation reduces the noise of the laser greatly.

These results are taken for a relatively low repetition rate VECSEL, which is naturally more prone to mechanical and thermal noise [72]. Higher repetition lasers are also more useful for potential applications such as telecommunications and optical clocking. Mode-locked VECSELs have been demonstrated with repetition rates of up to 30GHz [42] and average output powers of over 2W [44].

Future work should focus on producing a mechanically stable and environmentally isolated high repetition VECSEL, on which to characterise the noise. The laser should be actively stabilised to a much quieter electrical reference oscillator, and reaching quantum noise limits should be aimed for.

The von der Linde method of characterising the noise of a mode locked laser does not differentiate between the noise from the mode locked laser and the noise from the RF oscillator used in the RF spectrum analyser. This leads to the von der Linde method only being useful to characterise the noise of relatively noisy lasers. The von der Linde method of noise characterisation also requires that the noise surrounding several harmonics of the laser repetition frequency be charcterised. This becomes difficult for high repetition rate lasers (eg 10GHz). Paschotta has recently developed a method to characterise the noise of two identical mode locked lasers, cancelling the effect of noise in the RF electrical oscillator [76]. This method would allow for highly accurate measurements of the laser noise to be taken at the higher repetition rates.

The VECSEL has been suggested through mathematical modelling to be a potential source for high repetition rates and extremely low noise, due to the fact that it can be fundamentally mode locked at high repetition rates with no Q-switching tendencies [42] and the low intrinsic noise limits in the VECSEL [71].

Chapter 8

Generation of THz radiation using a VECSEL

8.1 Introduction to THz generation and its applications

The spectral region of THz radiation is of great interest due to the fact that relatively little work has been performed in this region of the optical spectrum. The THz region has been shown to potentially be a very important spectral region in terms of homeland security and imaging applications as it has been shown that many items such as drugs and explosives can be uniquely identified by using a broadband THz system and observing the absorption spectra obtained from the sample. It has also been shown that DNA may also be identifiable in a similar way. A good overview of current applications for THz radiation can be found in [77]. As well as these imaging, spectroscopy and biomedical applications, there should be many more as yet untapped possibilities for applications such as coherent control and manipulation.

The terahertz region of the electromagnetic spectrum is currently receiving intense research interest. Up until the early 90s there were very few ways to generate THz radiation cheaply outside complicated transmission lines and still fewer ways to detect it. In fact, the major way to detect THz radiation before 1984 was the use of a bolometer. This is

a thermal based detector, operating at liquid hydrogen temperature. This low temperature, and hence high cost, linked with the fact that bolometers are 'square-law' detectors, measuring the intensity, but no phase information of the THz radiation, meant that it was extremely difficult to push forward with research in this spectral region.

Recently the development of semiconductor based, room-temperature generation and detection systems has lead to an explosion in the research being performed in this field. These systems are based on the Auston switch, and measure the amplitude and phase of the electric field, allowing spectral information to be obtained through Fourier transform [78]. The current state of the art systems for generating and detecting broadband coherent THz radiation are based on low temperature grown GaAs (LT-GaAs) antennas driven by femtosecond pulses from a Ti:Sapphire laser [79]. A typical THz system is shown in Figure 8.1 below [80]. In this case the THz radiation is brought to a focus, so it may be used for THz imaging or spectroscopy.

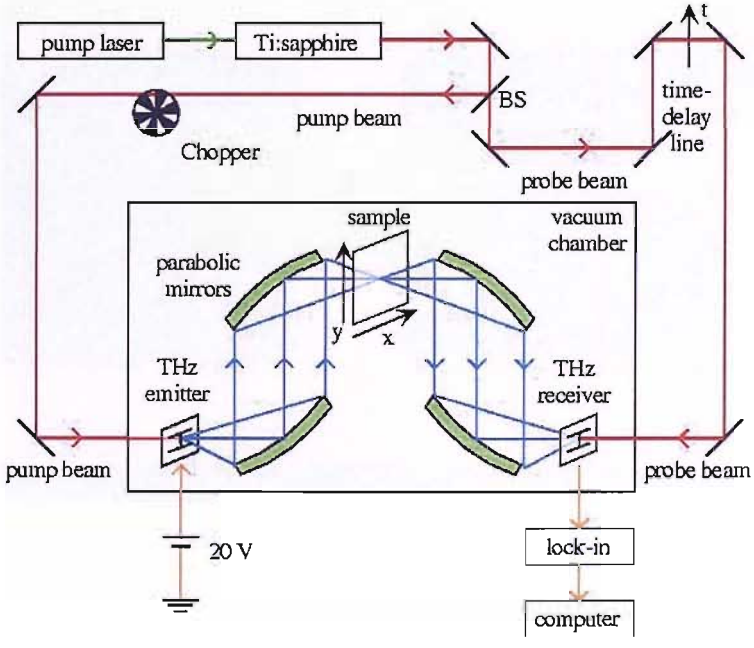

FIGURE 8.1: A schematic diagram of a typical THz time domain spectrometer. The THz radiation is collimated and focussed using four off axis parabolic mirrors [80].

THz pulses are generated and detected using the femtosecond pulses from the Ti:Sapphire laser. The laser beam is split and one arm illuminates the generation antenna while the other is passed along an optical delay line and then used to optically gate the detection

antenna. In this way, coherent detection of the THz radiation is achieved and the phase and amplitude information of the electric field of the THz pulse is plotted against optical delay time.

A typical THz generation antenna structure is shown in Figure 8.2. It consists of a LT-GaAs substrate with a metallic H structure antenna deposited on the surface [81]. The lines typically have a spacing of 50 μm, with a gap of 10 μm at the centre of the H. Electrical contacts are deposited onto these and a bias voltage of 25 V is applied (500 V/mm) across the stripes. The femtosecond laser pulses from the Ti:Sapphire laser are then focused to a 5 μm spot. The antenna is moved to ensure that the laser spot is hitting at the centre of the antenna stripe gap. The relatively large dimensions of the generation antenna ensure that they are electrically robust to the large bias voltage applied.

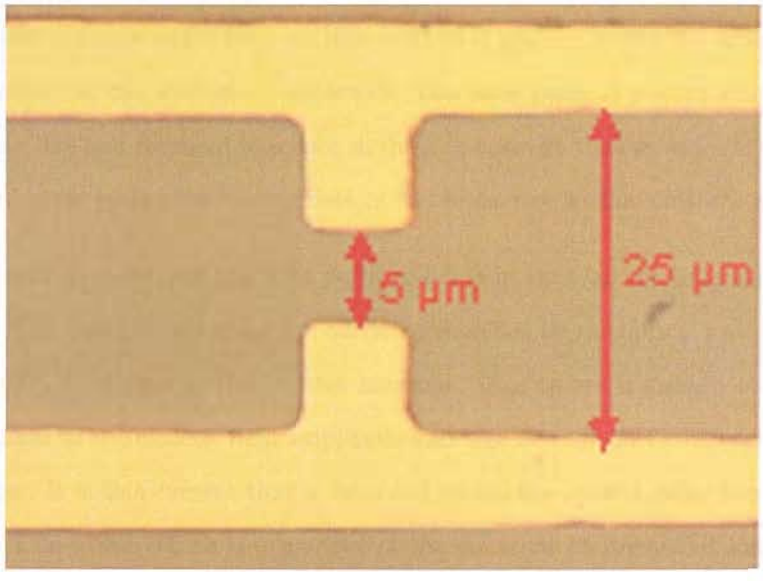

FIGURE 8.2: A typical THz antenna showing a metallic H structure deposited on an LT-GaAs substrate. In this case the antenna has a gap of 5 μm with 25 μm between the parallel lines of the H. The optical pulses are focussed onto the gap in the center of the antenna, which creates a photocurrent, with a short population recombination time [81].

THz radiation is produced by a femtosecond optical pulse hitting the semiconductor and exciting free carriers in it. The induced free carriers are driven apart by the DC voltage bias applied to the antenna structure. This movement of carriers in the emitting antenna produces the THz radiation. Free carriers are rapidly trapped due to the defects in the

semiconductor, due to the low temperature growth, causing a fast carrier recombination time. The duration of the optical pulse is important as this defines the rise time of the photocurrent, and hence the bandwidth of the THz radiation emitted.

The recovery time of the semiconductor is also important as it sets the power per unit frequency across the THz range. In other words if the recovery is too slow there are many microwave components in the spectrum, causing the fixed amount of energy available to be spread over a broader range of frequencies. This would lead to a reduction in the strength of the THz radiation generated and system sensitivity in that range.

The detection antenna is very similar to the generation antenna except a gap of typically 25 microns is used between the lines with a gap of 5 microns at the centre of the H. These reduced dimensions are used as the reduced gap dimensions increase detector sensitivity to the THz radiation. The detector antenna operates in a very similar way to the emitter antenna apart from no bias voltage is applied across the antenna and the current induced in the antenna is detected. The laser pulse is passed along a variable optical delay line and focussed to a spot in the gap between the two sides of the antenna. This optical pulse generates free carriers in the same way as the emitter antenna.

When the optical pulse and the THz pulse coincide in time on the antenna the electric field of the THz pulse drives apart the carriers generated by the optical pulse in the same way as the DC bias does in the emitter antenna. This causes a current to flow, which is proportional to the electric field amplitude and sign at that particular optically gated time window. It is this current that is recorded versus the optical delay time, producing a recorded THz pulse, which is a product of the constant photocurrent induced by the optical pulse, regardless of optical delay, and the magnitude and sign of the electric field of the THz pulse incident on the antenna.

Through Fourier transform of this pulse the THz spectrum can be generated. Figure 8.3 [79] shows a typical THz pulse that is obtained from a system driven by a Ti:Sapphire laser producing 35fs pulses. It can be seen that this method of generating THz radiation produces extremely broadband radiation up to nearly 2 THz. In Figure 8.3 absorption lines can be seen which are due to atmospheric water in the THz radiation beam path. These can be removed by placing the THz beam path inside an environment which has

been purged of water by a nitrogen purge. Further information as to the sensitivity limits and detection performance from this type of photoconductive antennae can be found in [82] and [83]

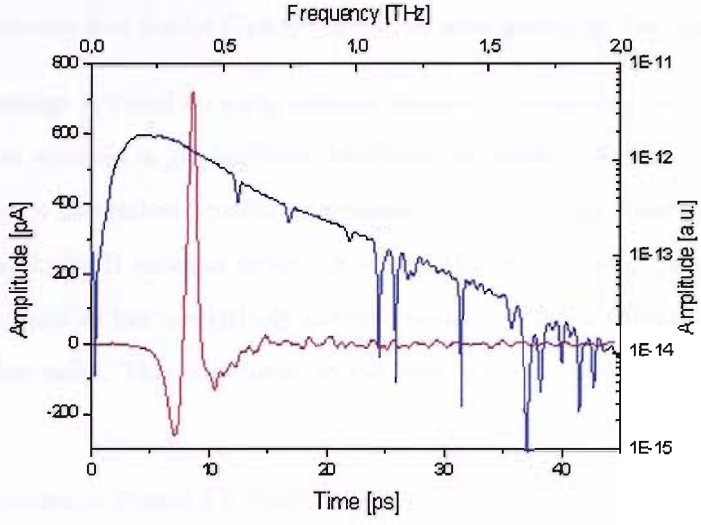

FIGURE 8.3: A single cycle THz pulse generated by a 35 fs pulse from a Ti:Sapphire driven THz system is shown, related to the bottom and left axis. The broadband THz spectrum of the pulse is extracted through Fourier transform and is shown here, related to the top and right axis [79].

8.2 THz generation using VECSELs

VECSELs offer the opportunity of a compact and relatively cheap source of 500fs pulses, which with the correct cavity design and engineering have near turn-key operation. This is an important step for the commercialisation of broadband THz imaging and spectroscopy systems. Currently Ti:Sapphire lasers are used, which are expensive and normally bulky. The advantages of a cheap compact system would have a large impact in moving THz systems from labs, with trained laser specialists, to compact turn-key systems. The main challenge for implementing VECSEL lasers in THz systems is the laser wavelength. Lt-GaAs antennae have their absorption band edge at 900nm and so these well understood antennae cannot be used. We are currently developing a mode locked VECSEL at 835 nm, for the use with Lt-GaAs antennae.

In this work we report the first generation of THz radiation using a VECSEL at 1040 nm using a Lt-GaAsSb antenna. This material has a band edge at 1100nm and so the VECSEL radiation is absorbed in this substrate. More information and a characterisation of Lt-GaAsSb can be found in [84]. This work was done in collaboration with Braunschweig Technical University and the Lt-GaAsSb antennae were grown by Damstadt University.

The antenna design is based on a log-periodic photoconductive antenna design for CW THz generation reported in [85] and have a structure as shown in Figure 8.4. This antennae design gives a theoretical broader bandwidth over which THz radiation is generated compared to a simple H antenna design. A simple H antenna has a characteristic resonant frequency and so has a relatively narrow resonant bandwidth over which efficient generation takes place. This puts limits to the bandwidth of the THz pulse that can be produced.

The antenna shown in Figure 8.4 (used in this work) effectively has many dipole pairs with different separations. The range of dipole dimensions means that each one is resonant with a different frequency starting with higher frequencies near the centre of the structure and moving to lower frequencies towards the outside of the structure. The combined bandwidth of each of these dipoles means that the antenna as a whole is resonant with a broader bandwidth of THz radiation, and produces THz radiation more efficiently over this broader range than that of a simple H design.

Another effect of this type of antenna is that the THz pulse produced is chirped due to the fact that the small separation dipoles, which are resonant with the high frequency THz radiation, are nearer the centre of the antenna structure and hence the induced free carriers reach these earlier than the lower frequency, larger dipoles located further from the centre. The polarisation of the majority of the THz radiation, produced from resonances with the shorter interdigitated arms is perpendicular to the polarisation of the low frequency components near DC which resonate with the central conductor arm.

There is a technical disadvantage to this type of antenna in that it is extremely sensitive to electrostatic discharge, due to its broadband design, and also it has a very small separation of only 2 micron between the two sides of the antenna, due to the interdigitated design. This means that the antennae are very sensitive to the bias voltage

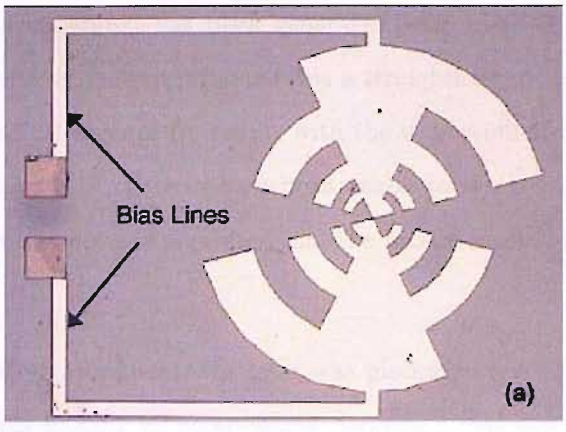

(a) A photograph of the log-periodic spiral antenna

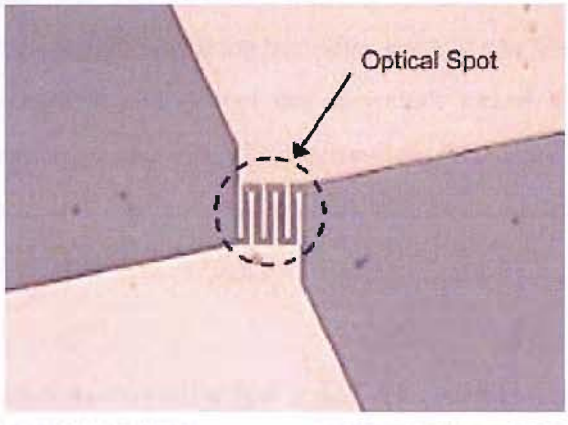

(b) A close up photo of the central section of the log-periodic antenna showing the interdigitated fingers

FIGURE 8.4: An image of the log-periodic antenna design used in the LT-GaAsSb antenna used in this work. These antennae were produced at Darmstadt University, Germany and were designed for single frequency THz generation, through the photomixing of two CW lasers at slightly different wavelengths. This image clearly shows the tiny gap between the two sides of the antenna, making them extremely sensitive and fragile [85].

that is applied to the generation antenna. A coupling of E-M radiation such as the microwaves from a mobile telephone in the presence of a large bias voltage can cause the antenna to short out, rendering it useless.

Here we report the first generation of THz radiation using a sub 500 fs 1.2G Hz mode locked VECSEL, operating at 1042 nm as the source of the short optical pulses. We have used a bolometer to detect the intensity of the radiation generated and to produce the first THz images from this system.

A strong THz radiation signal has been generated with a LT-GaAsSb antenna and detected with a bolometer, and in principle it is a straightforward matter to achieve an all-semiconductor room temperature result, with the utilisation of a second antenna in the place of the bolometer. To date we have been unable to achieve this due to the fragile nature of the antenna structures deposited and the lack of availability of the substrate material.

On another technical improvement, the laser was placed on a solid INVAR base, with locking mirror mounts holding all components, forming a compact and easily portable laser as shown in Figure 8.5. The VECSEL was still in alignment and operated correctly, producing 500fs pulses straight out of the box, after travelling to Germany, demonstrating the stability, portability and ease of use of a mode locked VECSEL. This is an important demonstration, as the VECSEL implemented in this fashion for THz generation would be aimed at a low cost, low maintenance system, usable by people with relatively little laser experience.

8.3 Experimental results for a LT-GaAsSb antenna, driven by a sub-500fs mode locked VECSEL operating with a repetition rate of 1.2 GHz and a wavelength of 1038nm

The experimental setup was as shown in Figure 8.6, with the VECSEL operating in a regime producing 50mW average power in 480 fs pulses at a repetition rate of 1.18 Ghz and a wavelength of 1042 nm. The autocorrelation and optical spectrum of the laser pulses are shown in Figure 8.7. The laser produced near transform limited pulses, which were 1.05X the Fourier limit. The Antenna was a Lt-GaAsSb substrate with an interdigitated design antenna structure. The Antenna was illuminated by the laser beam, which was focused to a spot of 5 microns.

The THz radiation passed through a silicon lens in contact with the back of the antenna, to reduce divergence. It was then collimated by an off-axis parabolic mirror, and brought to a focus by a focusing mirror. This focus defines the imaging plane, where

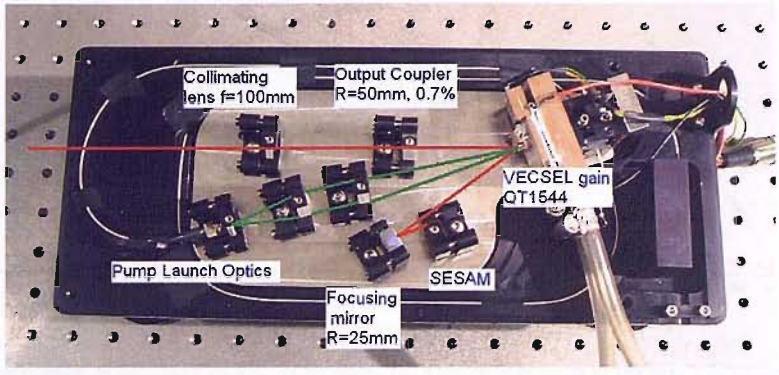

(a) A photograph of the VECSEL laser cavity, showing all of the various components. All of the mirror mounts and translation stages are lockable.

(b) A photograph of the complete laser, with its lid in place, making it stable, isolated from air movements, vibrations and tempreature variations.

FIGURE 8.5: Photographs of the 50 mW, ¡500 fs pulse VECSEL with a repetition rate of 1.2 GHz, mounted on the INVAR base, in a compact, stable, portable and robust package.

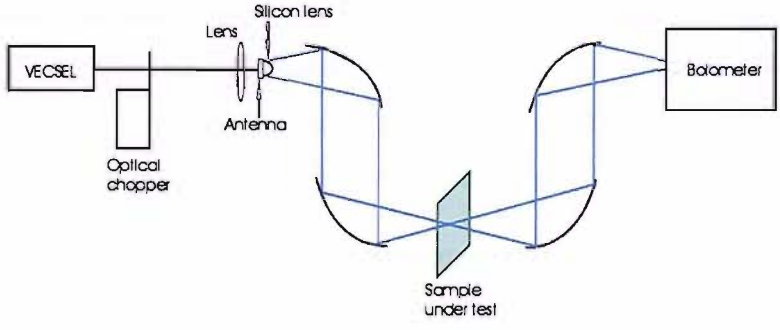

FIGURE 8.6: A schematic diagram showing the VECSEL laser cavity, which produced 50 mW average power and 480 fs pulses with a repetition rate of 1.2 GHz. This is then focused onto the LT-GaAsSb antenna and the THz radiation is focused onto a sample, before being collected and focused into the bolometer. The optical beam is mechanically chopped to allow a lock-in amplifier to be used to detect the THz signal.

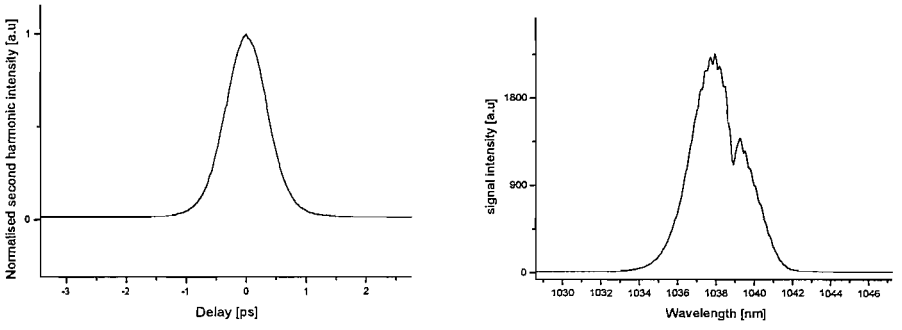

(a) Autocorrelation of the ML-VECSEL pulse train, showing $sech^2$ pulses with a FWHM width of 480 fs.

(b) Optical Spectrum of the ML-VECSEL laser output centred at 1038 nm with a FWHM width of 2.5 nm. The dip in the spectrum at 1038.5 nm is not a feature of the output spectrum and is thought to be a water absorption.

FIGURE 8.7: Graphs of the autocorrelation and optical spectrum of the VECSEL pulse train used for THz generation.

the object being imaged is placed. The THz radiation is re-collimated, and focused onto the detector by another two off axis parabolic mirrors.

The detector was a bolometer, which is a thermal sensor operating at liquid hydrogen temperatures. The bolometer detects intensity, by measuring the amount a target is heated by the THz radiation. Bolometers are sensitive over a huge wavelength range from sub mm to several microns.

The laser beam was modulated by an optical chopper at a rate of 10 Hz, and a lock-in amplifier was used at the output of the bolometer to reject noise. The image was formed by placing the object in the focus of the THz radiation and moving it in a raster scanning pattern using a computer controlled X-Y stage. The data was recorded using imaging software to build up an image of the object. This provides an image which shows the transparency of the object to the THz radiation, but provides no information regarding the specific frequency of the THz radiation that is absorbed.

Bolometers are sensitive over a very broad frequency range and therefore it is important to experimentally ensure that THz radiation was being generated and that what is detected is not just heat being emitted by the antenna due the optical energy absorbed. To ensure that THz radiation was being generated two tests were carried out. First the voltage was turned off on the antenna. Without this voultage no THz would be

generated and indeed when the voltage was switched off the detected signal from the bolometer dissapeared. As a second test the pulse duration of the VECSEL pulses was increased to several picoseconds, whilst the average power remained constant and again no signal was detected on the bolometer when it was being illuminated with longer pulses. These two experimental tests provide a lot of experimental evidence that what was generated was indeed THz radiation.

Figure 8.8 shows the first results with the THz image along with a photo of the object that was imaged. A circular hole in a metal plate was first imaged to assess the quality of the imaging system. From this the hole can be clearly seen, although it is also clear that the focus of the THz radiation is not spherical due to the asymmetry of the image. This is probably due to a slight misalignment of the THz radiation beam path.

Figure 8.9 is a THz scan of a foil F on plastic is shown along with a photo of the object. Figure 8.10 a THz image of a pig's larynx is shown along with a photograph of the sample and a THz image from a Ti:Sapphire driven system. This sample was specially prepared due to the fact that water strongly absorbs THz radiation. Therefore the sample had to be chemically dried and set in wax. The sample is also cut relatively thick (about 4 mm) compared to typical pathology samples, due to the relatively lower absorption of THz radiation by these samples compared to visible light. Details of the sample preparation can be found in [86].

The Ti:Sapphire based system was used to look at the absorption in a specific spectral range, which was possible as coherent detection could be performed as outlined above. It can be seen that there is good agreement between the image obtained by the Ti:Sapphire laser based THz system and that from the VECSEL based system.

8.4 Future work: all room temperature generation and detection

The current broadband systems all rely on expensive Ti:Sapphire laser technology, which limits their implementation into many applications due to cost and the skill required

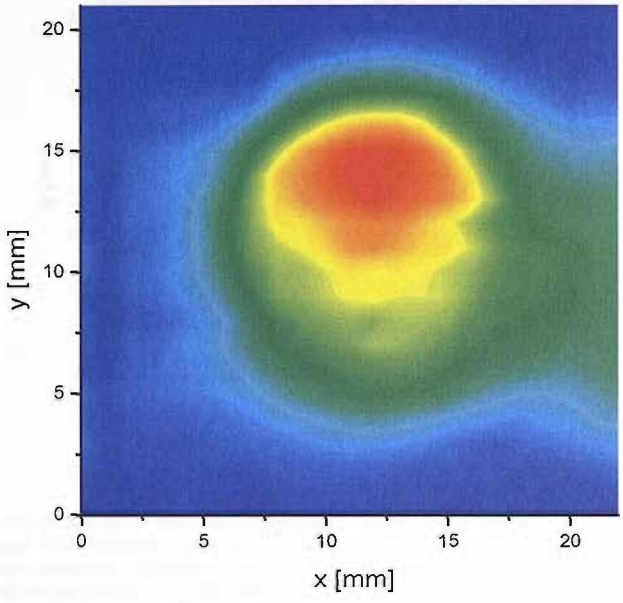

(a) THz image of a circular hole in a metal target, recorded using the ML-VECSEL to generate THz radiation with a LT-GaAsSb antenna and a bolometer to detect the radiation.

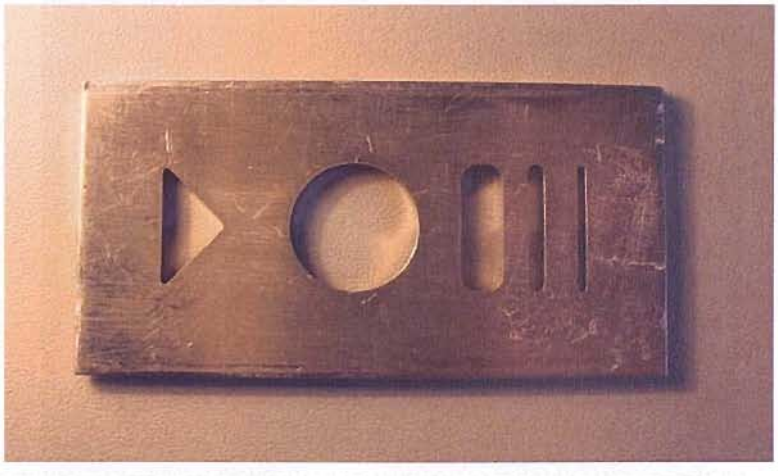

(b) A photo of the metal target showing the circular hole in the centre. Only the area directly around the hole was imaged.

FIGURE 8.8: A THz image of a circular hole in a metal target, and a photograph of the target for comparison. It can be seen that the THz image intensity is slightly assymetric, with higher intensity at the top and the right of the image. This is due to a mis-alignment of the THz beam path.

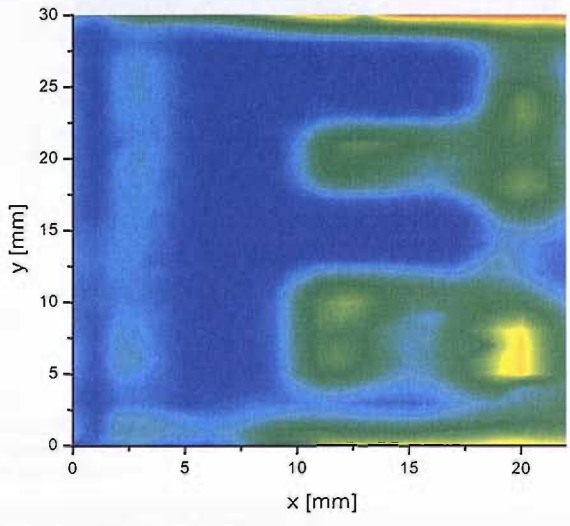

(a) THz image of a foil F mounted on plastic, recorded using the ML-VECSEL to generate THz radiation with a LT-GaAsSb antenna and a bolometer to detect the radiation. Diffraction of the THz readiation around the sample edge leads to the bright line near the bottom of the image, and the mounting clamp can be seen on the left of the image.

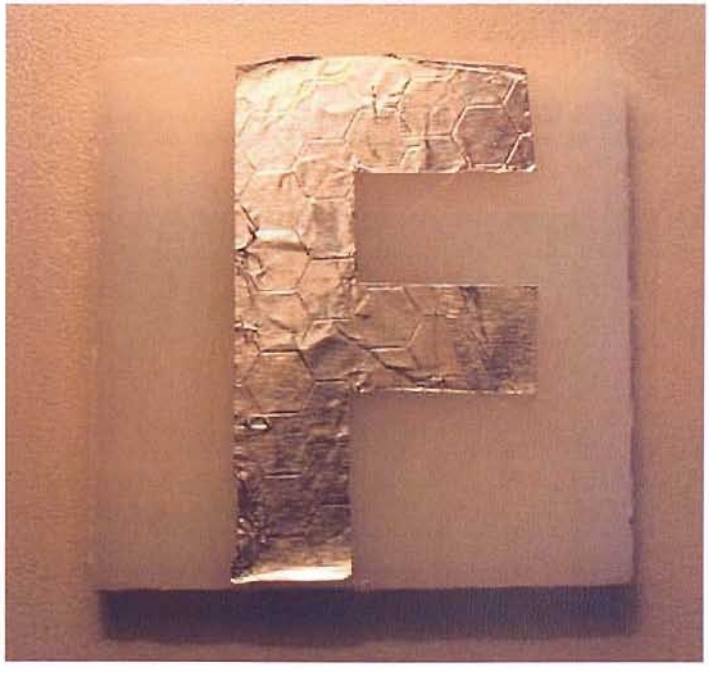

(b) A photograph of the foil F mounted on plastic that was imaged by the VECSEL THz system for comparison.

FIGURE 8.9: A THz image of a foil F mounted on plastic, and a photograph of the target for comparison. The F can clearly be seen in the THz image.

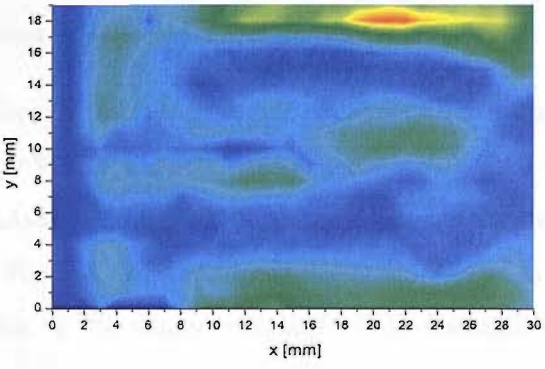

(a) THz image of a pigs larynx mounted in wax, recorded using the ML-VECSEL to generate THz radiation with a LT-GaAsSb antenna and a bolometer to detect the radiation.

(b) A photograph of the pigs larynx mounted in wax that was imaged by the VECSEL THz system and the Ti:Sapphire system for comparison.

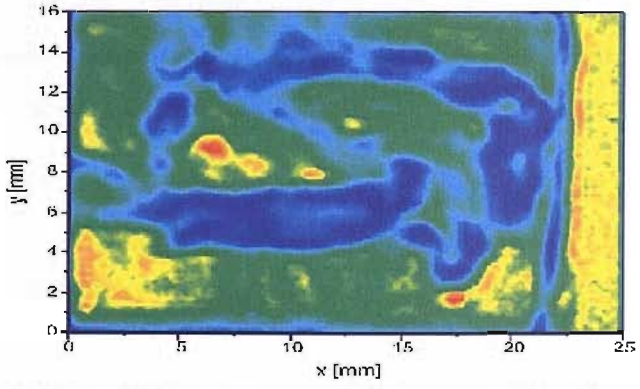

(c) THz image of a pigs larynx mounted in wax, recorded using the Ti:Sapphire laser to generate and coherently detect THz radiation using LT-GaAs antennae.

FIGURE 8.10: A THz image of a pigs larynx set in wax, recorded using the VECSEL THz system and a bolometer and also recorded using coherent dectection with two Lt-GaAs antennae and a Ti:Sapphire mode locked laser. A photograph of the target is also shown for comparison.

to operate these lasers. A cheap, compact and turn-key broadband THz source would push forwards the industrial applications of THz radiation, as well as making the THz radiation an additional tool to researchers in different fields.

It should be a straightforward matter to obtain all room temperature measurements of THz radiation using a VECSEL as the optical pulse source. All that is needed is a second working Lt-GaAsSb antenna, which can then be implemented in an identical system to that shown in Figure 8.1 for the current Ti:Sapphire based systems. Currently we have been limited due to the relative rareness of the material, as most work on THz generation has focused on Lt-GaAs based antennae for Ti:Sapphire lasers. We are also limited in that the antenna structures that we have been able to obtain are extremely complicated structures, which are prone to breaking due to their sensitivity to electrostatic discharges. We aim to perform this experiment in the near future with a pair of antennae, with simpler structure. This should yield the first all room temperature generation and detection of THz radiation using a VECSEL as the optical pulse source.

We are also working on developing a mode locked VECSEL producing sub 500fs pulses at a wavelength of 835nm, allowing the standard LT-GaAs antennae to be used, with our laser being able to act as a direct replacement of the Ti:Sapphire laser currently used, for applications where only a moderate bandwidth of THz radiation is needed.

Future work will also aim to increase output power of the VECSEL so that it could be used to drive several antennae pairs, leading to the possibility of line scanning imaging, which would greatly increase throughput.

Finally, the shortening of the laser output pulses to near their 100 fs theoretical limit would also help as a broader bandwidth of THz radiation could be obtained, which would be comparable to that from a Ti:Sapphire system. With the 480 fs pulses used currently the THz bandwidth produced is expected to be relatively moderate, in the range of 0.7 THz, due to the optical pulse being of the same order as the lifetime of the carriers in the Lt-GaAsSb and the relatively slow rise time of the free carrier density in the generation antenna compared to that from a 35 fs pulse source.

Chapter 9

Conclusions

9.1 Application based results for VECSELs

Potential practical applications have been demonstrated and worked towards in this work. The most application based work reported here is that on the generation of THz radiation with a VECSEL. The second application which progress has been made towards is the field which require stabilised low timing jitter lasers, such as optical clocking and telecommunications.

For the first time VECSELs have been used to generate THz radiation, which has been detected using a bolometer, to form the first THz images from a VECSEL driven system. Future work will focus on obtaining coherent detection as well as generation of broadband THz radiation using a VECSEL. This could make the VECSEL a very attractive laser to use with broadband systems where a modest THz bandwidth is required. The VECSEL has the opportunity to provide a cheap, stable and easy to use system for much wider application into industry.

VECSELs are being designed to operate with sub ps pulses at a wavelength of 835 nm, which would allow the well understood and easy to obtain low temperature GaAs antennas to be used, increasing ease of integration of a VECSEL based system.

The first characterisation of the timing jitter and amplitude noise of a mode locked VECSEL has been performed, as has active stabilisation of the laser cavity length,

through locking the laser repetition rate to an external oscillator. This first demonstration shows that actively stabilised passively mode locked lasers have the potential to be useful lasers in the fields of optical clocking and telecommunications, where low jitter sources are critical. The ability to power scale the VECSEL architecture, along with the already demonstrated high fundamental repetition rates available make the VECSEL potentially a very interesting source for this type of application.

Future work should focus on demonstrating an actively stabilised VECSEL at a much higher repetition rate of 10 GHz or more, as well as demonstrating further reduction of the timing jitter.

9.2 Fundamental VECSEL properties

VECSELs continue to be an interesting laser source with many potential applications. One of the most desirable advances would be to use a larger portion of the available gain bandwidth for mode-locking, to make a VECSEL producing 100fs pulses directly from the oscillator, coupled with watt level output powers. This would mean that the VECSEL would be very competitive in a whole host of ultrafast applications.

Currently a limit of 448 fs has been reached and in this work spectro-temporal measurements on a sub 500 fs VECSEL were performed to observe the spectrum evolution, and mode-locking onset times for several pulse regimes were recorded. These measurements strongly point to the optical spectrum limiting the minimum pulse duration that can currently be generated, as the mode-locking onset time increases as the pulse duration decreases.

Several potential methods have been suggested for further reducing the pulse duration. The first and possibly simplest is to redesign the SESAM structure to force the pulse to be formed sooner after CW lasing starts, when mode-locking in the ac Stark regime. The other major route that should be pursued is that of exploiting other fast saturable effects such as the Kerr effect, which is used to such great effect in Ti:Sapphire lasers. This has been attempted, using ZnSe, which has a much higher non-linear coefficient than sapphire, but to date this has not been achieved due to the losses that are imposed by

TPA on the laser by introducing pollycrystaline ZnSe. Other potential materials should be pursued such as single crystal ZnSe and also potentially polymer filled photonic crystals [58]. A Kerr lens mode locked VECSEL would be technically easier to demonstrate if the fixed losses of the cavity could be reduced, or the gain could be increased, for example by better thermal management of the active gain region.

Appendix A

Publication list

K.G. Wilcox, H.D. Foreman, J.S. Roberts, and A.C. Tropper, 'Timing jitter of 897 MHz optical pulse train from actively stabilised passively modelocked surface-emitting semiconductor laser', IEE Electronics Letters, vol. 42, no. 3, p 159-160, 2006.

A.C. Tropper, H.D. Foreman, A. Garnache, K.G. Wilcox and S.H. Hoogland, 'Vertical-external-cavity semiconductor lasers', Journal of Physics D: Applied Physics, vol. 37, pR75-R85, 2004.

H.D. Foreman, K.G. Wilcox, A.C. Tropper, P. Dupriez, A. Malinowski, J.K. Sahu, Y. Jeong, J. Nilsson, D.J. Richardson, F. Morier-Genoud, U. Keller, J.S. Roberts, 'High power femtosecond source based on passively mode locked 1050-nm VECSEL and Yb fibre power amplifier', Advanced Solid State Photonics, Lake Tahoe, Feb 2006.

K.G. Wilcox, H.D. Foreman, J.S. Roberts, and A.C. Tropper, 'Timing jitter characterisation of a 1.04μm passively mode-locked VECSEL at an actively stabilised repetition rate of 897 MHz', Advanced Solid State Photonics, Vienna, 2005.

K.G. Wilcox, H.D. Foreman, J.S. Roberts, A.C. Tropper, F. Rutz, R. Wilk, C. Jordens and M. Koch, 'All room temperature coherent generation and detection of broadband THz radiation using LT-GaAsSb antennas and a sub 500fs mode locked vertical external cavity surface emitting laser' In preparation.

Bibliography

[1] S. Hoogland. Optically pumped vertical-external-cavity semiconductor-emitting lasers, phd thesis, university of southampton., 2003.

[2] D. L. Zhou and L. J. Mawst. High-power single-mode antiresonant reflecting optical waveguide-type vertical-cavity surface-emitting lasers. *Ieee Journal of Quantum Electronics*, 38(12):1599–1606, 2002.

[3] N. Samal, S. R. Johnson, D. Ding, A. K. Samal, S. Q. Yu, and Y. H. Zhang. High-power single-mode vertical-cavity surface-emitting lasers. *Applied Physics Letters*, 87(16), 2005.

[4] M. Kuznetsov, F. Hakimi, R. Sprague, and A. Mooradian. High-power (¿0.5-w cw) diode-pumped vertical-external-cavity surface-emitting semiconductor lasers with circular tem00 beams. *Ieee Photonics Technology Letters*, 9(8):1063–1065, 1997.

[5] M. Kuznetsov, F. Hakimi, R. Sprague, and A. Mooradian. Design and characteristics of high-power (¿ 0.5-w cw) diode-pumped vertical-external-cavity surface-emitting semiconductor lasers with circular tem00 beams. *Ieee Journal of Selected Topics in Quantum Electronics*, 5(3):561–573, 1999.

[6] http://www.novalux.com.

[7] C. L. Yan, Y. Q. Ning, L. Qin, D. Cui, Y. Liu, Y. F. Sun, Z. H. Jin, H. Q. Li, G. T. Tao, C. Wang, L. J. Wang, and H. L. Jiang. High-power vertical-cavity surface-emitting laser with an extra au layer. *Ieee Photonics Technology Letters*, 17(8):1599–1601, 2005.

[8] J. L. A. Chilla, S. D. Butterworth, A. Zeitschel, J. P. Charles, M. K. Reed, and L. Spinelli. High-power optically pumped semiconductor lasers. *Solid State Lasers XIII*, Session 5332:41, 2004.

[9] S. Hoogland, S. Dhanjal, A. C. Tropper, J. S. Roberts, R. Haring, R. Paschotta, F. Morier-Genoud, and U. Keller. Passively mode-locked diode-pumped surface-emitting semiconductor laser. *Ieee Photonics Technology Letters*, 12(9):1135–1137, 2000.

[10] C. Stewen, K. Contag, M. Larionov, A. Giesen, and H. Hugel. A 1-kw cw thin disc laser. *Ieee Journal of Selected Topics in Quantum Electronics*, 6(4):650–657, 2000.

[11] K. Contag, M. Karszewski, C. Stewen, A. Giesen, and H. Hugel. Theoretical modelling and experimental investigations of the diode-pumped thin-disk yb : Yag laser. *Quantum Electronics*, 29(8):697–703, 1999.

[12] H. Le, S. Di Cecca, and A. Mooradian. Scalable high-power optically pumped gaas laser. *Applied Physics Letters*, 58:1967, 1991.

[13] H. Cao, L. R. Chen, J. Magne, and S. LaRochelle. Tunable 4x10 ghz optically modelocked semiconductor fibre laser. *Electronics Letters*, 41(13):730–732, 2005.

[14] P. J. Delfyett, L. Florez, N. Stoffel, T. Gmitter, N. Andreadakis, G. Alphnose, and W. Ceislik. 200-fs optical pulse generation and intracavity pulse evolution in a hybrid mode-locked semiconductor diode-laser/ amplifier system. *optics Letters*, 17(9):670–672, 1992.

[15] E. U. Rafailov, M. A. Cataluna, W. Sibbett, N. D. Il'inskaya, Y. M. Zadiranov, A. E. Zhukov, V. M. Ustinov, D. A. Livshits, A. R. Kovsh, and N. N. Ledentsov. High-power picosecond and femtosecond pulse generation from a two-section mode-locked quantum-dot laser. *Applied Physics Letters*, 17:081107, 2005.

[16] W. B. Jiang, M. Shimizu, R. P. Mirin, T. E. Reynolds, and J. E. Bowers. Femtosecond periodic gain vertical-cavity lasers. *Ieee Photonics Technology Letters*, 5(1):23–25, 1993.

[17] P. P. Vasilev and A. B. Sergeev. Generation of bandwidth-limited 2 ps pulses with 100 ghz repetition rate from multisegmented injection laser. *Electronic Letters*, 25:1049, 1989.

[18] D. A. Yanson, M. W. Street, S. D. McDougall, I. G. Thayne, J. H. Marsh, and E. A. Avrutin. Terahertz repetition frequencies from harmonic mode-locked monolithic compound-cavity laser diodes. *Applied Physics Letters*, 78:3571, 2001.

[19] S. H. Park, J. Kim, H. Jeon, T. Sakong, S. N. Lee, S. Chae, Y. Park, C. H. Jeong, G.Y. Yeom, and Y. H. Cho. Room-temperature gan vertical-cavity surface-emitting laser operation in an extended cavity scheme. *Applied Physics Letters*, 83(11):2121–2123, 2003.

[20] A. Ouvrard, A. Garnache, L. Cerutti, F. Genty, and D. Romanini. Single-frequency tunable sb-based vcsels emitting at 2.3 μm. *IEEE Photonics Technology Letters*, 17:2020, 2005.

[21] D. E. Spence, P. N. Kean, and W. Sibbett. 60-fsec pulse generation from a self-mode-locked ti-sapphire laser. *Optics Letters*, 16(1):42–44, 1991.

[22] V. E. Kisel, A. E. Troshin, V. G. Shcherbitsky, N. V. Kuleshov, V. N. Matrosov, T. A. Matrosova, and M. I. Kupchenko. Femtosecond pulse generation with a diode-pumped yb3+ : Yvo4 laser. *Optics Letters*, 30(10):1150–1152, 2005.

[23] E. Innerhofer, T. Sudmeyer, F. Brunner, R. Paschotta, and U. Keller. Mode-locked high-power lasers and nonlinear optics a powerful combination. *Laser Physics Letters*, 1(2):82–85, 2004.

[24] L. Krainer, R. Paschotta, S. Lecomte, M. Moser, K. J. Weingarten, and U. Keller. Compact nd : Yvo4 lasers with pulse repetition rates up to 160 ghz. *Ieee Journal of Quantum Electronics*, 38(10):1331–1338, 2002.

[25] S. Lutgen, T. Albrecht, P. Brick, W. Reill, J. Luft, and W. Spath. 8-w high-efficiency continuous-wave semiconductor disk laser at 1000 nm. *Applied Physics Letters*, 82(21):3620–3622, 2003.

[26] A. Garnache, A. C. Tropper, and V. C. Thierry-Mieg. *CLEO Technical Digest*, page 198, 2001.

[27] R. Haring, R. Paschotta, A. Aschwanden, E. Gini, F. Morier-Genoud, and U. Keller. *IEEE J.Quantum Electron*, 38:1268, 2002.

[28] J. E. Hastie, J. M. Hopkins, C. W. Jeon, S. Calvez, D. Burns, M. D. Dawson, R. Abram, E. Riis, A. I. Ferguson, W. J. Alford, T. D. Raymond, and A. A. Allerman. Microchip vertical external cavity surface emitting lasers. *Electronics Letters*, 39(18):1324–1326, 2003.

[29] S.-S. Beyertt, M. Zorn, T. Kubler, H. Wenzel andM. Weyers, A. Giesen, G. Trankle, and U. Brauch. Optical in-well pumping of a semiconductor disk laser with high optical efficiency. *IEEE Journal of Quantum Electronics*, 41(12):1439, 2005.

[30] A. J. Kemp, G. J. Valentine, J. M. Hopkins, J. E. Hastie, S. A. Smith, S. Calvez, M. D. Dawson, and D. Burns. Thermal management in vertical-external-cavity surface-emitting lasers: Finite-element analysis of a heatspreader approach. *Ieee Journal of Quantum Electronics*, 41(2):148–155, 2005.

[31] http://www.cohr.com/lasers.

[32] J. E. Hastie, J. M. Hopkins, S. Calvez, C. W. Jeon, D. Burns, R. Abram, E. Riis, A.I. Ferguson, and M. D. Dawson. 0.5-w single transverse-mode operation of an 850-nm diode-pumped surface-emitting semiconductor laser. *Ieee Photonics Technology Letters*, 15(7):894–896, 2003.

[33] M. Schmid, S. Benchabane, F. Torabi-Goudarzi, R. Abram, A. I. Ferguson, and E. Riis. Optical in-well pumping of a vertical-external-cavity surface-emitting laser. *Applied Physics Letters*, 84(24):4860–4862, 2004.

[34] M. I. Mller, C. Karnutsch, J. Luft, W. Schmid, K. Streubel, N. Linder, S.-S. Beyertt, U. Brauch, A. Giesen, and G. H. Dohler. Optically pumped vertical external cavity semiconductor thin-disk laser with cw operation at 660 nm. *Proc. Int. Symp. Compound Semiconductors*, 174:427–430, 2003.

[35] J. E. Hastie, S. Calvez, M. D. Dawson, T. Leinonen, A. Laakso, J. Lyytikainen, and M. Pessa. High power cw red vecsel with linearly polarized tem00 output beam. *Optics Express*, 13(1):77–81, 2005.

[36] J. E. Hastie, L. G. Morton, S. Calvez, M. D. Dawson, T. Leinonen, M. Pessa, G. Gibson, and M. J. Padgett. Red microchip vecsel array. *Optics Express*, 13(18):7209–7214, 2005.

[37] J. M. Hopkins, S. A. Smith, C. W. Jeon, H. D. Sun, D. Burns, S. Calvez, M. D. Dawson, T. Jouhti, and M. Pessa. 0.6 wcwgainnasvertical external-cavity surface emitting laser operating at 1.32 mu m. *Electronics Letters*, 40(1):30–31, 2004.

[38] C. Symonds, J. Dion, I. Sagnes, M. Dainese, M. Strassner, L. Leroy, and J. L. Oudar. High performance 1.55 mu m vertical external cavity surface emitting laser with broadband integrated dielectric-metal mirror. *Electronics Letters*, 40(12):734–735, 2004.

[39] H. Lindberg, A. Strassner, E. Gerster, and A. Larsson. 0.8w optically pumped vertical external cavity surface emitting laser operating cw at 1550 nm. *Electronics Letters*, 40(10):601–602, 2004.

[40] S. Hoogland, A. Garnache, I. Sagnes, B. Paldus, K. J. Weingarten, R. Grange, M. Haiml, R. Paschotta, U. Keller, and A. C. Tropper. Picosecond pulse generation with 1.5 mu m passively modelocked surface-emitting semiconductor laser. *Electronics Letters*, 39(11):846–847, 2003.

[41] R. Paschotta, R. Haring, A. Garnache, S. Hoogland, A. C. Tropper, and U. Keller. Soliton-like pulse-shaping mechanism in passively mode-locked surface-emitting semiconductor lasers. *Applied Physics B-Lasers and Optics*, 75(4-5):445–451, 2002.

[42] D. Lorenser, H. J. Unold, Djhc Maas, A. Aschwanden, R. Grange, R. Paschotta, D. Ebling, E. Gini, and U. Keller. Towards wafer-scale integration of high repetition rate passively mode-locked surface-emitting semiconductor lasers. *Applied Physics B-Lasers and Optics*, 79(8):927–932, 2004.

[43] S. Hoogland, A. Garnache, I. Sagnes, J. S. Roberts, and A. C. Tropper. 10-ghz train of sub-500-fs optical soliton-like pulses from a surface-emitting semiconductor laser. *Ieee Photonics Technology Letters*, 17(2):267–269, 2005.

[44] A. Aschwanden, D. Lorenser, H. J. Unold, R. Paschotta; E. Giniand, and U. Keller. 2.1-w picosecond passively mode-locked external-cavity semiconductor laser. *Optics Letters*, 30(3):272–274, 2005.

[45] http://people.deas.harvard.edu/jones/ap216/images/ bandgap_engineering/bandgap_engineering.html.

[46] http://www.css.sfu.ca/sites/csdl/research.html.

[47] M. Kneissl, D. W. Treat, M. Teepe, N. Miyashita, and N. M. Johnson. Continuous-wave operation of ultraviolet ingan/inalgan multiple-quantum-well laser diodes. *Applied Physics Letters*, 82(15):2386–2388, 2003.

[48] C. Lin, R. Yang, S. Murry, S. Pei, C. Yan, D. McDaniel, and M. Falcon. Room tempreature low-threshold type-ii quantum-well lasers at 4.5 μm. *IEEE Photonics Technology Letters*, 9:1573, 2005.

[49] K. K. Chow and S. W. Koch. Semiconductor-laser fundamentals - physics of gain materials. *Springer-Verlag Berlin*, 1999.

[50] http://www.mtmi.vu.lt/pfk/funkc_dariniai/ nanostructures/quant_structures.htm.

[51] L. A. Coldren and S. W. Corzine. Diode lasers and photonic integrated circuits. *John Wiley and Sons New York*, 1995.

[52] J. Geske, K. G. Gan, Y. L. Okuno, J. Piprek, and J. E. Bowers. Vertical-cavity surface-emitting laser active regions for enhanced performance with optical pumping. *Ieee Journal of Quantum Electronics*, 40(9):1155–1162, 2004.

[53] J. E. Hastie, C. W. Jeon, D. Burns, J. M. Hopkins, S. Calvez, R. Abram, and M. D. Dawson. A 0.5 w, 850 nm alxga1-xasvecsel with intra-cavity silicon carbide heatspreader. In *Advanced Lasers and Systems*, volume 5137 of *Proceedings of the Society of Photo-Optical Instrumentation Engineers (Spie)*, pages 201–206. SPIE-INT SOCIETY OPTICAL ENGINEERING, Bellingham, 2002.

[54] F. X. Kartner, J. Aus der Au, and U. Keller. Mode-locking with slow and fast saturable absorbers - what's the difference? *IEEE Journal of Selected Topics in Quantum Electronics*, 4:159–168, 1998.

[55] M. A. Holm, D. Burns, P. Cusumano, A. I. Ferguson, and M. D. Dawson. High-power diode-pumped algaas surface-emitting laser. *Applied Optics*, 38(27):5781–5784, 1999.

[56] H. A. Haus. Mode-locking of lasers. *IEEE Journal on Selected Topics in Quantum Electronics*, 6:1173–1185, 2000.

[57] O. Svelto. In *Principles of Lasers*. 1998.

[58] L. O'Faolain, M. B. Flynn, R. Wilson, and T. F. Krauss. A kerr mode-locked semiconductor laser: Design and theory. *Ieee Journal of Selected Topics in Quantum Electronics*, 10(5):1063–1069, 2004.

[59] K. Veskiusis. Phd thesis, univsersity of southampton. 2003.

[60] A. Garnache, S. Hoogland, A. C. Tropper, I. Sagnes, G. Saint-Girons, and J. S. Roberts. Sub-500-fs soliton-like pulse in a passively mode-locked broadband surface-emitting laser with 100 mw average power. *Applied Physics Letters*, 80(21):3892–3894, 2002.

[61] A. Mysyrowicz, D. Hulin, A. Antonetti, and A. Migus. Dressed excitons in a multiple-quantum-well structure - evidence for an optical stark-effect with femtosecond response-time. *Physical Review Letters*, 56(25):2748–2751, 1986.

[62] M. Haiml, R. Grange, and U. Keller. Optical characterization of semiconductor saturable absorbers. *Appl. Phys. B*, 79:331, 2004.

[63] V. M. Baev, T. Latz, and P. E. Toschek. Laser intracavity absorption spectroscopy. *Applied Physics B-Lasers and Optics*, 69(3):171–202, 1999.

[64] V. M. Baev, J. Eschner, E. Paeth, R. Schuler, and P. E. Toschek. Intracavity spectroscopy with diode-lasers. *Applied Physics B-Photophysics and Laser Chemistry*, 55(6):463–477, 1992.

[65] F. X. Kartner, L. R. Brovelli, D. Kopf, M. Kamp, I. Calasso, and U. Keller. Control of solid-state laser dynamics by semiconductor-devices. *Optical Engineering*, 34(7):2024–2036, 1995.

[66] A. Aschwandan. Phd thesis, eth zurich, 2003.

[67] M. J. Brennan, J. N. Milgram, P. Mascher, and H. K. Haugen. Wavelength tunable ultrashort pulse generation from a passively mode-locked asymmetric-quantum-well semiconductor laser. *Applied Physics Letters*, 81(14):2502–2504, 2002.

[68] C. F. Lin, Y. S. Su, and B. R. Wu. External-cavity semiconductor laser tunable from 1.3 to 1.54 mu m for optical communication. *Ieee Photonics Technology Letters*, 14(1):3–5, 2002.

[69] M. Endo and G. Ghosh. Timing jitter reduction of ultrashort tunable pulses using a mode-locked fiber laser in soliton regime. *Laser Physics*, 9(1):328–333, 1999.

[70] C. M.DePriest, T. Yilmaz, P. J. Delfyett, S. Etemad, A. Braun, and J. Abeles. Ultralow noise and supermode suppression in an actively mode-locked external-cavity semiconductor diode ring laser. *Optics Letters*, 27(9):719–721, 2002.

[71] R. Paschotta. Noise of mode-locked lasers (part ii): timing jitter and other fluctuations. *Applied Physics B-Lasers and Optics*, 79(2):163–173, 2004.

[72] R. Paschotta. Noise of mode-locked lasers (part i): numerical model. *Applied Physics B-Lasers and Optics*, 79(2):153–162, 2004.

[73] D. von der Linde. Characterization of the noise in continuously operating mode-locked lasers. *Appl Phys B*, 39:201–217, 1986.

[74] L-P. Chen, Y. Wang, and J-M. Liu. Spectral measurement of the noise in continuous-wave mode-locked laser pulses. *IEEE J Quant Elec*, 32:1817–1825, 1996.

[75] R. P. Scott, C. Langrock, and B. H. Kolner. High-dynamic-range laser amplitude and phase noise measurement techniques. *Ieee Journal of Selected Topics in Quantum Electronics*, 7(4):641–655, 2001.

[76] R. Paschotta, B. Rudin, A. Schlatter, G. J. Spuhler, L. Krainer, S. C. Zeller, N. Haverkamp, H. R. Telle, and U. Keller. Relative timing jitter measurements with an indirect phase comparison method. *Applied Physics B-Lasers and Optics*, 80(2):185–192, 2005.

[77] D. L. Woolard, E. R. Brown, M. Pepper, and M. Kemp. Terahertz frequency sensing and imaging: A time of reckoning future applications? *Proceedings of the Ieee*, 93(10):1722–1743, 2005.

[78] D.H. Auston, K.P. Cheung, and P.R. Smith. Picosecond photoconducting herzian dipoles. *Applied Physics Letters*, 45:284–286, 1984.

[79] http://www.tu-braunschweig.de/ihf/ag/terahertz.htm.

[80] http://www.sanken.osaka-u.ac.jp/ labs/bis/research/thz/thz.htm.

[81] http://www.iemn.univ-lille1.fr/sites_perso/ vignaud/english/source_thz.htm.

[82] R. Yano, H. Gotoh, Y. Hirayama, S. Miyashita, Y. Kadoya, and Y. Hattori. Terahertz wave detection performance of photoconductive antennas: Role of antenna structure and gate pulse intensity. *Journal of Applied Physics*, 97(10), 2005. Part 1.

[83] S. Kono, M. Tani, and K. Sakai. Generation and detection of broadband pulsed terahertz radiation. In *Terahertz Optoelectronics*, volume 97 of *Topics in Applied Physics*, pages 31–62. 2005.

[84] J. Sigmund, C. Sydlo, H. L. Hartnagel, N. Benker, H. Fuess, F. Rutz, T. Kleine-Ostmann, and M. Koch. Structure investigation of low-temperature-grown gaassb, a material for photoconductive terahertz antennas. *Applied Physics Letters*, 87:252103, 2005.

[85] R. Mendis, C. Sydlo, J. Sigmund, M. Feiginov, P. Meissner, and H. L. Hartnagel. Tunable cw-thz system with a log-periodic photoconductive emitter. *SOLID-STATE ELECTRONICS*, 48(10-11):2041–2045, 2004.

[86] P. Knobloch, C. Schildknecht, T. Kleine-Ostmann, M. Koch, S. Hoffmann, M. Hofmann, E. Rehberg, M. Sperling, K. Donhuijsen, G. Hein, and K. Pierz. Medical thz

imaging: an investigation of histo-pathological samples. *Physics in medicine and Biology*, 47:3875–3884, 2002.